

**MECHANISMS AND APPLICATIONS OF PHOTOINDUCED
PROCESSES IN FLUORESCENT PROTEINS**

A Thesis
Presented to
The Academic Faculty

by

Russell Vegh

In Partial Fulfillment
of the Requirements for the Degree
Doctor of Philosophy in the
School of Chemistry and Biochemistry

Georgia Institute of Technology
December 2012

**MECHANISMS AND APPLICATIONS OF PHOTOINDUCED
PROCESSES IN FLUORESCENT PROTEINS**

Approved by:

Dr. Laren M. Tolbert, Advisor
School of Chemistry and Biochemistry
Georgia Institute of Technology

Dr. Andreas S. Bommarius
School of Chemical and Biomolecular
Engineering
Georgia Institute of Technology

Dr. Wendy L. Kelly
School of Chemistry and Biochemistry
Georgia Institute of Technology

Dr. Christine K. Payne
School of Chemistry and Biochemistry
Georgia Institute of Technology

Dr. Raquel L. Lieberman
School of Chemistry and Biochemistry
Georgia Institute of Technology

Date Approved: December 2012

**MECHANISMS AND APPLICATIONS OF PHOTOINDUCED
PROCESSES IN FLUORESCENT PROTEINS**

Approved by:

Dr. Laren M. Tolbert, Advisor
School of Chemistry and Biochemistry
Georgia Institute of Technology

Dr. Andreas S. Bommarius
School of Chemical and Biomolecular
Engineering
Georgia Institute of Technology

Dr. Wendy L. Kelly
School of Chemistry and Biochemistry
Georgia Institute of Technology

Dr. Christine K. Payne
School of Chemistry and Biochemistry
Georgia Institute of Technology

Dr. Raquel L. Lieberman
School of Chemistry and Biochemistry
Georgia Institute of Technology

Date Approved: December 2012

ACKNOWLEDGEMENTS

I would first like to thank my advisors Drs. Laren Tolbert and Andreas Bommarius for the many opportunities they have set in front of me. I am very grateful for their years of continued support, encouragement, and funding throughout my graduate studies. They have always permitted me to pursue my own ideas and interests allowing me to become an independent scientist in the process.

My graduate studies would have also not been possible without the guidance and support of my good friend, mentor, and colleague Dr. Kyril Solntsev. He has been critically involved working closely with me throughout my time at Georgia Tech and has helped to provide unique and exciting experiences such as traveling abroad. Without his expertise, hard work, encouragement, and constant guidance I would not have become the mature and skilled scientist I am today.

I would also like to thank the members of my committee, Drs. Wendy Kelly, Christine Payne, and Raquel Lieberman, for their thoughtful comments and insights regarding this endeavor. Without their guidance, this work would not be the necessary contribution to the literature that it is today.

An important part of my graduate education was achieved through collaborations with both local and foreign scientists. I would like to thank my local collaborator Dr. Rob Dickson and his student Amy Jablonski for their dedication to this project. It should be noted that all of the fluorescence modulation experiments were performed by her, as well as the data analysis with the aid of Prof. Dickson. These are acknowledged in the text, but also here. Thank you also to Dr. Malcolm Forbes who hosted me at his house while I

conducted research in his laboratory in Chapel Hill, NC. The work I conducted there would not have been possible without the expertise of his post-doctoral researcher Robert Schmidt and graduate student Lauren Jarocho. I would also like to thank our collaborators in Helsinki, Finland, where the transient absorption spectroscopy measurements were performed with the use of their state-of-the-art transient spectroscopy system. Dr. Dima Bloch went above and beyond to help me obtain publishable results while I was stationed there. I would also like to thank his collaborators, Misha Verkhovsky, Virve Rauhamaki, Marko Rintanen, and James Evans for all their help, lively discussion, and for making me feel at home while I was over 4800 miles away. Finally I want to remember and express my gratitude to Dr. Michael Verkhovsky who recently passed with cancer; I will always remember our spirited discussions and will undoubtedly carry his wisdom with me into my future career.

During my graduate career I was fortunate enough to mentor several undergraduate students. Working with them has allowed me to extend my project into areas that would have otherwise gone unexplored. Therefore I would like to thank Soohee Cho, Savini Santha, and Adrian Amador for their hard work and dedication to these projects.

Of course I cannot ignore the continued support and assistance of my lab members from both research groups. Michael Abrahamson has remained a good friend throughout the years. The time we spent at the gym, the lake, or just relaxing at home always helped to deflect some of our frustrations and stress associated with the countless hours spent in lab and for that I am endlessly grateful. E-A Gould, a longtime friend and fellow lab mate, has provided tremendous support throughout the last 5 years not only by

encouraging me as a researcher, but also for opening her home to me and providing me with a feeling of family in Atlanta. I must also express my thanks to other current and former members of both groups, including Jonathan Park, Janna Blum, Jonathan Rubin, Ryan Clairmont, Yuzhi Kang, Brett Fellows, Jing Chen, Mélanie Hall, Juan Vargas, Michael Rood, Nathan Jarnagin, Mike Salvitti, Yoon-Keun Chae, Robert Whetsell, and Anthony Baldrige.

TABLE OF CONTENTS

	Page
ACKNOWLEDGEMENTS	iii
LIST OF TABLES	viii
LIST OF FIGURES	x
LIST OF ABBREVIATIONS	xix
LIST OF SYMBOLS	xxii
SUMMARY	xxiii
<u>CHAPTER</u>	
1 INTRODUCTION AND OVERVIEW	1
2 PHOTOINDUCED PROCESSES IN RED FLUORESCENT PROTEINS	8
Introduction	8
Materials and Methods	11
Results	22
Discussion	71
Conclusions	76
3 HIDDEN PHOTOINDUCED PROTON TRANSFER IN THE BLUE FLUORESCENT PROTEIN MKALAMA1	78
Introduction	78
Materials and Methods	80
Results	82
Discussion	89
Conclusions	100
4 OPTICAL MODULATION OF FLUORESCENT PROTEINS	102

Introduction	102
Materials and Methods	105
Results	113
Discussion	123
Conclusions	126
5 CONCLUSIONS AND FUTURE WORK	127
APPENDIX A: DNA AND AMINO ACID SEQUENCES	132
APPENDIX B: ABSORPTION SPECTRA OF BLUE FLUORESCENT PROTEINS	137
REFERENCES	142

LIST OF TABLES

	Page
Table 2.1. Thermocycler parameters for the PCR reaction. After segment 1, the <i>Pfu</i> DNA polymerase was added.	13
Table 2.2. Fluorescence response of APF and HPF to various reactive oxygen species.	34
Table 4.1. Forward (F) and reverse (R) primers used to generate mutants of GFP-F99S/M153T/V163A/T203V/S205V.	107
Table 4.2. Forward (F) and reverse (R) primers used to generate mutants of GFP-F99S/M153T/V163A/T203V/S205V.	108
Table 4.3. Forward (F) and reverse (R) primers used to generate mutants of mKalamal.	108
Table 4.4. Forward (F) and reverse (R) primers used to generate mutants of Padron*.	109
Table 4.5. Forward (F) and reverse (R) primers used to generate mutants of Padron*.	110
Table 4.6. Forward (F) and reverse (R) primers used to generate mutants of Padron*.	111
Table 4.7. Photophysical parameters of T203V/S205V mutations for cw 405 nm excitation.*Low fluorescence enhancements make absolute frequencies hard to obtain, so these are not very reliable.	117
Table 4.8. Mutants of T203V/S205V with the corresponding fluorescence enhancement and characteristic frequency following co-excitation with 372 nm and 515 nm.	119
Table 4.9. Characteristic frequencies, as well as on and off times for Padron* and its mutants.	121
Table A.1. Amino acid sequences of KillerRed, mRFP, and DsRed each containing a polylinker and a 6xHN affinity tag. The 6xHN affinity tag and polylinker are underlined. The three residues which make up the chromophore are highlighted in red.	132
Table A.2. The DNA sequence of the KillerRed gene inserted between <i>Sa</i> I and <i>Not</i> I restriction sites in Pprotet.	133

Table A.3. Amino acid sequences containing polylinker and hexahistidine tag (underlined/bolded) for mKalama1 and GFP F99S/M153T/V163A/T203V/S205V. The three residues which make up the chromophore are highlighted in blue.	133
Table A.4. Amino acid sequences containing polylinker and hexahistidine tag (underlined/bolded) for EGFP and Padron*. The three residues which make up the chromophore are highlighted in green.	134
Table A.5. The DNA sequence of the mKalama1 Gene inserted between <i>XhoI</i> and <i>EcoRI</i> restriction sites in pBad-HisB.	134
Table A.6. The DNA sequence of the 203V/205V gene inserted between <i>BamHI</i> and <i>HindIII</i> restriction sites in PQE-30.	135
Table A.7. The DNA sequence of the Padron* gene inserted between <i>BamHI</i> and <i>HindIII</i> restriction sites in PQE-31.	136

LIST OF FIGURES

	Page
Figure 1.1. Representation of the 11 stranded β -barrel of GFP (PDB 1GFL) with the α -helix running through the center. Drawn using the PyMOL Molecular Graphics System, Version 1.2r3pre, Schrödinger, LLC.	2
Figure 1.2. Reaction scheme for GFP chromophore biogenesis redrawn from reference 7. The reaction scheme is cyclization, followed by dehydration and then oxidation, producing a stoichiometric amount of H_2O_2 .	2
Figure 1.3. Absorption (blue) and emission (green) spectrum of wtGFP. The A band belongs to the neutral chromophore while B band belongs to the anion.	3
Figure 1.4. Proposed decarboxylation mechanism of wtGFP redrawn from reference 16. The excited state chromophore accepts an electron from glutamate which then decarboxylates. After decarboxylation, the chromophore can then donate both an electron and a proton to quench the radical, leaving anionic chromophore.	4
Figure 2.1. Sequence alignment of KillerRed and DsRed. The amino acids are color coded. Red indicates small and hydrophobic (including tyrosine), blue is acidic, magenta is basic, and green is hydroxyl/sulfhydryl/amine/glycine. An * (asterisk) indicates positions which have a single, fully conserved residue. A : (colon) indicates conservation between groups of strongly similar properties. A . (period) indicates conservation between groups of weakly similar properties.	9
Figure 2.2. Photobleaching of KillerRed (left, isosbestic point at 488 nm), mRFP (middle), and DsRed (right) with 532 nm pulsed laser (340 mW/cm^2 , pulsed laser, 4 ns per pulse, 50-100 pulses per spectrum).	23
Figure 2.3. Time resolved traces at 1270 nm recorded for pure D_2O , KillerRed and standard photosensitizer $TPPS_4$ following 532 nm excitation. $A_{532 \text{ nm}} = 0.1$ for the dye solution and KillerRed.	24
Figure 2.4. Steady state luminescence spectra ($\lambda_{\text{ex}}=550 \text{ nm}$) of 1O_2 (from excitation of RoseBengal, black line), mRFP (blue line), and KillerRed (red line).	25
Figure 2.5. Phosphorescence decay of KillerRed at 1270 nm in 99% D_2O (black), 50% D_2O (red), and 100% H_2O (blue) following 532 nm excitation.	26
Figure 2.6. KillerRed phosphorescence signal at 1270 nm in PBS fit to a 3-exponential model.	26
Figure 2.7. The fluorescence of TEMPO-9-ac is initially quenched by the nitroxide moiety. Upon radical trapping, that fluorescence is restored ($\lambda_{\text{ex/em}} = 358/440 \text{ nm}$). Radical trapping can also be monitored by EPR spectroscopy.	28

- Figure 2.8. Absorption (left) and emission (right) spectra (λ_{ex} 358 nm) of KillerRed irradiated at various time intervals using Hanovia carousel photoreactor (see Materials and Methods). Samples were with (top) and without (bottom) radical fluorescence probe TEMPO-9-ac. 28
- Figure 2.9. Fluorescence spectra of TEMPO-9ac (20 μM) in PBS before (black line) and after (blue line) irradiation with Hanovia carousel photoreactor (see Materials and Methods). 29
- Figure 2.10. Fluorescence spectra ($\lambda_{\text{ex}}=358$ nm) of KillerRed and TEMPO-9ac irradiated with Hanovia carousel photoreactor (see Materials and Methods) at 1 hr intervals. Left graph –the sample bubbled with oxygen, right graph – the sample bubbled with nitrogen. 29
- Figure 2.11. Absorption spectra of KillerRed before and after 90 min of irradiation with Hanovia carousel photoreactor (see Materials and Methods). Samples were bubbled with either oxygen or nitrogen. 30
- Figure 2.12. Emission spectra ($\lambda_{\text{ex}}=565$ nm) of KillerRed before and after 90 min irradiation with Hanovia carousel photoreactor (see Materials and Methods). Samples were bubbled with either oxygen or nitrogen. 30
- Figure 2.13. Emission spectra ($\lambda_{\text{ex}}=358\text{nm}$) of DsRed (left) and KillerRed (right) in the presence TEMPO-9ac (20 μM) irradiated with a 532 nm laser (5 mW/cm^2). 31
- Figure 2.14. Absorption spectra of KillerRed and DsRed in the presence TEMPO-9ac irradiated with a 532 nm laser (5 mW/cm^2). 32
- Figure 2.15. mRFP (10 μM) and TEMPO-9ac (20 μM) irradiated using a Hanovia carousel photoreactor (see Materials and Methods). An increase in TEMPO-9-ac fluorescence indicates the production of radicals. 32
- Figure 2.16. β -Galactosidase alone or fused to either mRFP or KillerRed and irradiated using Hanovia carousel photoreactor (see Materials and Methods). 33
- Figure 2.17. Reaction of HPF or APF with various ROS produces the fluorescent compound fluorescein ($\lambda_{\text{ex/em}}=490/515$ nm). 34
- Figure 2.18. Emission spectra of KillerRed (13 μM) in the presence of HPF (left) and APF (right) irradiated with Hanovia carousel photoreactor (see Materials and Methods) at various times ($\lambda_{\text{ex}}=490$ nm). 35
- Figure 2.19. Fluorescence spectra ($\lambda_{\text{ex}}=490$ nm) of HPF (left) and APF (right) in PBS before (black) and after (blue) irradiation with Hanovia carousel photoreactor (see Materials and Methods). 35

- Figure 2.20. Emission spectra of KillerRed (13 μM) and APF (5 μM) in PBS before and after irradiation with Hanovia carousel photoreactor (see Materials and Methods). Samples were bubbled with oxygen or nitrogen ($\lambda_{\text{ex}}=490\text{ nm}$). 36
- Figure 2.21. EPR spectrum of KillerRed in PBS buffer after 40 min of irradiation with 560 nm (40 mW/cm^2) light using a Continuum Powerlite YAG laser pumping a Continuum OPO. 37
- Figure 2.22. From left to right: EPR spectra of mRFP, DsRed, and EGFP obtained after irradiation with 560 nm light (40 mW/cm^2) for RFPs and 480 nm (30 mW/cm^2) for EGFP. Samples were excited using a Continuum Powerlite YAG laser pumping a Continuum OPO. 38
- Figure 2.23. Fluorescence emission of KillerRed, Amplex[®] Red, and horseradish peroxidase after irradiation at different time intervals (solid lines). Dashed lines correspond to the resorufin fluorescence calculated as the difference between the normalized spectra at each time and $t = 0$. 39
- Figure 2.24. Calibration curve for the Amplex[®] Red assay. Serial dilutions of H_2O_2 were mixed with Amplex[®] red reagent and allowed to react for 30 min in the dark. This resulted in the formation of resorufin which was detected by its fluorescence at 585 nm. Detection limit: 0.1 μM H_2O_2 . 39
- Figure 2.25. Fluorescence spectra for Amplex[®] Red H_2O_2 Assay. As a control, H_2O_2 (1 mM, final concentration) was added to the Amplex[®] Red reagent and allowed to react for 30 min and then the fluorescence spectrum was measured (red line). For the sample, KillerRed (13 μM) was incubated with H_2O_2 for 24 hours and then mixed with the Amplex[®] Red reagent. It was allowed to react for 30 min and then the fluorescence spectrum was measured (black line). 41
- Figure 2.26. Fluorescence spectra for Amplex[®] Red H_2O_2 Assay. As a control, H_2O_2 (1 mM, final concentration) was added to the Amplex[®] Red reagent and allowed to react for 30 min and then the fluorescence spectrum was measured (red line). For the sample, mRFP (10 μM) was incubated with H_2O_2 for 24 hours and then mixed with the Amplex[®] Red reagent. It was allowed to react for 30 min and then the fluorescence spectrum was measured (black line). 42
- Figure 2.27. Fluorescence spectra for Amplex[®] Red H_2O_2 Assay. As a control, H_2O_2 (1 mM, final concentration) was added to the Amplex[®] Red reagent and allowed to react for 30 min and then the fluorescence spectrum was measured (red line). For the sample, EGFP (10 μM) was incubated with H_2O_2 for 24 hours and then mixed with the Amplex[®] Red reagent. It was allowed to react for 30 min and then the fluorescence spectrum was measured (black line). 43
- Figure 2.28. Absorption spectra of mRFP before and after addition of 800 μM H_2O_2 . 43
- Figure 2.29. Absorption spectra of EGFP before and after addition of 2 mM H_2O_2 . 44

- Figure 2.30. Absorption spectra of KillerRed before and after addition of 325 μM H_2O_2 . 44
- Figure 2.31. Fluorescence spectra of rosorufin formed by addition of Amplex® Red reagent to a solution of 5 μM H_2O_2 (black line) and to a solution containing 5 μM H_2O_2 and 10 μM BSA (red line). The solution containing 5 μM H_2O_2 and 10 μM BSA was incubated for 24 hours before addition of the Amplex® Red reagent. 45
- Figure 2.32. Ground state absorption spectra at pH 7.5 for mutants of KillerRed. N145T is shown in black and the double mutant N145T/A161C is shown in red. 46
- Figure 2.33. Ground state absorption spectra of N145T/A161C at pH 6.5 before (black) and after irradiation (red) with 407 nm light using the emission from a xenon arc lamp coupled to a monochromator (slit width of 2 nm). 47
- Figure 2.34. Chromophore pocket of KillerRed (PDB 3GB3) illustrating the important residues that favor the Z state. Drawn using the PyMOL Molecular Graphics System, Version 1.2r3pre, Schrödinger, LLC. 47
- Figure 2.35. Mass spectrum of unbleached DsRed in 10 mM ammonium acetate diluted 1:10 in a 50:50 water:acetonitrile mixture containing 0.1% formic acid. Calculated MW of DsRed is 28,319 Da which includes -24 Da for chromophore formation. 50
- Figure 2.36. Mass spectrum of partially bleached DsRed in 10 mM acetate diluted 1:10 in a 50:50 water:acetonitrile mixture containing 0.1% formic acid. 51
- Figure 2.37. Mass spectrum of native KillerRed in 10 mM acetate diluted 1:10 in a 50:50 water:acetonitrile mixture containing 1% formic acid. The calculated MW of KillerRed is 28,961 Da which includes -24 Da for cyclization-dehydration-oxidation. 52
- Figure 2.38. Mass spectrum of unbleached mRFP in 10 mM acetate diluted 1:10 in a 50:50 water:acetonitrile mixture containing 0.1% formic acid. The calculated MW of mRFP is 27,980 Da which includes -24 Da for cyclization-dehydration-oxidation. 53
- Figure 2.39. Mass spectrum of bleached mRFP in 10 mM acetate diluted 1:10 in water:acetonitrile:formic acid. The calculated MW of mRFP is 27,980 Da which includes -24 Da for cyclization-dehydration-oxidation. 54
- Figure 2.40. SDS PAGE (16%) of mRFP (lanes 1-2), protein ladder (lane 3), and KillerRed (lanes 4-5). Protein ladder contains 250, 150, 100, 75, 50, 37, 25, 20, 15, and 10 kD proteins (top to bottom). 55

Figure 2.41. SDS PAGE of protein ladder (lane 1), mRFP (10 μg , lane 2), induced cell lysate (lane 3), and non-induced cell lysate (lane 4). Protein ladder contains 119, 79, 46, 31, 24, and 19 kD proteins (top to bottom).	55
Figure 2.42. Native protein gel (16%) with 15 μg (lane 1) and 45 μg (lane 2) of purified KillerRed. The bottom band represents the monomer of KillerRed and the band above it is attributed to the dimer.	56
Figure 2.43. The protein sequence of KillerRed showing possible fragments after trypsinolysis.	57
Figure 2.44. Peptide mass fingerprint of native KillerRed following trypsin digest.	57
Figure 2.45. Peptide mass fingerprint of bleached KillerRed following trypsin digest. The protein was bleached 50% at 585 nm.	58
Figure 2.46. Peptide mass fingerprint of bleached KillerRed following trypsin digest. The protein was bleached 80% at 585 nm.	58
Figure 2.47. Sub-nanosecond TA spectra of KillerRed at pH 7.5 after excitation with 100 fs laser pulse (532 nm, 180 mW/cm ²).	59
Figure 2.48. Sub-nanosecond TA spectra of mRFP (left) and DsRed (right) at pH 7.5 after excitation with 100 fs laser pulse (532 nm, 180 mW/cm ²).	60
Figure 2.49. TA spectra of KillerRed following 532 nm excitation.	61
Figure 2.50. The result of the best multiexponential decay fit for the TA data of KillerRed.	61
Figure 2.51. Absorbance decays (dots) with kinetic fits (solid lines) for KillerRed at various wavelengths. Residuals displayed at bottom of graph with different vertical offsets. Time constants of the exponential decay components are shown at the top.	62
Figure 2.52. TA spectra of mRFP following 532 nm excitation.	63
Figure 2.53. The result of the best multiexponential decay for the TA data of mRFP.	63
Figure 2.54. Absorbance decays (dots) with kinetic fits (solid lines) for mRFP at various wavelengths. Residuals displayed at bottom of graph with different vertical offsets.	64
Figure 2.55. TA spectra of DsRed following 532 nm excitation. The sample was probed for 4 seconds.	65

- Figure 2.56. The result of the best multiexponential decay fit for the TA data of DsRed. The time point 4 sec is shown to demonstrate the production of decarboxylated photoproduct. 65
- Figure 2.57. Absorbance decays (dots) with kinetic fits (solid lines) for DsRed at various wavelengths. Residuals displayed at bottom of graph with different vertical offsets. Time constants of the exponential decay components are shown at the top. 66
- Figure 2.58. Decay of the transient signal at 731 nm for KillerRed for an oxygenated sample (top left, red line), a standard sample (top left, black line), an anaerobic sample (top left), and a sample in D₂O (top right). Decay of the transient signal at 722 nm for mRFP for an oxygenated sample (middle left, red line), a standard sample (middle left, black line), an anaerobic sample (middle left, blue line), and a sample in D₂O (middle right, blue line). Decay of the transient signal at 745 nm for DsRed for an oxygenated sample (bottom left, red line), a standard sample (bottom left, black line), an anaerobic sample (bottom left, blue line), and a sample in D₂O (bottom right, blue line). 67
- Figure 2.59. Kinetics of the TA signal at 731 nm for KillerRed (top), at 722 nm for mRFP (middle), and at 745 nm for DsRed in the absence and presence of H₂O₂. 69
- Figure 2.60. Ground state absorption spectra of KillerRed before and after addition of 34 μ M H₂O₂. 70
- Figure 2.61. Ground state absorption spectra of DsRed before and after addition of 34 μ M H₂O₂. 70
- Figure 2.62. Representation of the β -barrel of KillerRed (PDB 3GL3) with the long-filled water channel in red and residues 137-158 highlighted in orange. Drawn using the PyMOL Molecular Graphics System, Version 1.2r3pre, Schrödinger, LLC. 74
- Figure 2.63. Electron density map of photobleached KillerRed (PDB 3GL4, 2mF_o-DF_c contoured at 2 σ) showing residues 137-158 of monomer A (left) and monomer B (right). Drawn using the PyMOL Molecular Graphics System, Version 1.2r3pre, Schrödinger, LLC. 74

Figure 3.1. Optical properties of mKalama1. (a) Absorption and emission spectra of mKalama1 at various pH. Buffer: CCPBS (20 mM CAPS, 20 mM CABS, 20 mM KPi, 200 mM NaCl); pH adjusted with KOH. (b) TA spectra of mKalama1 at pH 7.5 after excitation with 100 fs 355 nm laser pulse (145 mw/cm²). (c) TA spectra of mKalama1 at pH 7.5 after excitation with 4 ns 355 nm laser pulse. The 600-750 nm part was magnified by the factor of 10 for better visualization. (d) Same as (c), but monitored in 1 ms - 1 min time window. (e) The results of the best multiexponential decay fit (Eq. 1) of the data from graph (c). The spectrum at $t = 0$ was calculated by the extrapolation of the fit. Buffer: PBS (pH 7.5). $\epsilon(\lambda)$: normalized to 1 mg/mL protein. 83

Figure 3.2. Fluorescence decay of mKalama1 at 460 nm excited with a 372 nm pulsed diode at pH 7.5 (upper panel) and multiexponential fit residuals (lower panel). 84

Figure 3.3. Fluorescence decay of mKalama1 at 510 nm excited with a 476 nm pulsed diode at pH 11.25 (upper panel) and multiexponential fit residuals (lower panel). 84

Figure 3.4. Absorption spectra of mKalama1(pH 7.5) irradiated for 0 hours (black), 1 hour (red), 2 hours (green), and 5 hours (blue) with 385±5 nm light (10 mW/cm²). Irradiation of mKalama1 was carried out using a Xenon lamp coupled to a monochromator. 85

Figure 3.5. Absorption spectra of mKalama1 before irradiation (red), after 4 hours irradiation at 385 nm (black, 10 mW/cm²), and then irradiated at 340 nm (2 mW/cm²) for 10 minutes (blue). Irradiation of mKalama1 was carried out using a Xenon lamp coupled to a monochromator. 86

Figure 3.6. Absorption spectra of mKalama1 at pH 7.5 (red), at pH 12.0 (blue), and then titrated from pH 12.0 to pH 7.5 (black). 87

Figure 3.7. Excitation spectra of mKalama1 at various pH ($\lambda_{em} = 555$ nm). 88

Figure 3.8. Absorbance decays (dots) with kinetic fits (solid lines) at various wavelengths. Residuals displayed at bottom of graph with different vertical offsets. Time constants of the exponential decay components are shown at the top. 89

Figure 3.9. TA kinetics at 505 nm for mKalama1 in H₂O (red) and for mKalama1 incubated in D₂O for 14 h (blue). Kinetics of H₂O was scaled to match intensity of that in D₂O. 91

Figure 3.10. Left column: TA of mKalama1 at various pH after excitation with a 355 nm laser pulse. Right column: TA decays at various pH. 91

Figure 3.11. Photocycle of mKalamal showing the characteristic decay times and the wavelengths of the detected intermediates.	93
Figure 3.12. Normalized absorption spectra of <i>p</i> -HBDI in methanol (solid black) and mKalamal (solid blue) with their respective radical cation transients (dotted lines).	93
Figure 3.13. TA spectra of Mkalama1 showing the weak bands from 525 nm to 725 nm (left) with the kinetic traces at selected wavelengths (right).	95
Figure 3.14. TA kinetics at 625 nm for anaerobic conditions (red) and fully aerobic conditions (black).	95
Figure 3.15. TA spectrum at 860 μ s for wtGFP (pH 7.5).	96
Figure 3.16. Results of the multi-exponential decay fit for mKalamal under aerobic conditions (left) and anaerobic conditions (right). Data was fit using 1 μ s-1.7 ms time frame.	97
Figure 3.17. TA spectra for wtGFP T203V/S205V after 355 nm excitation.	99
Figure 3.18. The chromophore of GFP T203V (PDB 2QLE) and nearby residues. Drawn using the PyMOL Molecular Graphics System, Version 1.2r3pre, Schrödinger, LLC.	99
Figure 3.19. The chromophore of GFP T203V (PDB 2QLE) is shown in a slightly twisted version (yellow) to illustrate H180 as possible proton acceptor. Drawn using the PyMOL Molecular Graphics System, Version 1.2r3pre, Schrödinger, LLC.	100
Figure 4.1. Spectral representation of strategy behind the research: a) excitation of Z^N ; b) excited state isomerization and relaxation of Z^{N*} ; c) acid-base equilibration; d) ground-state isomerization of E^A ; e) excitation and photoisomerization of E^A (modulation); f) relaxation and reprotonation of Z^A .	104
Figure 4.2. Chromophore of GFP T203V (PDB 2QLE) with key surrounding residues. Drawn using the PyMOL Molecular Graphics System, Version 1.2r3pre, Schrödinger, LLC.	114
Figure 4.3. Ground state absorption spectra of T203V/S205V before and after irradiation with 355 nm light.	115
Figure 4.4. A) Enhancement as a function of modulation frequency fit to phase-resolved lifetime equations. B) Characteristic frequencies are plotted as a function of 405 nm primary excitation for T203V/S205V and T203V/S205V/H148K. Linear fit was performed to obtain the natural k_{decay} of each protein.	117

Figure 4.5. Enhancement factor versus primary intensity of (A) 405 nm and (B) 372 nm excitation of T203V/S205V and T203V/S205V/H148K. Enhancement factor of 1.0 indicates no fluorescent increase over primary alone.	118
Figure 4.6. Ground state absorption spectrum of mKalama1 (red) and mKalama1 G149K (black).	120
Figure 4.7. TA spectra for T203V/S205V at 2, 10, 30, 50, 80, and 240 μ s after excitation with a 355 nm laser.	122
Figure 4.8. TA spectra for H148K at 4, 10, 30, 50, 80, and 400 μ s after excitation with a 355 nm laser.	122
Figure 4.9. TA spectra for mKalama1 G149K at 4, 7, 13, 32, and 1660 μ s after excitation with a 355 nm laser. The kinetics of the transitions are affected by the probe light.	123
Figure 4.10. The chromophore of GFP T203V (PDB 2QLE) modeled in the <i>E</i> configuration with key surrounding residues. Drawn using the PyMOL Molecular Graphics System, Version 1.2r3pre, Schrödinger, LLC.	124
Figure B.1. Absorption spectra of the H148Y mutant of T203V/S205V for native sample (black) and partially bleached sampled (red).	137
Figure B.2. Absorption spectra of the H148K mutant of T203V/S205V at various irradiation times. The neutral absorption decreased while the anionic absorption increased.	137
Figure B.3. Absorption spectra of the S147R mutant of T203V/S205V for native sample (black) and partially bleached sampled (red).	138
Figure B.4. Absorption spectrum of the S147K mutant of T203V/S205V.	138
Figure B.5. Absorption spectrum of the H148G mutant of T203V/S205V.	139
Figure B.6. Absorption spectrum of the H148D mutant of T203V/S205V.	139
Figure B.7. Absorption spectrum of the F165H mutant of T203V/S205V.	140
Figure B.8. Absorption spectrum of the H148R mutant of T203V/S205V.	140
Figure B.9. Absorption spectrum of the V150A mutant of T203V/S205V.	141
Figure B.10. Absorption spectrum of the F165L mutant of T203V/S205V.	141

LIST OF ABBREVIATIONS

APF	3'-(<i>p</i> -Aminophenyl) fluorescein
BFP	Blue fluorescent protein
BSA	Bovine serum albumin
CALI	Chromophore-assisted laser inactivation
CCD	Charge-coupled device
CFD	Constant fraction discriminator
CFP	Cyan fluorescent protein
CHCA	α -Cyano-4-hydroxycinnamic acid
Cro	Chromophore
CT	Charge transfer
cw	Continuous wave
Da	Daltons
ddH ₂ O	Double-distilled water
DEPMPO	5-(Diethoxyphosphoryl)-5-methyl-1-pyrroline- <i>N</i> -oxide
DMPO	5,5-Dimethyl-1-pyrroline- <i>N</i> -oxide
DMSO	Dimethyl sulfoxide
DNA	Deoxyribonucleic acid
dNTP	Deoxyribonucleotide triphosphates
EGFP	Enhanced green fluorescent protein
EPR	Electron paramagnetic resonance
ESI	Electrospray ionization
ESPT	Excited-state proton transfer

FCS	Fluorescence correlation spectroscopy
FP	Fluorescent protein
FRET	Fluorescence resonance energy transfer
GFP	Green fluorescent protein
HCl	Hydrochloride
HEPES	4-(2-Hydroxyethyl)-1-piperazineethanesulfonic acid
HPF	3'-(<i>p</i> -Hydroxyphenyl) fluorescein
HPLC	High performance liquid chromatograph
HRP	Horseradish peroxidase
IMAC	Immobilized metal affinity chromatography
IPTG	Isopropyl β -D-1-thiogalactopyranoside
IRF	Instrument response function
LB	Lysogeny broth
MALDI	Matrix-assisted laser desorption/ionization
mRFP	Monomeric red fluorescent protein
MS	Mass spectrometry
MW	Molecular weight
NA	Numerical aperture
NTA	Nitrilotriacetic acid
OD	Optical density
ONPG	<i>ortho</i> -Nitrophenyl- β -galactoside
PAFP	Photoactivatable fluorescent proteins
PAGE	Polyacrylamide gel electrophoresis
PBS	Phosphate buffer saline
PCR	Polymerase chain reaction

PDA	Photodiode array
PFP	Photoswitchable fluorescent proteins
<i>p</i> -HBDI	<i>p</i> -Hydroxybenzylideneimidazolone
pK_a	Ground-state acidity constant
RFP	Red fluorescent protein
ROS	Reactive oxygen species
RPM	Rotations per minute
SDS	Sodium dodecyl sulfate
SOD	Superoxide dismutase
TA	Transient absorption
TCPK	Tosyl phenylalanyl chloromethyl ketone
TCSPC	Time correlated single photon counting
TEMED	Tetramethylethylenediamine
TEMPO-9-ac	4-((9-Acridinecarbonyl)amino)-2,2,6,6-tetramethylpiperidin-1-oxyl
TPPS ₄	<i>meso</i> -Tetra(4-sulfonatophenyl)porphine
trans-MVP	<i>trans</i> -1-(Methoxyvinyl)pyrene
wt	Wild-type
YFP	Yellow fluorescent protein

LIST OF SYMBOLS

ω	Angular frequency
τ	Lifetime
λ	Wavelength
λ_{em}	Wavelength of excitation
λ_{ex}	Wavelength of emission
ϕ	Quantum yield
μ	Micro
ν_{mod}	Modulation frequency
T_m	Melting temperature
T_1	Triplet state

SUMMARY

In the current work, the photophysics and photochemistry of the phototoxic red fluorescent protein (RFP) KillerRed was investigated. KillerRed's phototoxicity makes it useful for studying oxidative stress on cell physiology and for cell killing in photodynamic therapy. Spectroscopic probes were used to show that the phototoxicity of KillerRed stems primarily from a type I photosensitization mechanism producing radicals. The production of radicals was supported by electron paramagnetic resonance (EPR) studies, where a long-lived radical was observed in KillerRed and two other RFPs (mRFP and DsRed) following excitation. Transient absorption spectroscopy, various other spectroscopic techniques, and the published crystal structure of KillerRed indicate that the long-filled water channel is likely responsible for the increased phototoxicity of KillerRed.

In the blue fluorescent protein (BFP) mKalama1, some of the same techniques were applied to understand the photophysics and photochemistry on the timescale ranging from femtoseconds to seconds. Transient absorption spectroscopy and previously published results demonstrate that two-photon excitation of mKalama1 likely results in the formation of a radical cation and solvated electrons. This may explain the blinking behavior which has been observed on the single molecule level for many fluorescent proteins, the identity of which has remained elusive. It was also shown that the chromophore, while neutral in the ground state, does not exhibit excited-state proton transfer (ESPT) during its nanosecond excited-state lifetime; however, the chromophore undergoes a deprotonation in the ground state after electronic relaxation. This work plays

a key role in our understanding of fluorescent proteins and will help pave the way to developing new ones.

The research on the BFPs was extended to improve them for cellular imaging. This was accomplished by identification of dark states in the BFPs which are longer in wavelength than the collected fluorescence. Using dual lasers, it was shown that these dark states could be optically depleted, thereby increasing the overall fluorescence without enhancing the background fluorescence. Rational site-directed mutagenesis was carried out on the BFPs and the mutants were screened for fluorescence enhancement. These proteins were then analyzed using transient absorption spectroscopy to elucidate the identity of the dark state(s) used for fluorescence enhancement.

CHAPTER 1

INTRODUCTION AND OVERVIEW

The green fluorescent protein (GFP) was first described in 1955.¹ It was later isolated from the jellyfish *Aequorea* and identified as a protein in 1961.² In the jellyfish, the GFP emits light through a bioluminescent reaction. This reaction is mediated through the photoprotein aequorin, which is a complex of coelenterazine, oxygen, and apophotoprotein.³ Calcium binding in aequorin results in an intermolecular reaction, in which coelenterazine is oxidized to singlet-excited coelenteramide.³ The complex of coelenteramide and apoprotein is called the blue fluorescent protein which emits blue light (469 nm) upon relaxation to the ground state. This blue light is then transferred to the GFP via fluorescence resonance energy transfer (FRET) giving rise to emission at 508 nm.^{2,4}

The crystal structure of GFP, first solved in 1996^{5,6} (PDB 1EMA and 1GFL), contains an 11-stranded β -barrel with an α -helix running through the center (Figure 1.1). Central to the α -helix is the chromophore *p*-hydroxybenzylideneimidazolinone (*p*-HBDI) which is formed by an autocatalytic, posttranslational cyclization of the three residues S65, Y66, and G67, only requiring molecular oxygen (Figure 1.2). The reaction pathway for chromophore formation is cyclization-dehydration-oxidation with an equivalent amount of H₂O₂ formed in the process.^{7,8} The residue R96 plays a catalytic role in the biosynthesis of the chromophore by increasing the nucleophilicity of G67 in the cyclization reaction.^{9,10} The β -barrel, also known as the β -can, gives the chromophore its

structural rigidity owing to its fluorescent properties. Indeed, the free chromophores as well as the denatured protein are virtually non-fluorescent at room temperature.¹¹

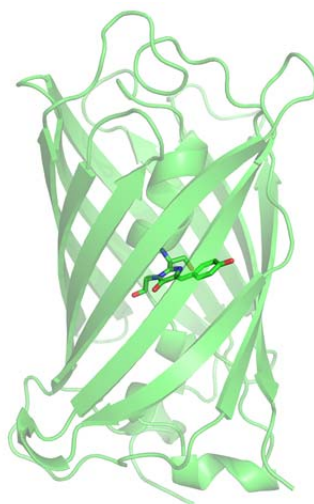


Figure 1.1. Representation of the 11 stranded β -barrel of GFP (PDB 1GFL) with the α -helix running through the center. Drawn using the PyMOL Molecular Graphics System, Version 1.2r3pre, Schrödinger, LLC.

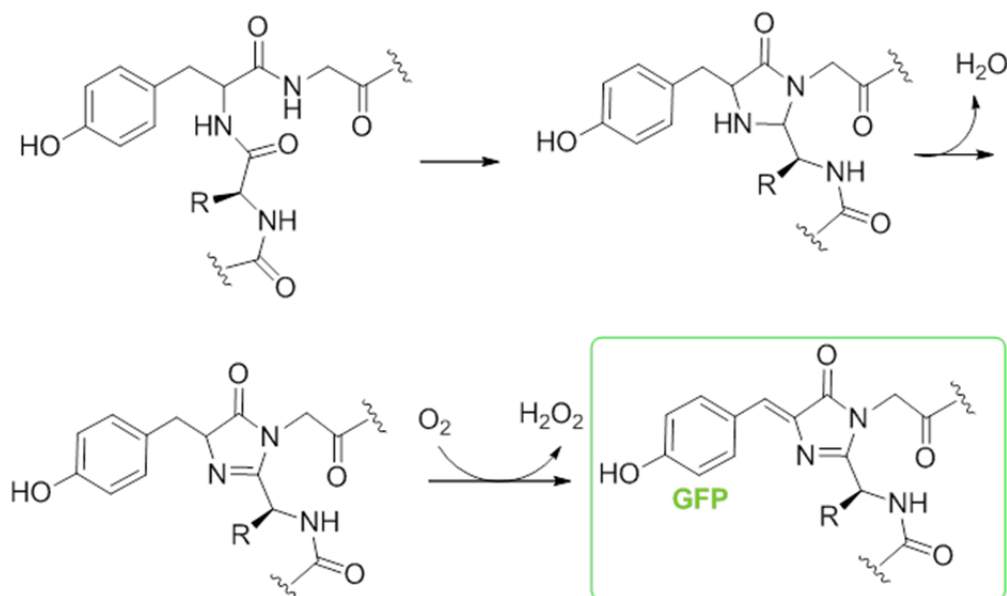


Figure 1.2. Reaction scheme for GFP chromophore biogenesis redrawn from reference 7. The reaction scheme is cyclization, followed by dehydration and then oxidation, producing a stoichiometric amount of H₂O₂.

The absorption spectrum of wild-type green fluorescent protein (wtGFP) has two main absorption peaks with maxima at 398 nm (band A) and 478 nm (band B) corresponding to the chromophore and its conjugate base, respectively (Figure 1.3).¹² Excitation of band A simultaneously yields weak 460 nm and strong 508 nm emission. The strong fluorescence at 508 nm occurs through an excited-state proton transfer (ESPT) mechanism, where the chromophore becomes deprotonated at the Y66 phenol group in the excited state resulting in a ~100 nm emission shift.¹²

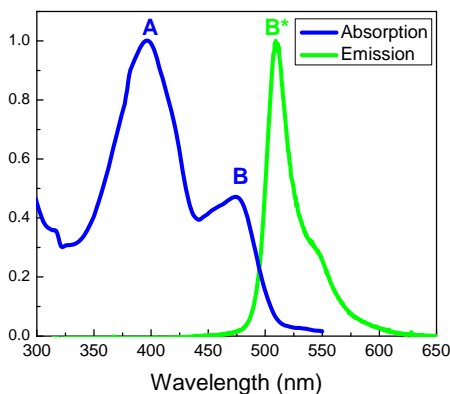


Figure 1.3. Absorption (blue) and emission (green) spectrum of wtGFP. The A band belongs to the neutral chromophore while B band belongs to the anion.

Illumination of wtGFP results in a decrease in the main absorption peak with concomitant increase and red shift of the anionic peak. This photobleaching occurs through decarboxylation of E222 via a Kolbe-type mechanism (Figure 1.4) in wtGFP and other fluorescent proteins.¹³⁻¹⁶ However, it has also been proposed that bleaching can occur by $^1\text{O}_2$ production¹⁷ as it is known that some fluorescent proteins (FPs) can produce

reactive oxygen species (ROS) upon illumination.¹⁷⁻²³ Although the phototoxicity is considered a negative trait for cellular imaging, it has been explored for chromophore-assisted laser inactivation (CALI),^{22,24} for photodynamic studies,²⁵ for studying oxidative stress on various cellular components,²⁶ and for massive light-induced damage of genomic DNA.^{27,28}

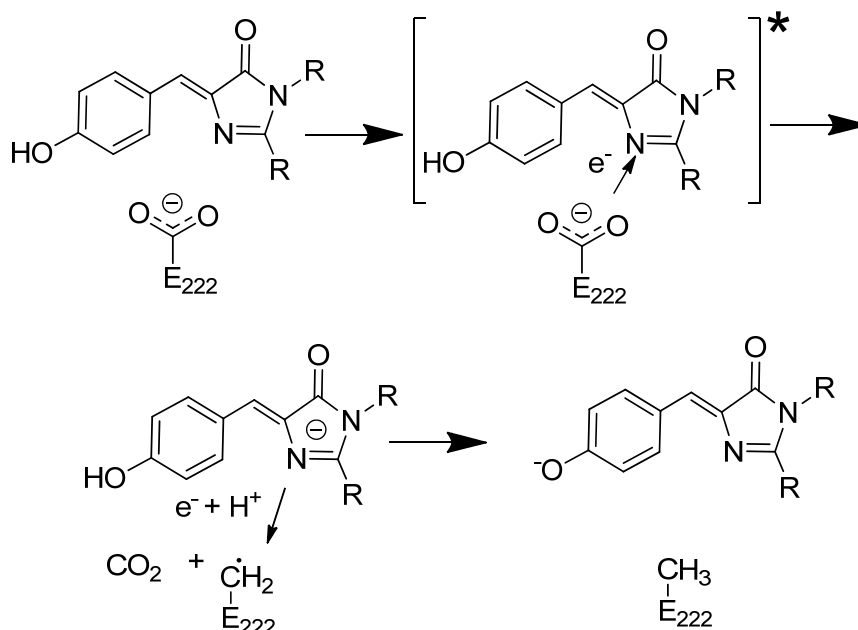


Figure 1.4. Proposed decarboxylation mechanism of wtGFP redrawn from reference 16. The excited state chromophore accepts an electron from glutamate which then decarboxylates. After decarboxylation, the chromophore can then donate both an electron and a proton to quench the radical, leaving anionic chromophore.

Surprisingly, G67 is the only residue of the tripeptide essential for chromophore formation in fluorescent proteins.¹⁸ The tyrosine moiety can be mutated to any aromatic residue to yield FPs of different colors. For example, mutation of the central tyrosine to histidine or tryptophan yields the blue (BFP) and cyan (CFP) fluorescent proteins respectively.⁸ The central chromophore has also been mutated to phenylalanine²⁹ as well

as unnatural amino acids^{30,31} to yield fluorescent proteins with a variety photophysical and photochemical properties.

Residues surrounding the chromophore also have a large effect on the photophysical and photochemical properties of FPs. For instance, the mutation T203Y leads to pi-pi stacking with the chromophore, giving the longer emitting yellow fluorescent protein (YFP).³² The proton wire can be blocked with the mutations T203V and S205V, thereby inhibiting excited state proton transfer yielding a BFP.^{33,34} The chromophore of red fluorescent proteins (RFPs) are anionic and undergo an additional oxidation step extending the conjugation of the chromophore and the emission wavelength.³⁵ The discovery of new FPs together with engineered variants of GFP and similar chromoproteins have allowed for coverage of the entire visible spectrum, most notably through the development of the “mFruits”TM by Roger Tsien.^{36,37} The unique properties of fluorescent proteins have been exploited for development of pH,³⁸ metal,^{39,40} and hydrogen peroxide sensors,⁴¹ as well as for inactivation of selected proteins,^{22,42} and cell killing in photodynamic therapy.²⁵

The expression of GFP in a nematode⁴³ boosted its potential for *in vivo* applications in live cell imaging. Imaging of FPs spurred a revolution that has increased our knowledge of biological processes. However, a common problem in imaging is the spatial resolution which is defined by the diffraction limit. The diffraction limit is the minimal distance at which two objects can be discerned. This limit was first recognized by Ernst Abbe⁴⁴ at the end of the 18th century and is governed by Equation 1.1:

$$d = \frac{\lambda}{2NA} \quad (\text{Eq. 1.1})$$

Where d is the diffraction limit, λ is the wavelength of light, and NA is the numerical aperture. With modern optics this limits the resolution to about a third of the wavelength or 200 nm. However, a new era of fluorescent proteins emerged with the discovery of photoactivatable fluorescent proteins (PAFPs).⁴⁵ These proteins are grouped into three different categories: i) those that can irreversibly switch from a dark-to-bright fluorescent state, ii) those that can irreversibly photoconvert from one fluorescent color to another,⁴⁵ or iii) those that can reversibly switch from one state to another.^{33,46-49} In the case of the reversible photoswitchable fluorescent proteins (PFP), their switching behavior is due to a *Z-E (cis-trans)* isomerization of the chromophore.^{50,51} The other groups of PAFP are activated through a variety of other mechanisms.⁵² These proteins, along with new imaging techniques, have helped to break the diffraction limit and obtain resolutions better than 100 nm.^{45,53,54}

While GFP was discovered more than 50 years ago, it was not until the 1990s that GFP was employed as an *in vivo* fluorescent marker.⁴³ The development of a variety of FPs together with their unique photophysical and photochemical properties has allowed us to better understand the complex processes in individual cells as well as whole organisms. Without these remarkable tools, much would remain unknown in these complex biological systems. Due to their complex nature and overwhelming variety, however, there is still much that can be improved upon and that still remains unknown about the dynamics in FPs.

Until recently, the use of FPs has largely been in static applications, i.e., imaging. That is, even though the cellular processes which are imaged by FPs are dynamic, the FPs are acting merely as reporters. There is a growing interest in FPs which are themselves

photochemically active, either by initiating chemical processes or by undergoing photoprocesses which change their response. This thesis addresses examples of each.

Chapter 2 discusses the photochemistry and photoprocesses of the phototoxic fluorescent protein KillerRed. This fluorescent protein exhibits phototoxicity upon excitation with green light generating reactive oxygen species (ROS).²⁰⁻²² KillerRed's phototoxicity is far greater than most other fluorescent proteins²² making it useful for photodynamic therapy,²⁵ for chromophore-assisted laser inactivation (CALI),²² for studying oxidative stress on various cellular components,²⁶ and for massive light-induced damage of genomic DNA.^{27,28} The ROS produced by KillerRed and the mechanistic details behind the phototoxicity are the subject of discussion.

Chapters 3 and 4 discuss the photoprocesses in fluorescent proteins and how these time dependent processes can be manipulated to facilitate their use in cellular imaging. By mutating various residues around the active chromophore, one can alter the dynamics of these time dependent processes allowing for better use in cellular imaging. How these specific mutations affect the chemistry of these proteins is discussed.

CHAPTER 2

PHOTOINDUCED PROCESSES IN RED FLUORESCENT PROTEINS

Introduction

RFPs are anionic and are formed by an additional oxidation step during chromophore maturation, resulting in extended conjugation and a longer emission wavelength.³⁵ The development of RFPs has allowed for better tissue penetration depth⁵⁵ and separation from cellular autofluorescence.⁵⁶ DsRed, a tetrameric RFP originally cloned from *Discoma* coral and mutated to improve its fluorescent properties, was the first of its kind.⁵⁷ The crystal structure⁵⁸ and the mechanism of bleaching¹⁴ show that photobleaching is a result of the decarboxylation of E215 (E222 in wtGFP). Due to its tetrameric nature, DsRed was mutated to yield a monomeric red fluorescent protein (mRFP) which has a ~25 nm red shift compared to DsRed.⁵⁶ Then, in 2006, the fluorescent protein KillerRed, a dimeric RFP derived by mutation of the chromoprotein anm2CP, was found to exert phototoxicity upon irradiation with light of 540-580 nm due to the formation of ROS.²⁰⁻²² The sequence alignment of KillerRed and DsRed, obtained using ClustalW,⁵⁹ gives a 26% amino acid identity (Figure 2.1). Despite having the same chromophore (QYG) as KillerRed, DsRed does not show any evidence of phototoxicity.²²

of the chromophore to the outside environment. This channel has been considered the escape route for the ROS and, thus, is likely responsible for the enhanced ROS generation and transport.^{64,65} Although solvent access to the chromophore is not a unique property of KillerRed, the accessibility occurs close to the methylene bridge and imidazolinone moiety, presumably the most reactive groups of the chromophore in the excited state.^{65,66} Compared to other fluorescent proteins, KillerRed exhibits the largest cavity so far.⁶⁵ Using molecular dynamic simulations, the diffusion pathways for molecular (O_2) and singlet oxygen (1O_2) in KillerRed were investigated.⁶⁷ The authors estimated that the exit time for O_2 out of the channel is $\sim 2-11$ ps while 1O_2 was proposed to react with the local environment before having a chance to escape.⁶⁷ It is hypothesized this water-filled channel is closed by residues Y74 and H80 which can transiently open upon rearrangements of the two residues.⁶⁷ The diffusion of O_2 throughout the channel does not significantly disrupt the network of water molecules and is thought to provide the structural plasticity needed for long-range diffusion.⁶⁷

Although the phototoxicity of KillerRed is unambiguously related to ROS production,^{21,22,26,64,65} the distribution of the latter and the mechanism of their formation is still a matter of debate. ROS generation by photosensitizers can occur by either a type I or type II photosensitization mechanism. Superoxide (O_2^-) and other radical species are generated by a type I mechanism by electron transfer to/from the substrate, or hydrogen transfer from the substrate in the excited triplet state (T_1) of the sensitizer. The most common electron acceptor is molecular oxygen, $O_2(X^3\Sigma_g^-)$, forming O_2^- , which can react with its surroundings to produce other reactive oxygenated products. Type II

photosensitization produces singlet oxygen $O_2(a^1\Delta_g) = {}^1O_2$ by direct energy transfer from T_1 state of the photosensitizer to $O_2(X^3\Sigma_g^-)$.⁶⁸

Only a few contradicting reports from the discoverers of KillerRed exist,^{21,64,69} suggesting different (type I, type II, or both) photosensitization mechanisms. While formation of both O_2^- and 1O_2 using fluorescent molecular probes has been reported,²¹ more recent reports demonstrate that an antibody-KillerRed chemical conjugate kills cancer cells in H_2O more efficiently than in D_2O .⁶⁴ The authors consider this as indirect proof that the role of 1O_2 in the KillerRed phototoxicity is negligible, since the lifetime of 1O_2 is longer in D_2O ⁷⁰ and, therefore, should enhance cytotoxicity. In all cases, the phototoxic action of KillerRed is accompanied by bleaching.^{21,22,64,69}

To employ KillerRed as a possible therapeutic agent and to elucidate the mechanisms of bleaching and phototoxicity, it is important to determine the ROS distribution. Herein, the photophysical and photochemical properties of the three RFPs-- KillerRed, DsRed, and mRFP--are studied. The origin of the phototoxicity is investigated using a number of direct and indirect methods. Transient absorption (TA) spectroscopy is used to identify dark states in these RFPs, and the results reinforce the implications of the protein structure on the phototoxicity.

Materials and Methods

Protein expression and purification

The gene encoding DsRed was amplified from DsRed2-1 plasmid (BD Biosciences Clontech, Palo Alto, CA) and cloned into pProTet (Clontech) between *SalI* and *NotI* restrictions sites and contained an N-terminal 6xHN affinity tag. The genes encoding KillerRed and mRFP (Genbank accession numbers AAY40168.1 and AAM54544,

respectively) were cloned into pProTet between the *SalI* and *NotI* restriction sites and contain an N-terminal 6xHN affinity tag. For protein expression, the plasmids were transformed into *E. coli* DH5- α -pro. A 5 mL culture was inoculated into 1 L of Lysogeny Broth (LB, pH 7) containing 35 $\mu\text{g/mL}$ of chloramphenicol, grown to an OD600 of 0.4 at 37 °C (2-3 h), and then induced with anhydrotetracycline (1 mg/mL). The temperature was reduced to 32 °C for expression. The proteins were overexpressed to 20% of cell protein and purified the protein via Ni^{2+} -nitrilotriacetic acid (NTA)-immobilized metal affinity chromatography (IMAC). All measurements were performed in phosphate buffer saline (PBS, 50 mM phosphate, 250 mM NaCl, pH 7.5), unless otherwise stated.

Anhydrotetracycline

Anhydrotetracycline was made by dissolving 250 mg/L of tetracycline in water, the pH adjusted to 3, and the sample autoclaved for 45 min at 121 °C.

Site-directed mutagenesis

Mutagenesis of the KillerRed gene was performed using the rapid-polymerase chain reaction (PCR) site-directed mutagenesis method.⁷¹ The PCR reaction mixture contained the following:

25 μL of 2X Failsafe™ PCR buffer J (Epicentre®, Madison, WI)

20 μL of ddH₂O (autoclaved)

1.5 μL of 10 μM Forward primer

1.5 μL of 10 μM Reverse primer

1 μL of Methylated template DNA (50 ng)

1 μL of *Pfu* DNA Polymerase (Added after segment 1, Table 2.1)

The reaction was carried out in a thermocycler with the parameters in Table 2.1.

Table 2.1. Thermocycler parameters for the PCR reaction. After segment 1, the *Pfu* DNA polymerase was added.

Segment	Cycles	Temperature	Time
1	1	98 °C	5 minutes
2	17	98 °C	30 seconds
		52 °C	1 minute
		72 °C	10 minutes

The Failsafe™ PCR buffer contains a buffered salt solution with all 4 dNTPs, MgCl₂, and Failsafe™ PCR enhancer (with betaine). Forward and reverse oligonucleotide primers were purchased from Eurofins MWG Operon (Huntsville, Alabama). All primers ended in either a G or C and contained a minimum of 15 bp on either side of the mutation site. The size of the flanking regions on either side of the mutation site was modified so that the melting temperatures (T_m) of both sides were somewhere between 50-60 °C and within 1 °C of each other. After running the PCR, 1 µL of *DpnI* was added to the reaction mixture and incubated at 37 °C overnight. The sample was then heated to 80 °C for 20 minutes to deactivate the *DpnI*. Transformation of the DNA was carried out by adding 2 µL of the reaction mixture to 100 µL of XL1-Blue competent cells. The cells were heated to 42 °C for 1 minute to increase the cell permeability. Then, 400 µL of LB was added and the sample was incubated in a thermomixer at 37 °C for 1 hour with shaking at 700 RPM. The sample was then plated on agar plates containing LB and chloramphenicol. Colonies were picked, grown overnight, and the DNA was extracted and purified using the QIAprep Spin Miniprep kit (Qiagen, USA). The purified DNA was sent to Eurofins MWG Operon (Huntsville, Alabama) where sequencing analysis confirmed the amplified product. For unsuccessful reactions, the annealing temperature (52°C, Table 2) was varied until the mutant was obtained.

Trypsinolysis of KillerRed and HPLC purification of peptides

KillerRed (80 µg) was denatured in 200 µL of 6 M urea for 10 min at 95 °C. It was then cooled to 30 °C and 800 µL of digest buffer (50 mM HEPES, 300 mM NaCl, and 20 mM CaCl₂, pH 8.0) containing trypsin (40 µg, tosyl phenylalanyl chloromethyl ketone (TCPK) treated trypsin from bovine pancreas, Sigma Aldrich) was added. The sample was incubated for 8 h at 30 °C and then dithiothreitol was added to a final concentration of 10 mM. The peptides were then separated by reverse-phase high performance liquid chromatography (HPLC). Tryptic peptides were separated by reverse-phase HPLC on a Shimadzu Prominence HPLC system (Columbia, MD) using a water/acetonitrile gradient containing 0.05% trifluoroacetic acid. The HPLC system was equipped with a Shimadzu-LC-20AT pump, Beckman Coulter Ultrasphere ODS C18 reverse phase column (5 µm, 4.6 mm x 25 mm), and SPD-M20A prominence photodiode array (PDA) detector. Peptide elution was monitored by absorbance at both 280 and 380 nm. Collected fractions were lyophilized immediately and then subjected to matrix-assisted laser desorption/ionization mass spectrometry (MALDI-MS). For mass spectral fingerprinting, the samples were lyophilized after digestion and then subjected to MALDI-MS.

MALDI-MS of KillerRed

The collected fractions containing peptides were dissolved in a small amount of ddH₂O and purified using Zip Tip® Pipette tips (EMD Millipore). The peptides were eluted from the Zip Tip® with 50:50 water:acetonitrile (containing 0.1% formic acid). A second elution was carried out with a 50:50 water:methanol (containing 0.1% formic acid). The MALDI-MS were acquired on a 4700 Proteomics Analyzer (Applied Biosystems). The

measurements were done in reflector mode using α -cyano-4-hydroxycinnamic acid (CHCA) as the matrix. The spectra were the sum of ~1500 laser shots.

Protein gel electrophoresis

Resolving gel (16%) was prepared by mixing 3.4 mL of ddH₂O, 2.5 mL of resolving buffer (1.5 M Tris HCl, pH 6.8), 100 μ L of disodium dodecyl sulfate (SDS; 10%, w/v), 4 mL of Bis-Acrylamide (40%), 50 μ L of ammonium persulfate (10%, w/v), and 10 μ L of tetramethylethylenediamine (TEMED). The solution was poured between the casting plates leaving ~3.5 cm to the top. Immediately after pouring the gel, 2 mL of ddH₂O was added on top of the gel to avoid air exposure. The gel was left to polymerize for 10-15 min. The layer of water was removed after polymerization. Stacking gel (4%) was prepared by mixing 6.4 mL of ddH₂O, 2.5 mL of stacking gel buffer (0.5M Tris HCl, pH 6.8), 100 μ L of SDS (10%, w/v), 1 mL of bis-acrylamide (40%), 50 μ L of ammonium persulfate (10%, w/v), and 10 μ L of TEMED. The solution was poured to the top of the glass plate and the comb was inserted to create wells. The gel was left for ~10 min. For native gels, SDS was replaced with water. Running buffer was prepared by diluting 3.0 g of Tris HCl, 1 g of SDS, and 14.4 g of glycine to 1L with ddH₂O. SDS was not added to running buffer for native gels.

Time-correlated single photon counting measurements

Time-resolved fluorescence was acquired using the Time-Correlated Single Photon Counting method (TCSPC). Picosecond pulsed diode lasers were used to excite the samples. The detector was a high speed microchannel plate photomultiplier tube (Hamamatsu R3809U-50) cooled to -20 °C to reduce noise. The pulses were communicated to a hardware controller by a constant fraction discriminator (CFD). A

second CFD was used to obtain a timing reference pulse from the light source. The time-amplitude-converter output voltage was sent through a biased amplifier with a variable gain and a variable offset and the amplified signal was fed to the analog-to-digital converter. A multichannel analyzer software (Edinburgh Instruments F900) was used to process the signal and convert it to a PC format. Fluorescence lifetime data was fit using the program FFIT provided by professor Nikolai Tkachenko at the Tampere University of Technology (Tampere, Finland). The instrument response functions (IRF) were measured and used to deconvolute the fluorescence decay.

Transient absorption spectroscopy measurements (μ s-s)

In the present study, a custom-built kinetic setup based on ANDOR and Basler Vision microarray imaging cameras was used, allowing the broadband TA measurements with 1 μ s time resolution after a single pulse excitation. This set-up, previously used to study cytochrome c oxidase,⁷²⁻⁷⁴ is located at the University of Helsinki (Helsinki, Finland) where measurements were performed. A pulsed 150 W xenon arc lamp (Applied Photophysics, Surrey, U.K.) was used as the probe light source. After passing through the sample, the probe light was directed using a fiber optic cable (300 μ m, UV-VIS XSR solarization-resistant, Ocean Optics, Dunedin, FL) to either of the two detectors incorporated into one setup. A Triax-180 compact imaging spectrometer (HORIBA Jobin Yvon, Edison, NJ) delivers spectral imaging over a fast kinetic CCD matrix (DV420-UV-FK; Andor Technology, Belfast City, Ireland) to allow recording absorption change surfaces with a time resolution of 1–16 μ s between the spectra. The slower reaction on a time scale from tens of microseconds to minutes was measured with an in-house-built spectrometer based on Sprint spL 2,048–140 km linear scan camera (Basler vision

technologies, time resolution, 12 μs between the spectra). The wavelength-time-absorption data surfaces from these two detectors were combined into a single surface containing the absorbance changes developed after the laser flash. The setup was operated by software written by Nikolai Belevich (University of Helsinki, Helsinki, Finland).

Photolysis of the proteins was achieved with single-flash laser excitation at 532 nm (maximum energy, 340 mJ/cm^2 , 50 mm^2 spot area, 4 ns per pulse) provided by a 2nd harmonic generator attached to a Q-switched Nd-YAG laser (Brilliant B, Quatel, Les Ulis, France). The laser beam was focused, using a pair of cylindrical quartz lenses, on the larger side of a quartz fluorescence microcuvette (10 x 2 mm optical path, Hellma Analytics, Müllheim, Germany) and covered 10 x 2 mm area of the sample. The laser-illuminated spot was slightly larger than the sample area exposed to the probe light, lessening the possibility of slow, diffusion-related artifacts. Each data surface was an average of 10-25 laser flashes. Fresh, dark-adapted sample (The optical density of each sample was set to 1 at the λ_{max}) was taken every time for the flash excitation during averaging, so that each sample was illuminated only once. The sample was exposed to the probe light ~ 0.5 ms prior to the flash excitation using a mechanical shutter (Uniblitz LS2, 2 mm aperture, 300 μs opening time, Vincent Associates, Rochester, NY) to minimize the actinic effect of the white light. All measurements were performed at ambient temperature.

The wavelength-time-absorption surfaces of TA changes in the 1 μs – 1 min time window following the photolysis were decomposed into a multiexponential decay function (Equation 2.1) using a global fit algorithm:

$$\Delta A(t, \lambda) = \sum_i \varepsilon_i(\lambda) \exp(-t/\tau_i) \quad (\text{Eq. 2.1})$$

where $\Delta A(t, \lambda)$ is the optical absorption change at time t ($t = 0$ at the instance of laser flash) and at wavelength λ , and $\varepsilon_i(\lambda)$ and τ_i are the characteristic spectrum and time constant for the i -th exponential decay component, respectively. The global data fit with a sequential reaction model⁷⁵ (reaction consisting of several sequential, irreversible steps) using an algorithm previously described.⁷⁶ All data treatment was performed in MATLAB (version 7.8, MathWorks, Natick, MA). For H₂O₂ experiments, the measurements were recorded within 1 min after addition of H₂O₂.

Transient absorption spectroscopy measurements (ps-fs)

TA spectroscopy measurements were performed in Dr. Joseph Perry's lab (GA Tech, Atlanta, US). Spectra were acquired using a commercial TA spectroscopy system (Newport, Helios). This system accepts two input laser beams, one of variable wavelength used as the pump beam and one of a fixed wavelength used to generate the probe beam in a proprietary nonlinear optical crystal. All experiments were performed using the TOPAS output at 532 nm with a pulse width of 100 fs. A small portion (~5%) of a Ti:Sapphire regenerative amplifier (Newport, Spitfire, 800 nm, 1 kHz, Spectra-physics) provided the probe pulse to generate the white-light continuum (WLC, 420-850 nm, 850-1650 nm). At these specifications, the instrument response function is approximately 200 fs. At each time point, data were averaged for 2 s. The Helios pump beam was chopped at 500 Hz to obtain pumped (signal) and non-pumped (reference) absorption spectra of the sample. A correction factor for chirp in the probe beam was generated using the ultrafast response of CCl₄, and was applied to all data sets. The data

were stored as 3-D wavelength-time-absorbance matrices that were exported for use with the fitting software. The protein solutions had an OD₅₃₂ of 0.5 in 2 mm path-length cuvettes and were stirred continually throughout the data acquisition. The average pump intensity was ~180 mW/cm².

Isotopic measurements

For the kinetic measurements in D₂O, the concentrated protein samples were diluted in 99.9% D₂O-based PBS buffer (pD 7.5); the final H₂O concentration in the samples did not exceed 2%. pD was adjusted with DCl or KOD, taking into account the typical pH correction for the pH glass electrode: $pD = pH^{app}(D_2O) - 0.4$.⁷⁷ The samples were incubated for 24 h in the D₂O medium before measurements.

Anaerobic/aerobic measurements

Anaerobic samples were prepared using a gas/vacuum line of local design. A 4 x 10 x 30 mm fluorescence quartz cell was sealed to a Kimble-Kontes high-vacuum stopcock, which had a vacuum O-ring connection to the vacuum line. As a typical degassing procedure, 20 cycles of exchanging vacuum (10⁻³ bar) and pure Ar were followed by shaking the cell filled with Ar for 15 min on an orbital shaker; then the procedure was repeated 2 more times. 99.99% Ar was additionally purified using the Agilent Technologies BOT-2 and IOT oxygen scrubbers. Aerobic samples were bubbled with oxygen for 10 min before TA measurements.

Hydrogen peroxide measurements

All measurements with the Amplex® Red reagent (Invitrogen) were performed in a micro cuvette (5 mm path length) with 500 µL as the total volume. Prior to use, the

Amplex® Red reagent (Component A, blue cap) was dissolved in 60 mL of DMSO (Component B, green cap). Reaction buffer 1X (50 mM phosphate) was prepared by diluting the 5X reaction buffer (Component C, white cap). The contents of the vial of horseradish peroxidase (HRP, Component D, yellow cap) were dissolved in 1.0 mL of 1X reaction buffer to yield a stock solution of HRP (10 U/mL of HRP). The working solution of Amplex® Red reagent was prepared by mixing 4.85 mL of 1X reaction buffer, 50 μ L of the Amplex® Red reagent stock solution, and 100 μ L of the HRP stock solution. A 20 mM working solution of H₂O₂ was prepared by diluting 22.7 μ L of 3.0% H₂O₂ (Component E, red cap) into 977 μ L of 1X reaction buffer. Serial dilutions of the 20 mM H₂O₂ solution were used for the standard curve. H₂O₂ concentrations were measured by mixing 250 μ L of the sample with 250 μ L of the working solution of Amplex® Red reagent. The reactions were incubated at room temperature for 30 minutes in the dark. Fluorescence measurements were recorded using the Fluorolog 3 spectrofluorometer (Horiba, λ_{ex} =530 nm). To measure H₂O₂ production by KillerRed, 3 mL of protein solution (OD₅₈₅=0.7) was irradiated using a carousel photoreactor equipped with a Hanovia 450 W medium pressure mercury lamp. A 520 nm cutoff filter was used, so only the 546 nm and 578 nm Hg emission lines were utilized. Aliquots (250 μ L) were removed from the 3 mL of protein solution at each time point, and mixed with 250 μ L of the working solution of Amplex® Red reagent. The reactions were incubated at room temperature for 30 minutes in the dark and then the fluorescence was measured. For steady state absorption spectra of the proteins with H₂O₂, the sample was left for 60 min before the measurement was taken.

Singlet oxygen determination by direct spectroscopic method

Singlet oxygen generation was detected by its characteristic phosphorescence at 1270 nm using a North Coast Scientific EO-817P germanium photodiode detector. A frequency-doubled Nd:YAG laser (Continuum Surelite I-10) was used as the excitation source providing 1–10 mJ per pump pulse at the sample at 532 nm with a pulse duration of around 10 ns. The standard $^1\text{O}_2$ photosensitizer *meso*-Tetra(4-sulfonatophenyl)porphine (TPPS₄, Sigma Aldrich, $\Phi_{\Delta} = 0.7$)⁷⁸ was used to ensure that 1270 nm phosphorescence is readily detectable at these conditions. Measurements were performed by Dr. Marina Kuimova at the Imperial College London (London, UK).

Radical trapping using TEMPO-9-ac

The free radical probe 4-((9-acridinecarbonyl)amino)-2,2,6,6-tetramethylpiperidin-1-oxyl (TEMPO-9-ac), obtained from Invitrogen (Carlsbad, CA), was used for the detection of radicals. Comparison of radical generation from KillerRed and DsRed was shown using TEMPO-9-ac. Separately, KillerRed (8 μM) and DsRed (8 μM) were irradiated in the presence of 20 μM TEMPO-9-ac using a frequency-doubled Nd:YAG laser ($\lambda = 532$ nm, 5 mW/cm²) under identical conditions (power*time/abs). For all other TEMPO-9-ac experiments, samples were irradiated using the Hanovia carousel photoreactor equipped with a 450 W medium pressure mercury lamp. A 520 nm cutoff filter was used, so only the 546 nm and 578 nm Hg emission lines were utilized.

EPR studies

EPR measurements were performed in Dr. Malcolm Forbes' lab (UNC, Charlotte, NC). EPR spectra were obtained with a JEOL model FA-100 operating at X-band (9.39 GHz). The ESR spectrometer settings were: modulation frequency, 100 kHz; modulation

amplitude, 3 G; microwave power, 1 mW; receiver gain, 3.99×10^6 and time constant 0.3 s. Samples were excited using a Continuum Powerlite YAG laser pumping a Continuum OPO. The RFPs were excited at 560 nm while EGFP was excited at 480 nm. Immediately after irradiation, samples were analyzed by EPR at room temperature.

Electrospray ionization mass spectrometry

Electrospray mass spectra were acquired in positive ion mode on a quadrupole/orthogonal acceleration time-of-flight mass spectrometer (Applied Biosystems QSTAR-XL). Samples were infused with a flow rate of $5 \mu\text{L}/\text{min}$ in a mixture of water:acetonitrile (1:1) with 0.1% formic acid. Capillary voltage was set to 3000 V and a cone voltage of 35 V was used. The masses of the compounds were obtained by deconvolution of the spectra using the MaxEnt algorithm of the Masslynx software.

Results

First, the spectral behavior of the RFPs is described. KillerRed and mRFP both have absorption and emission maxima at 585 nm and 609 nm (Figure 2.2), respectively. Irradiation (532 nm, $340 \text{ mW}/\text{cm}^2$, pulsed laser, 4 ns per pulse) of mRFP resulted in a hypsochromic shift of the main absorption peak while no shift was seen for KillerRed. KillerRed's main absorption peak decreased with an isosbestic point at 488 nm and an overall increase in absorbance below this point (Figure 2.2). DsRed has absorption and emission maxima of 561 nm and 595 nm respectively, which were close to the previously reported values.¹⁴ Irradiation of DsRed resulted in a redshift of the main absorption peak (Figure 2.2) due to production of the decarboxylated photoproduct.¹⁴

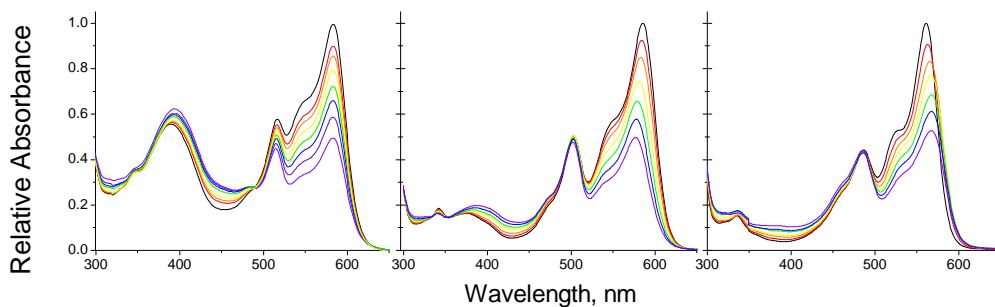


Figure 2.2. Photobleaching of KillerRed (left, isobestic point at 488 nm), mRFP (middle), and DsRed (right) with 532 nm pulsed laser (340 mW/cm², pulsed laser, 4 ns per pulse, 50-100 pulses per spectrum).

Singlet oxygen phosphorescence experiments

Production of ¹O₂ was determined from its characteristic phosphorescence at 1270 nm. Porphyrin TPPS₄ (*meso*-tetra(4-sulfonatophenyl)porphine), which absorbs significantly at 532 nm, was employed as a standard sensitizer to ensure that under these experimental conditions singlet oxygen phosphorescence at 1270 nm was easily observable. D₂O was used as a solvent for KillerRed to enhance the efficiency of the 1270 nm phosphorescence, since the lifetime of singlet oxygen in H₂O is significantly shorter than in D₂O (3.5 μs in H₂O vs 64 μs in D₂O).⁷⁰ As expected, an intense characteristic signal of ¹O₂ was observed following excitation of TPPS₄ (Figure 2.3). A phosphorescence signal was also detected following 532 nm excitation of KillerRed (Figure 2.3); however, careful spectral analysis (see below) shows that the signal is from the protein and not ¹O₂.

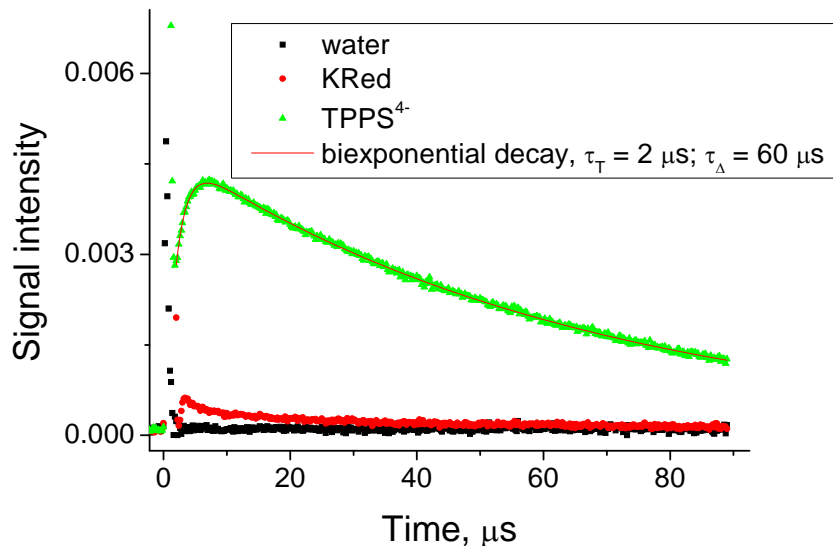


Figure 2.3. Time resolved traces at 1270 nm recorded for pure D₂O, KillerRed and standard photosensitizer TPPS₄ following 532 nm excitation. A₅₃₂ nm = 0.1 for the dye solution and KillerRed.

It is known that the phosphorescence spectrum of ¹O₂ is quite narrow, and no appreciable signal at 1200 nm should be detected (Figure 2.4). Using the 1200 nm narrow band filter, control experiments were performed which compared the phosphorescence at 1270 nm to that at 1200 nm. This is a straightforward way to distinguish the ¹O₂ emission from the triplet decay of the photosensitizer, which sometimes tails off to 1200 nm. The signal at 1200 nm for KillerRed is in fact several times more intense than at 1270 nm (Figure 2.4), and has exactly the same decay. Furthermore, the signal is reduced upon increase of the H₂O/D₂O ratio (Figure 2.5), repeating the same trend as seen at 1270 nm. Thus the signal at 1270 nm is simply the tail of the more blue-shifted signal, most likely the triplet state of KillerRed. The best fit of the signal from KillerRed was achieved with a tri-exponential fit with lifetimes of 4 ns, 3 μs, and 40 μs (Figure 2.6). The 4 ns lifetime is attributed to the rise time of the phosphorescence. Because both the green and

red forms of KillerRed absorb at 532 nm (Figure 2.2), the 3 μ s and 4 μ s phases are likely due to excitation of both forms. These data show that no singlet oxygen could be detected from KillerRed in the direct experiment. These results agree with unpublished results of Ragas who failed to detect singlet oxygen production from KillerRed.⁷⁹

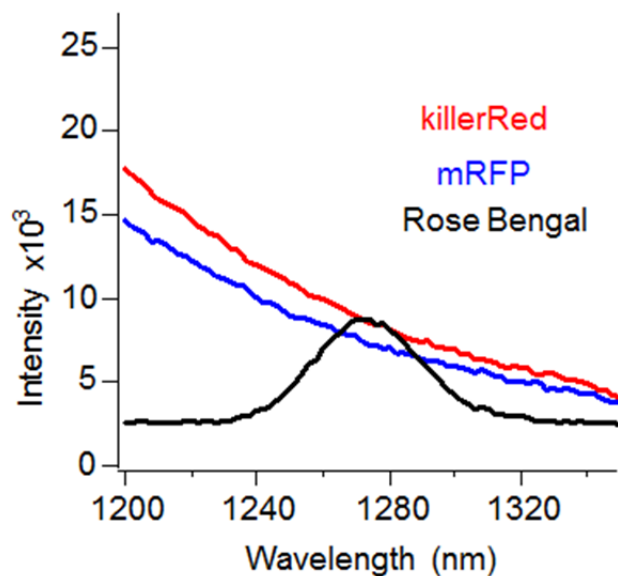


Figure 2.4. Steady state luminescence spectra ($\lambda_{\text{ex}} = 550$ nm) of $^1\text{O}_2$ (by excitation of RoseBengal, black line), mRFP (blue line), and KillerRed (red line).

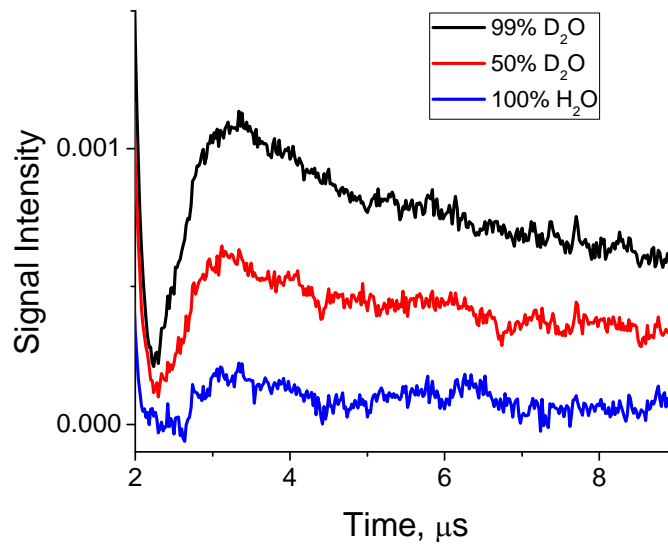


Figure 2.5. Phosphorescence decay of KillerRed at 1270 nm in 99% D₂O (black), 50% D₂O (red), and 100% H₂O (blue) following 532 nm excitation.

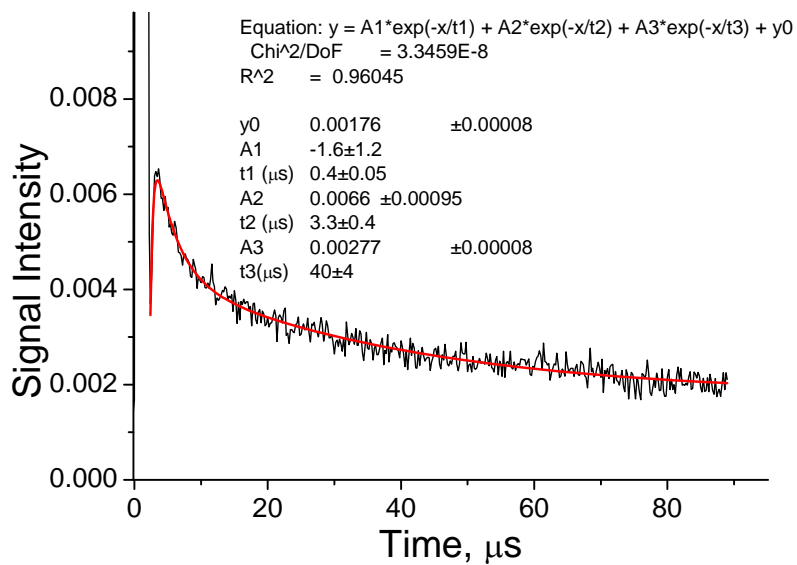


Figure 2.6. KillerRed phosphorescence signal at 1270 nm in PBS fit to a 3-exponential model.

Fluorescent probe measurements

Type I sensitization assumes the formation of radicals via electron transfer (reductive or oxidative) involving the triplet state of the photosensitizer. Therefore, the free radical probe TEMPO-9-ac, which captures mostly long-lived carbon- or sulfur-centered radicals, was employed for the detection of radicals. The nitroxide moiety of TEMPO-9-ac quenches the fluorescence of the acridine; however, upon radical trapping this fluorescence is restored (Figure 2.7). Irradiation of KillerRed (13 μM) in the presence of TEMPO-9-ac (20 μM) generated a large increase in signal from TEMPO-9-ac (Figure 2.8), indicating radical production. No increase was seen for the control experiment containing only TEMPO-9-ac in PBS buffer (Figure 2.9). To determine the effect of oxygen on the radical production, a solution containing KillerRed and TEMPO-9-ac was bubbled with either oxygen or nitrogen and then irradiated (Figure 2.10). The sample depleted of oxygen showed less of an increase of TEMPO-9-ac fluorescence over that which was oxygen saturated (Figure 2.10). Altogether, these data showed that the phototoxicity of KillerRed stems from an oxygen dependent type I photosensitization mechanism and that ROS production is accompanied by bleaching (Figures 2.11 and 2.12).

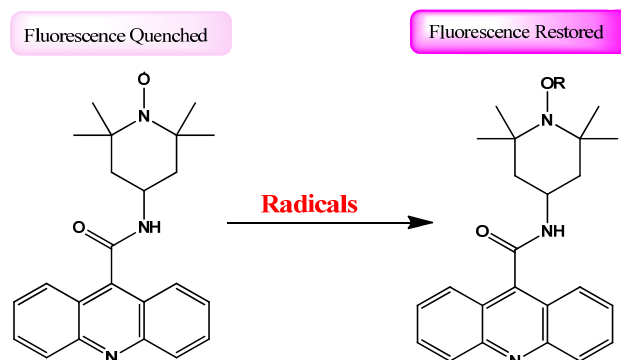


Figure 2.7. The fluorescence of TEMPO-9-ac is initially quenched by the nitroxide moiety. Upon radical trapping, that fluorescence is restored ($\lambda_{\text{ex/em}} = 358/440$ nm). Radical trapping can also be monitored by EPR spectroscopy.

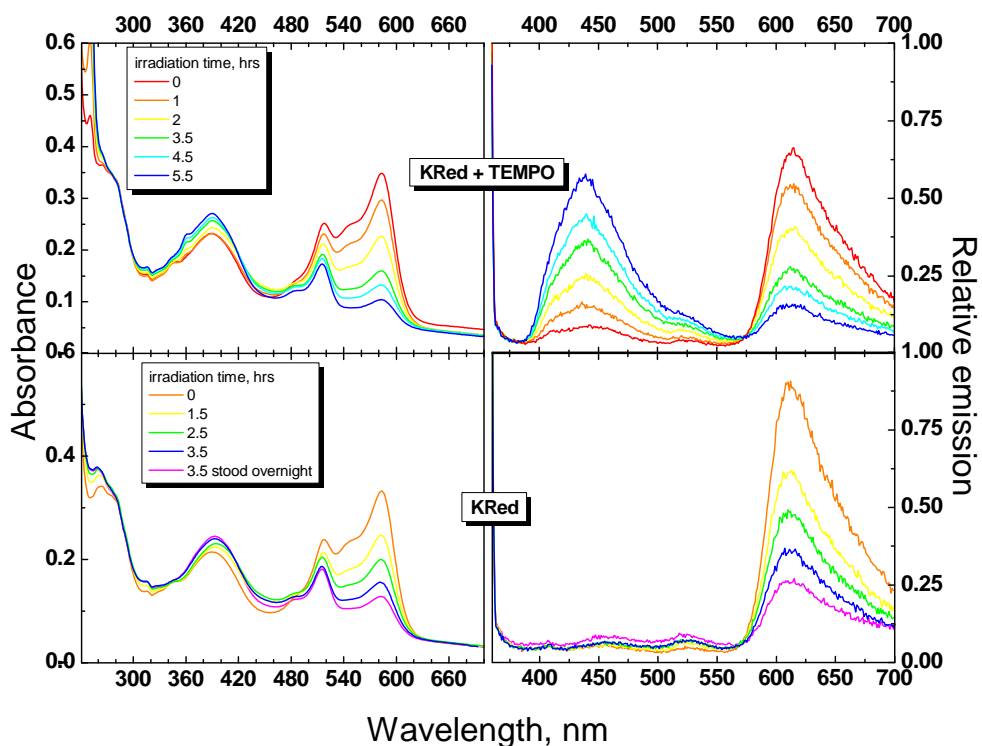


Figure 2.8. Absorption (left) and emission (right) spectra ($\lambda_{\text{ex}} = 358$ nm) of KillerRed irradiated at various time intervals using Hanovia carousel photoreactor (see Materials and Methods). Samples were with (top) and without (bottom) radical fluorescence probe TEMPO-9-ac.

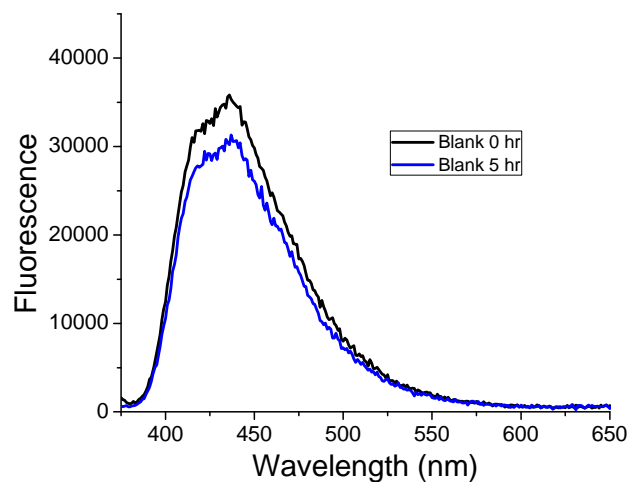


Figure 2.9. Fluorescence spectra of TEMPO-9ac (20 μM) in PBS before (black line) and after (blue line) irradiation with Hanovia carousel photoreactor (see Materials and Methods).

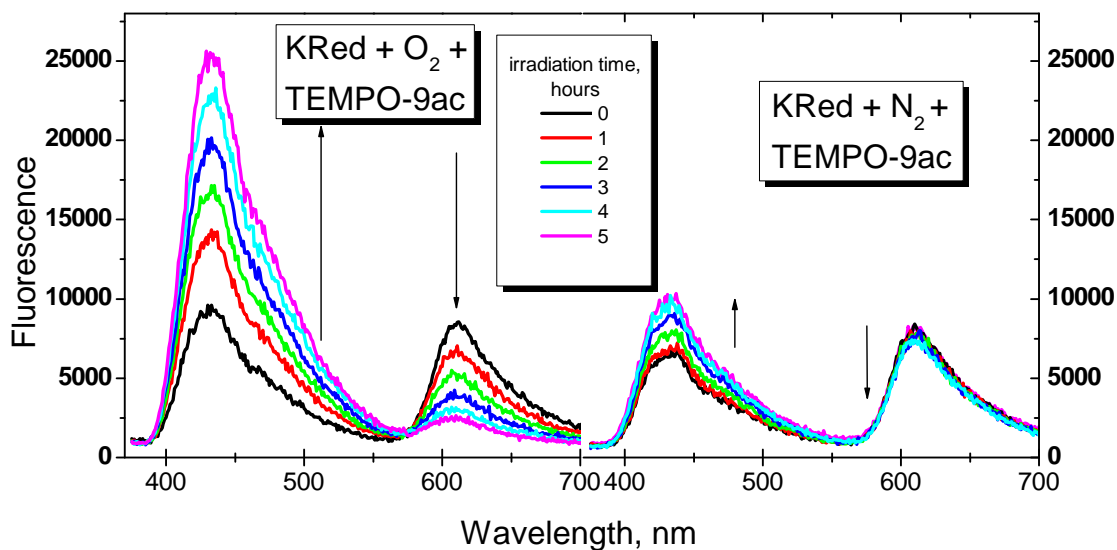


Figure 2.10. Fluorescence spectra ($\lambda_{\text{ex}} = 358 \text{ nm}$) of KillerRed and TEMPO-9ac irradiated with Hanovia carousel photoreactor (see Materials and Methods) at 1 hr intervals. Left graph – the sample bubbled with oxygen, right graph – the sample bubbled with nitrogen.

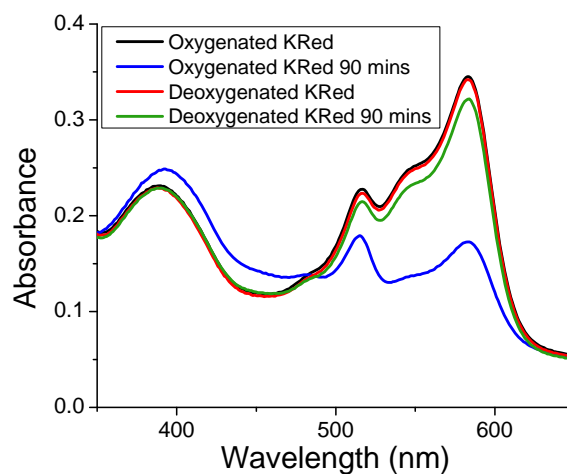


Figure 2.11. Absorption spectra of KillerRed before and after 90 min of irradiation with Hanovia carousel photoreactor (see Materials and Methods). Samples were bubbled with either oxygen or nitrogen.

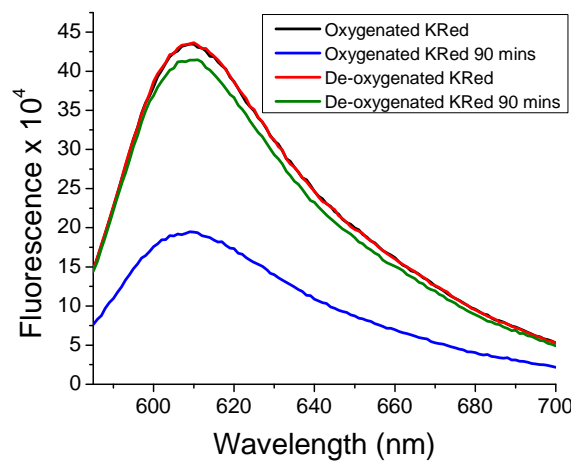


Figure 2.12. Emission spectra ($\lambda_{\text{ex}} = 565 \text{ nm}$) of KillerRed before and after 90 min irradiation with Hanovia carousel photoreactor (see Materials and Methods). Samples were bubbled with either oxygen or nitrogen.

Comparison of radical generation by KillerRed and DsRed using TEMPO-9-ac demonstrated that KillerRed produces 10-fold more radicals than does DsRed (Figure 2.13). The absorbance of the proteins was set to the same optical density at 532 nm to

ensure the same dosage of light (Figure 2.14). A response was also observed upon irradiation of mRFP with TEMPO-9-ac (Figure 2.15), indicating radical production; therefore, mRFP was tested for its phototoxic effects using *in vitro* studies. Separately, KillerRed and mRFP were each fused to β -galactosidase and irradiated at various time intervals using the 548 and 576 nm Hg emission lines of a Hanovia photoreactor (see materials and methods). β -Galactosidase activity was measured by hydrolysis of the chromogenic substrate *o*-nitrophenyl- β -D-galactoside to produce *o*-nitrophenolate (ONPG, λ_{max} 420 nm).⁸⁰ β -Galactosidase was deactivated 50% by KillerRed and 30% by mRFP, while the control showed an 18% decrease in activity after 8 hours of irradiation (Figure 2.16). Therefore, *in vitro* studies show that mRFP is phototoxic, but to a lesser extent than KillerRed.

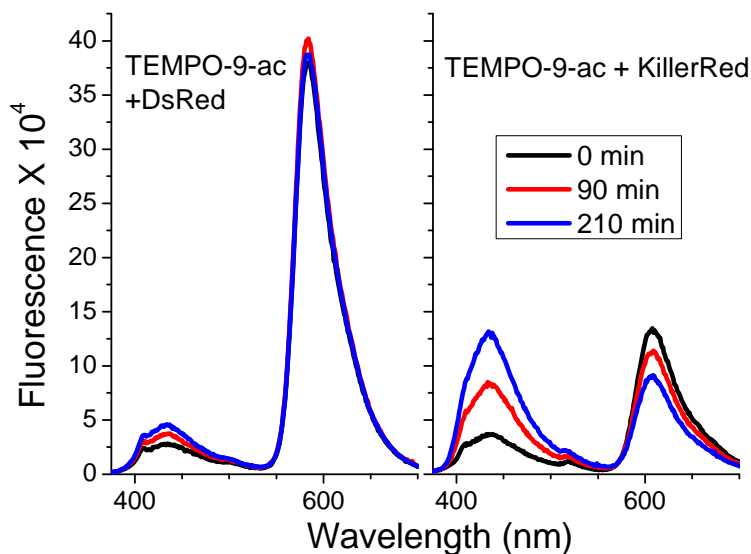


Figure 2.13. Emission spectra ($\lambda_{\text{ex}}=358\text{nm}$) of DsRed (left) and KillerRed (right) in the presence of TEMPO-9ac ($20\ \mu\text{M}$) irradiated with a 532 nm laser ($5\ \text{mW}/\text{cm}^2$).

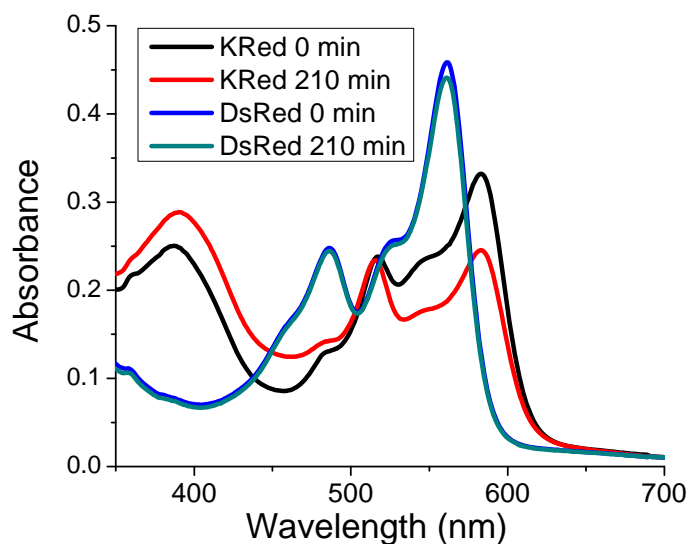


Figure 2.14. Absorption spectra of KillerRed and DsRed in the presence of TEMPO-9ac irradiated with a 532 nm laser (5 mW/cm^2).

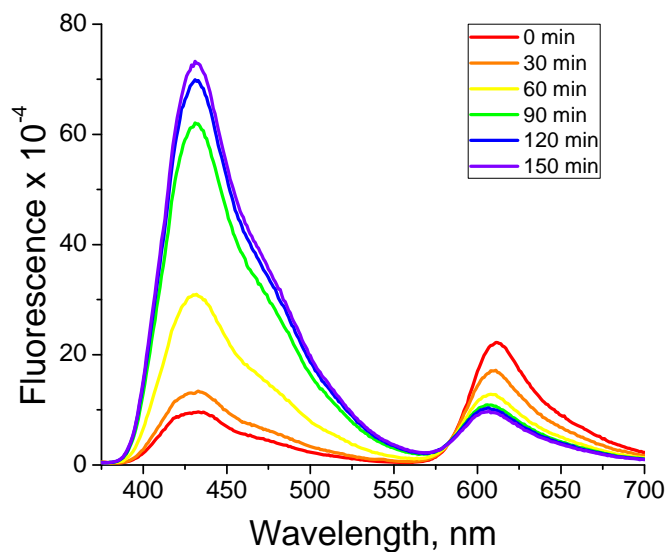


Figure 2.15. mRFP ($10 \mu\text{M}$) and TEMPO-9ac ($20\mu\text{M}$) irradiated using a Hanovia carousel photoreactor (see Materials and Methods). An increase in TEMPO-9-ac fluorescence indicates the production of radicals.

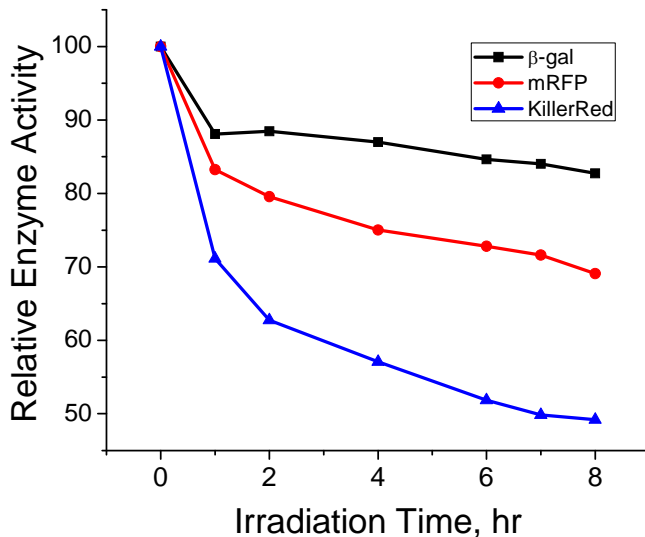


Figure 2.16. β -Galactosidase alone or fused to either mRFP or KillerRed and irradiated using Hanovia carousel photoreactor (see Materials and Methods).

Although it has been demonstrated that the phototoxicity of KillerRed is linked to radical production, the identity of the radical(s) remains elusive. Therefore, the probes 3'-(*p*-aminophenyl) fluorescein (APF) and 3'-(*p*-hydroxyphenyl) fluorescein (HPF) were employed because they can distinguish specific ROS based on the ratio of the fluorescence response of the two compounds (Table 2.2 and Figure 2.17).⁸¹ These probes are known to selectively and dose-dependently detect certain species among ROS and are resistant to light-induced autoxidation. Excitation of KillerRed in the presence of either probe resulted in a large increase in fluorescein fluorescence (Figure 2.18) compared to that of the controls (Figure 2.19). The largest fluorescence response was seen when KillerRed was irradiated in the presence of APF. From the ratio of the fluorescence response the identity of the ROS could not be determined because it did not match any of the ratios in Table 2.2. A likely reason for this is that a variety of ROS are produced or

that the radical being trapped is not one found on Table 2.2. The role of O₂ in the production of ROS was also investigated using APF. KillerRed and APF were irradiated in the presence and absence of O₂. As expected, a larger fluorescence response from the probe APF was seen in the presence of O₂ (Figure 2.20).

Table 2.2. Fluorescence response of APF and HPF to various reactive oxygen species.

ROS	ROS Generation Method	APF	HPF
Hydroxyl Radical	100 μM ferrous perchlorate (II) and 1 mM H ₂ O ₂	1200	730
Singlet Oxygen	100 μM of 3-(1,4-dihydro-1,4-epidioxy-1-naphthyl) propionic acid	9	5
Superoxide	100 μM KO ₂	6	8
Peroxy Radical	100 μM of 2,2'-azobis(2-amidinopropane),dihydrochloride (AAPH)	2	17
Hydrogen Peroxide	100 μM H ₂ O ₂	<1	2
Auto-oxidation	2.5 hours exposure to fluorescent light source	<1	<1

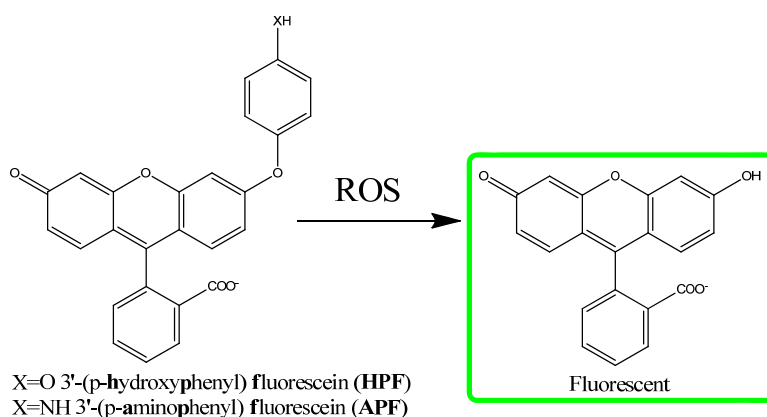


Figure 2.17. Reaction of HPF or APF with various ROS produces the fluorescent compound fluorescein ($\lambda_{\text{ex/em}} = 490/515 \text{ nm}$).

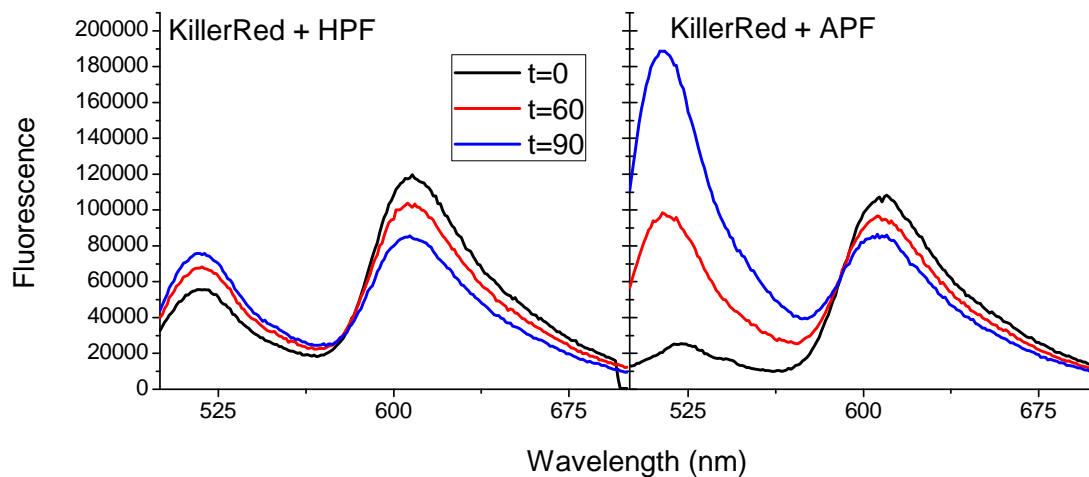


Figure 2.18. Emission spectra of KillerRed (13 μM) in the presence of HPF (left) and APF (right) irradiated with Hanovia carousel photoreactor (see Materials and Methods) at various times ($\lambda_{\text{ex}} = 490 \text{ nm}$).

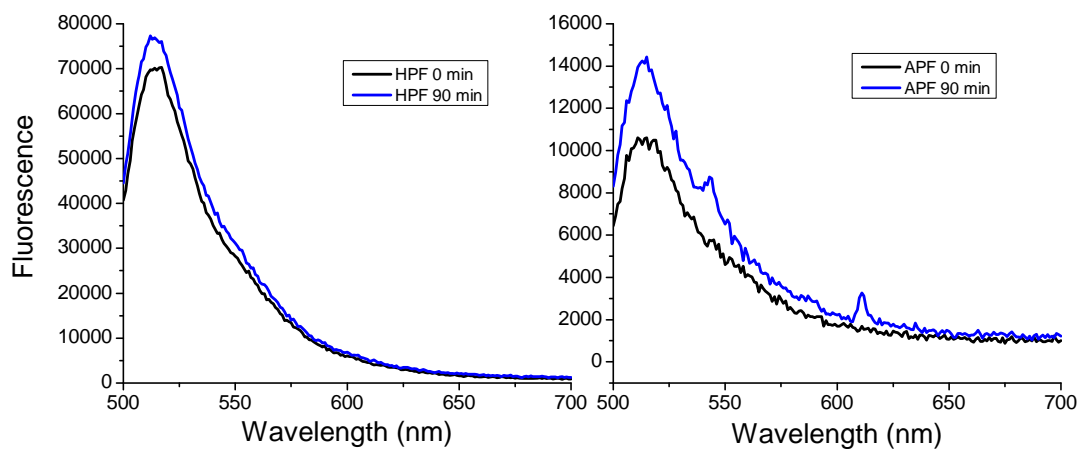


Figure 2.19. Fluorescence spectra ($\lambda_{\text{ex}} = 490 \text{ nm}$) of HPF (left) and APF (right) in PBS before (black) and after (blue) irradiation with Hanovia carousel photoreactor (see Materials and Methods).

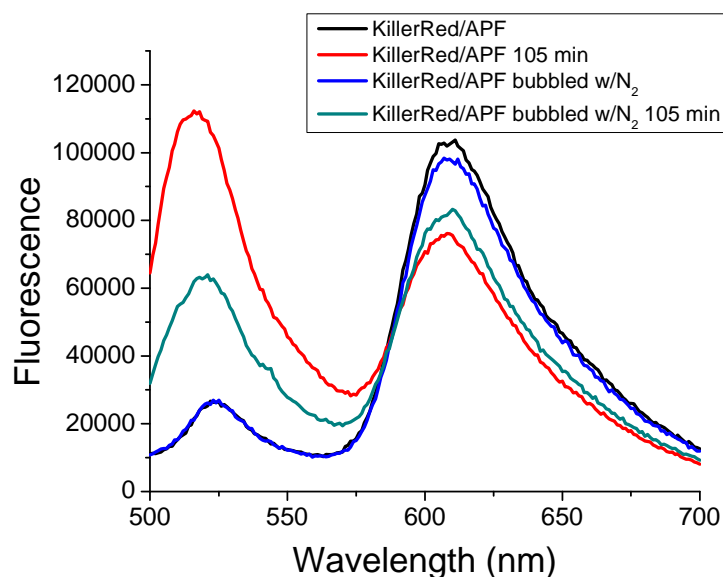


Figure 2.20. Emission spectra of KillerRed (13 μM) and APF (5 μM) in PBS before and after irradiation with Hanovia carousel photoreactor (see Materials and Methods). Samples were bubbled with oxygen or nitrogen ($\lambda_{\text{ex}} = 490 \text{ nm}$).

EPR experiments

In an attempt to identify any short-lived radicals, the spin trap 5,5-dimethyl-1-pyrroline-*N*-oxide (DMPO) was used. DMPO is commonly employed to detect transient free radical species in chemical and biological systems,⁸²⁻⁸⁴ using the hyperfine coupling constants to characterize the radicals.^{85,86} This trap is used to detect superoxide, hydroxyl, and peroxy radicals due to their short lifetime, which prevents direct detection using steady-state EPR. Irradiation of KillerRed with DMPO resulted in a broad singlet with a peak-to-trough width of 15 Gauss. Further analysis revealed that this radical was a result of irradiation of KillerRed and not adducts of DMPO, since irradiation of KillerRed in PBS gave the same broad singlet (Figure 2.21). As controls, the EPR spectra of non-irradiated KillerRed and irradiated PBS produced no signal. Interestingly, irradiation of DsRed, mRFP,⁵⁶ and EGFP resulted in the same broad singlet as seen in the EPR spectra

(Figure 2.22). Most likely, these stable paramagnetic species either have similar chemical structure, or the protein-based radicals are indistinguishable by our technique. It is noted that decarboxylation of E215 (E222 in wtGFP) in non-phototoxic DsRed can generate radicals.¹³ Although the nature of the radicals detected are still unknown, drawing parallels between the radical generation efficiency observed in this work and the phototoxicity of various proteins detected earlier seems appropriate.^{21,22} Altogether, our data suggest that the phototoxicity of KillerRed occurs primarily through a radical-based type I photosensitization mechanism.

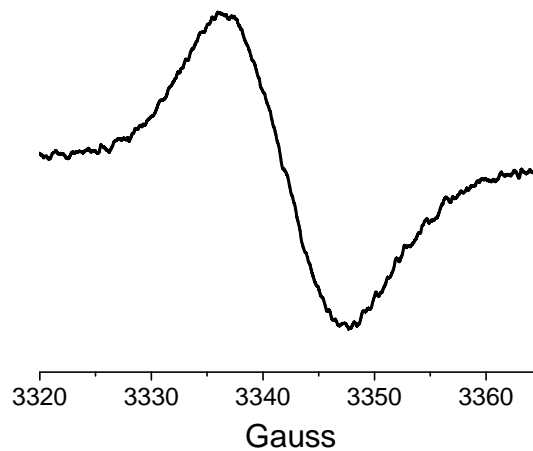


Figure 2.21. EPR spectrum of KillerRed in PBS buffer after 40 min of irradiation with 560 nm (40 mW/cm^2) light using a Continuum Powerlite YAG laser pumping a Continuum OPO.

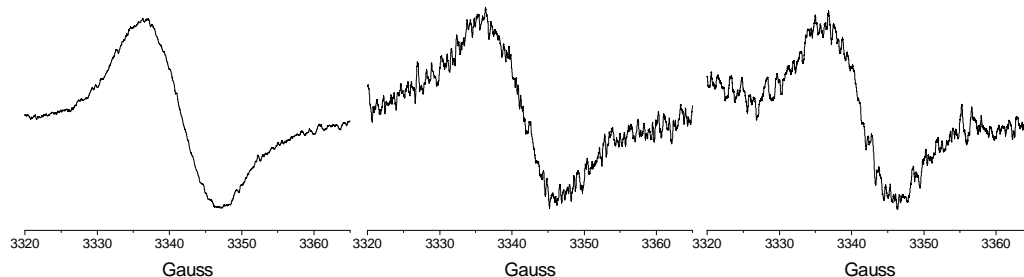
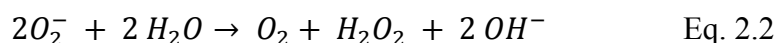


Figure 2.22. From left to right: EPR spectra of mRFP, DsRed, and EGFP obtained after irradiation with 560 nm light (40 mW/cm^2) for RFPs and 480 nm (30 mW/cm^2) for EGFP. Samples were excited using a Continuum Powerlite YAG laser pumping a Continuum OPO.

Hydrogen peroxide measurements

Through these experiments, it has been demonstrated that molecular oxygen actively participates in type I photosensitizing mechanisms. One of the major pathways for such involvement is an electron transfer from the anion radical of the sensitizer to $^3\text{O}_2$ leading to O_2^- formation. In living organisms, the latter is converted enzymatically into O_2 and H_2O_2 by superoxide dismutase (SOD).⁸⁷ In the absence of SOD, O_2^- is capable of radical-based oxidation damage through the Haber-Weiss reaction.⁸⁸ O_2^- is also known to undergo spontaneous dismutation producing H_2O_2 (Equation 2.2).⁸⁹



Therefore, we tested KillerRed for the production of H_2O_2 using the Amplex® Red system.²¹ Fluorescence from the reaction mixture before irradiation was normalized to that for each time interval and subtracted as background. The difference is plotted as the dashed line in Figure 2.23. The small increase in fluorescence at 585 nm is attributed to formation of resorufin, indicating production of H_2O_2 . From the calibration curve (Figure 2.24), one can estimate that the hydrogen peroxide production was below 100 nM. This

gave an overall yield of less than 1% when comparing the molar amount of photobleached protein to H_2O_2 produced.

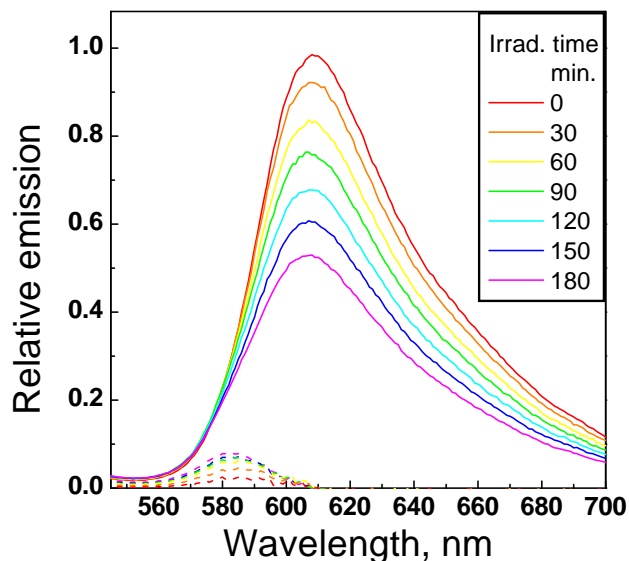


Figure 2.23. Fluorescence emission of KillerRed, Amplex® Red, and horseradish peroxidase after irradiation at different time intervals (solid lines). Dashed lines correspond to the resorufin fluorescence calculated as the difference between the normalized spectra at each time and $t = 0$.

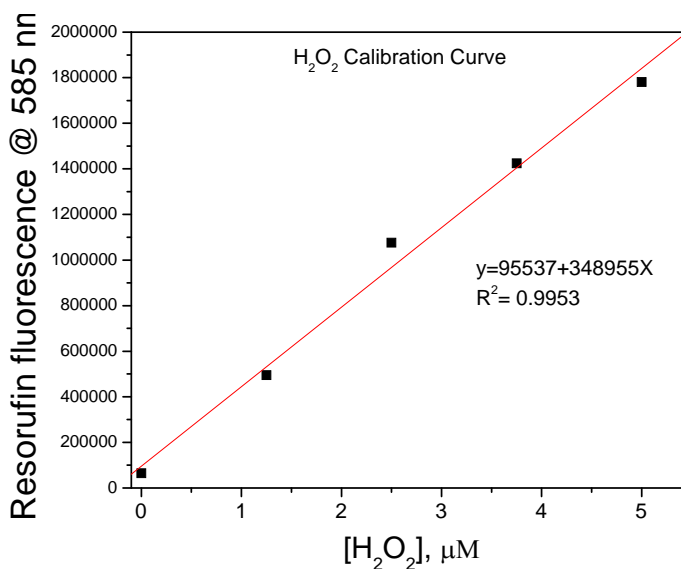


Figure 2.24. Calibration curve for the Amplex® Red assay. Serial dilutions of H_2O_2 were mixed with Amplex® red reagent and allowed to react for 30 min in the dark. This resulted in the formation of resorufin which was detected by its fluorescence at 585 nm. Detection limit: $0.1 \mu\text{M H}_2\text{O}_2$.

A second question is whether or not the production of H_2O_2 was stoichiometric with respect to KillerRed. Due to the very low yield of H_2O_2 (less than 1%), KillerRed was tested for its ability to consume H_2O_2 . Addition of 1 mM H_2O_2 to KillerRed (13 μM) resulted in the consumption of H_2O_2 after 24 hr, as shown by the Amplex® Red system (Figure 2.25). We also investigated the consumption of H_2O_2 by mRFP and EGFP. Both fluorescent proteins consumed H_2O_2 (Figures 2.26 and 2.27), but did not bleach at concentrations of H_2O_2 up to 80-fold that of protein (Figures 2.28 and 2.29). At the same time, the <10% bleaching of the 585 nm absorption peak was observed for KillerRed when concentrations of up to 25-fold were used (Figure 2.30). A control of bovine serum albumin (BSA) subjected to the same conditions did not show any consumption of H_2O_2 (Figure 2.31). This control showed that consumption of H_2O_2 is unique to these fluorescent proteins (KillerRed, mRFP, and DsRed) and that other trace impurities did not contribute to the spontaneous decomposition of H_2O_2 .⁹⁰

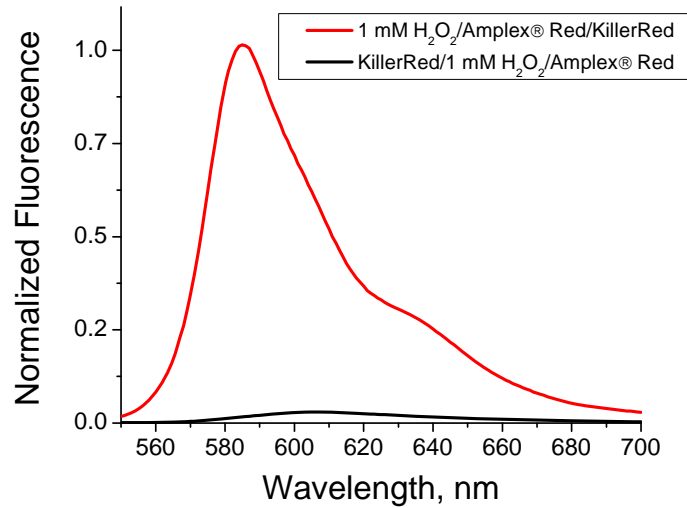


Figure 2.25. Fluorescence spectra for Amplex® Red H₂O₂ Assay. As a control, H₂O₂ (1 mM, final concentration) was added to the Amplex® Red reagent and allowed to react for 30 min and then the fluorescence spectrum was measured (red line). For the sample, KillerRed (13 μM) was incubated with H₂O₂ for 24 hours and then mixed with the Amplex® Red reagent. It was allowed to react for 30 min and then the fluorescence spectrum was measured (black line).

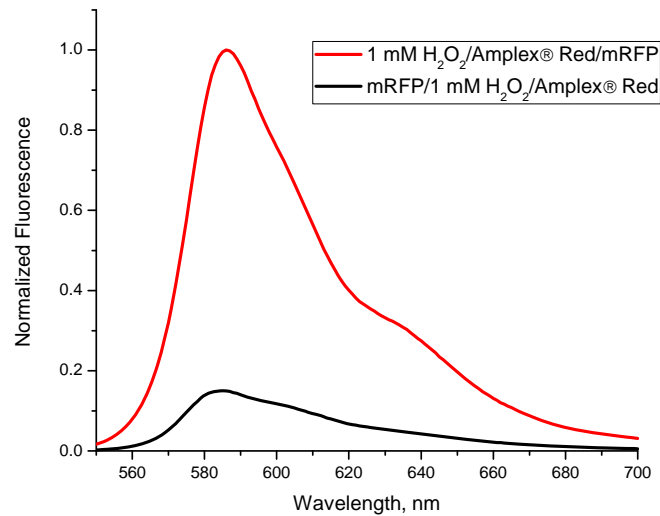


Figure 2.26. Fluorescence spectra for Amplex® Red H₂O₂ Assay. As a control, H₂O₂ (1 mM, final concentration) was added to the Amplex® Red reagent and allowed to react for 30 min and then the fluorescence spectrum was measured (red line). For the sample, mRFP (10 μM) was incubated with H₂O₂ for 24 hours and then mixed with the Amplex® Red reagent. It was allowed to react for 30 min and then the fluorescence spectrum was measured (black line).

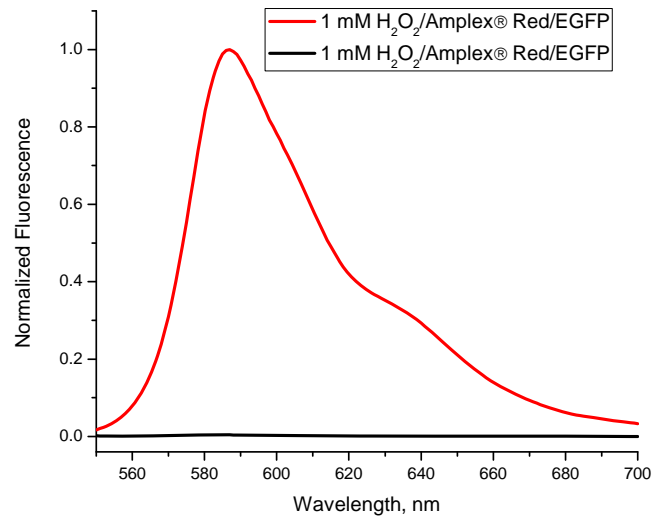


Figure 2.27. Fluorescence spectra for Amplex® Red H_2O_2 Assay. As a control, H_2O_2 (1 mM, final concentration) was added to the Amplex® Red reagent and allowed to react for 30 min and then the fluorescence spectrum was measured (red line). For the sample, EGFP (10 μM) was incubated with H_2O_2 for 24 hours and then mixed with the Amplex® Red reagent. It was allowed to react for 30 min and then the fluorescence spectrum was measured (black line).

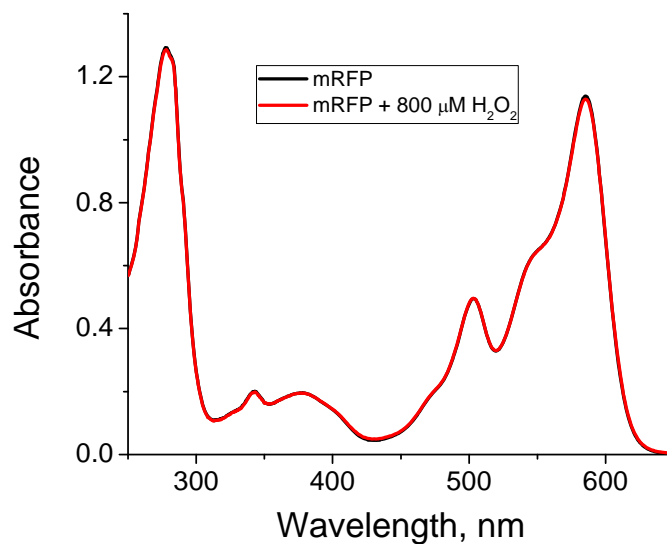


Figure 2.28. Absorption spectra of mRFP before and after addition of 800 μM H_2O_2 .

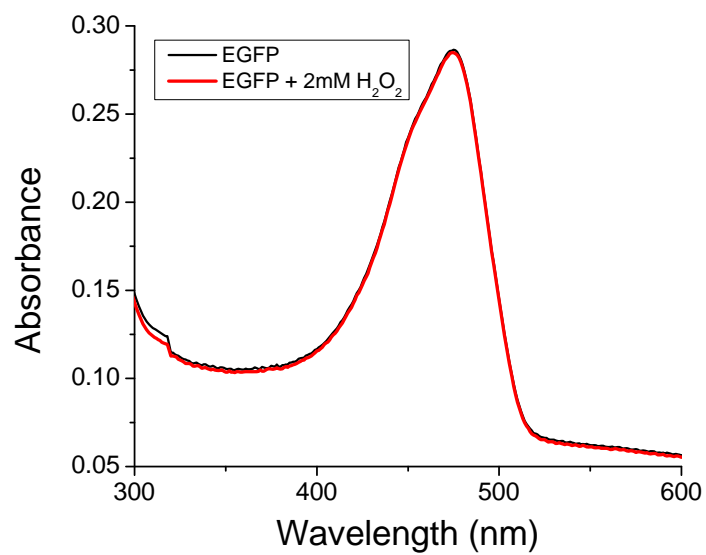


Figure 2.29. Absorption spectra of EGFP before and after addition of 2 mM H₂O₂.

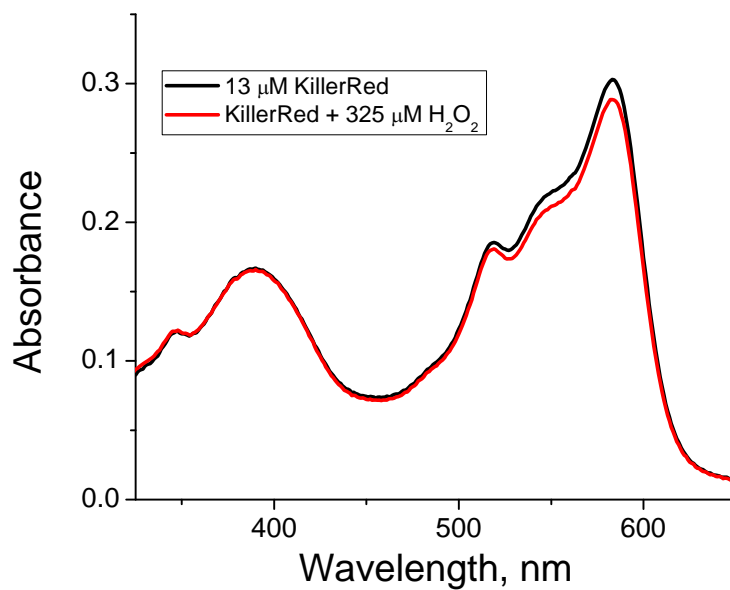


Figure 2.30. Absorption spectra of KillerRed before and after addition of 325 μM H₂O₂.

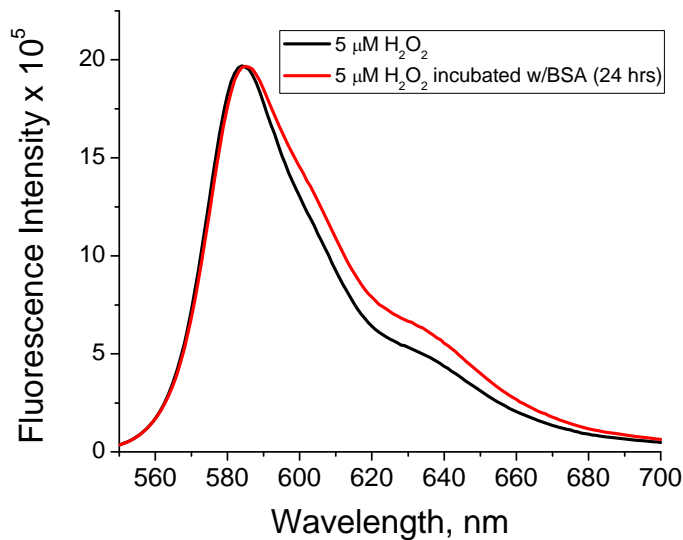


Figure 2.31. Fluorescence spectra of rosorufin formed by addition of Amplex® Red reagent to a solution of 5 μM H_2O_2 (black line) and to a solution containing 5 μM H_2O_2 and 10 μM BSA (red line). The solution containing 5 μM H_2O_2 and 10 μM BSA was incubated for 24 hours before addition of the Amplex® Red reagent.

Mutational analysis

It was previously suggested that N145 and A161 were indispensable for the phototoxicity of KillerRed.²¹ Therefore, these residues were mutated back to the original wild-type residues found in the non-phototoxic chromoprotein anm2CP to generate N145T, A161C, and N145T/A161C. The absorption spectra for the mutant N145T and the double mutant N145T/A161C are shown in Figure 2.32. Many forms of the protein are present in solution as both contain the red (~ 560 nm), green (~ 510 nm), and neutral (~ 400 nm) forms (Figure 2.2). Irradiation of N145T/A161C at 407 nm results in an overall increase in the green and red forms (Figure 2.33) which is likely due to photoswitching between the *Z* and *E* states of the chromophore. Supporting this hypothesis, the chromoprotein anm2CP is proposed to have its chromophore in the *E* state.⁶⁴ From the crystal structure of KillerRed, it is shown that N145 hydrogen bonds

with the chromophore (Figure 2.34). Previous crystal structure analysis, modeling in the side chain of C161, demonstrate that C161 is too close to the residue N145 ($<2.2\text{\AA}$), and therefore, would prevent optimal hydrogen bonding of the latter to the chromophore.⁶⁴ Thus, having a smaller side chain (A161 in KillerRed) eliminates this effect and allows for hydrogen bonding. By 180° rotation of the Y66 side chain around the C^α - C^β bond, Q159 is thought to stabilize the chromophore in the *E* state; thus, hydrogen bonding of N145 to Y66 (*E* state) would compete with that of Q159 to Y66 (*Z* state).⁶⁴ The *Z* state would be more energetically favorable when residue 161 is an alanine (i.e. in KillerRed), allowing for optimal hydrogen bonding between N145 and Y66. The role of Q159 is supported by the mutation Q159G in amn2CP, which results in increased red fluorescence and noticeable phototoxicity.⁶⁴ The combination of *E/Z* isomerization and poor chromophore maturation of the red chromophore explain the importance of these positions and their effect on the phototoxicity of KillerRed.

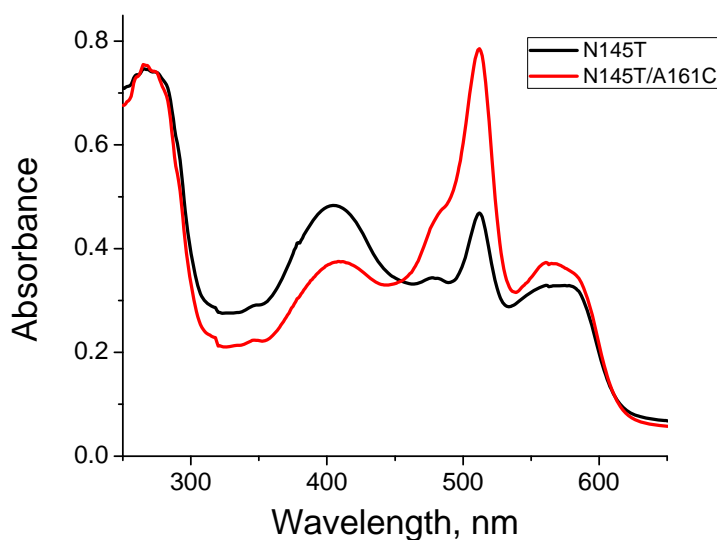


Figure 2.32. Ground state absorption spectra at pH 7.5 for mutants of KillerRed. N145T is shown in black and the double mutant N145T/A161C is shown in red.

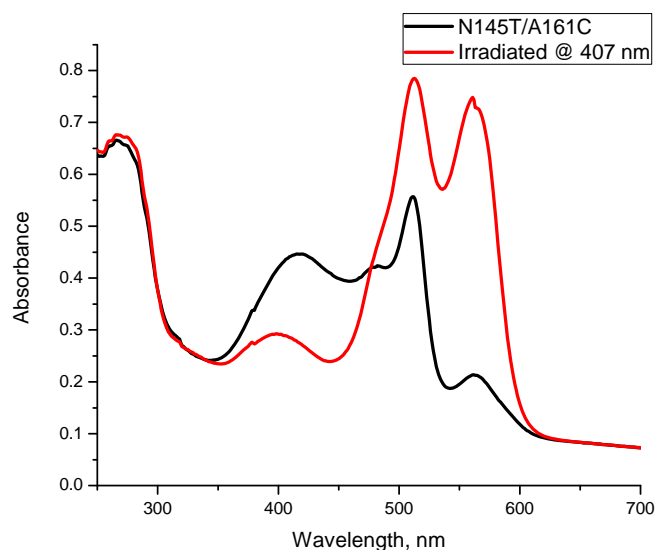


Figure 2.33. Ground state absorption spectra of N145T/A161C at pH 6.5 before (black) and after irradiation (red) with 407 nm light using the emission from a xenon arc lamp coupled to a monochromator (slit width of 2 nm).

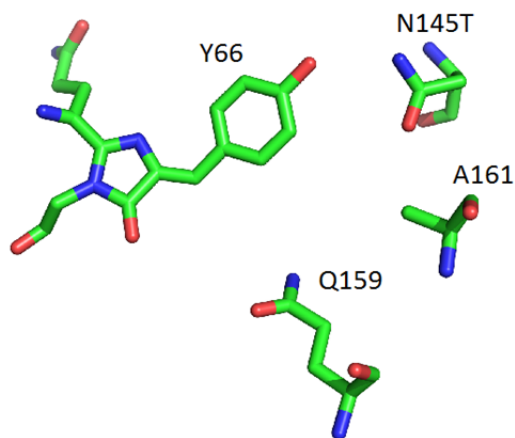


Figure 2.34. Chromophore pocket of KillerRed (PDB 3GB3) illustrating the important residues that favor the Z state. Drawn using the PyMOL Molecular Graphics System, Version 1.2r3pre, Schrödinger, LLC.

Mass spectrometry

Electrospray ionization mass spectrometry (ESI-MS) of bleached and unbleached DsRed, previously reported, demonstrated that photobleaching occurs through

decarboxylation of E215 (E222 in wtGFP). Therefore, this same technique was applied to investigate the mechanisms of bleaching in mRFP and KillerRed. Irradiation of the proteins were carried out in 10 mM ammonium acetate buffer (pH 8.2) using a 532 nm (5 mW/cm²) laser. The mass spectrum of native DsRed contained a peak at 28,319 Da (Figure 2.35). This is consistent with the calculated molecular weight of DsRed taking into account the N-terminal 6xHN tag and polylinker (Appendix A, Table A.1) and the loss of 24 Da for chromophore formation. A peak appeared at 28,278 Da in the mass spectrum of bleached DsRed (Figure 2.36), which is close to the expected mass for decarboxylation (-44 Da); the results of which have been previously published.¹⁴ For KillerRed, the best results were obtained when the protein was run in a 50:50 water:acetonitrile mixture containing 1% formic acid. A peak consistent with the calculated molecular weight (Figure 2.37, 28,961 Da) is present under these conditions; however, other higher and lower molecular weight species are also observed. It should be noted that the protein solution turned yellow in anything containing formic acid. Mass spectra were also obtained in both 50:50 water:acetonitrile and 50:50 water:methanol where the solution remained red in both cases; however, the spectra were noisy and did not yield peaks consistent with the calculated molecular weight. The mass spectrum of native mRFP had two major peaks with molecular weights of 25,196 Da and 25,515 Da (Figure 2.38) which are not consistent with the calculated mass of 27,980 Da. The ESI-MS of bleached mRFP were noisy and the peaks were not well resolved (Figure 2.39). From the SDS-PAGE of KillerRed and mRFP (Figure 2.40), it is shown that multiple bands are present. These bands are attributed to the partial hydrolysis of the main chain acylamine linkage, previously assigned for mRFP.⁵⁶ The SDS-PAGE of induced and non-

induced cell lysate (mRFP, Figure 2.41) demonstrates the presence of the smaller band only when the culture is induced, indicating that this band most likely stems from the protein. KillerRed does not hydrolyze under non-denaturing conditions as seen in Figure 2.42 and is shown to be pure (>95%) for ESI-MS analysis. The noise in the spectra of bleached KillerRed and mRFP suggest the presence of multiple molecular weight species. This is not surprising since the production of ROS can lead to oxidation of amino acid residue side chains, cleavage of peptide bonds, and formation of covalent protein-protein cross-linked derivatives.⁹¹

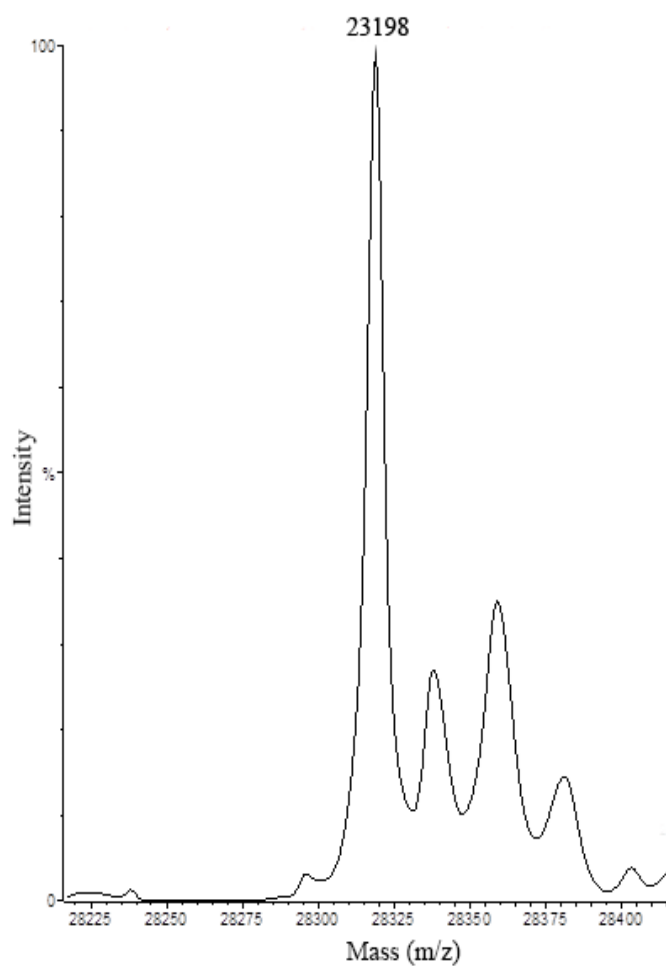


Figure 2.35. Mass spectrum of unbleached DsRed in 10 mM ammonium acetate diluted 1:10 in a 50:50 water:acetonitrile mixture containing 0.1% formic acid. Calculated MW of DsRed is 28,319 Da which includes -24 Da for chromophore formation.

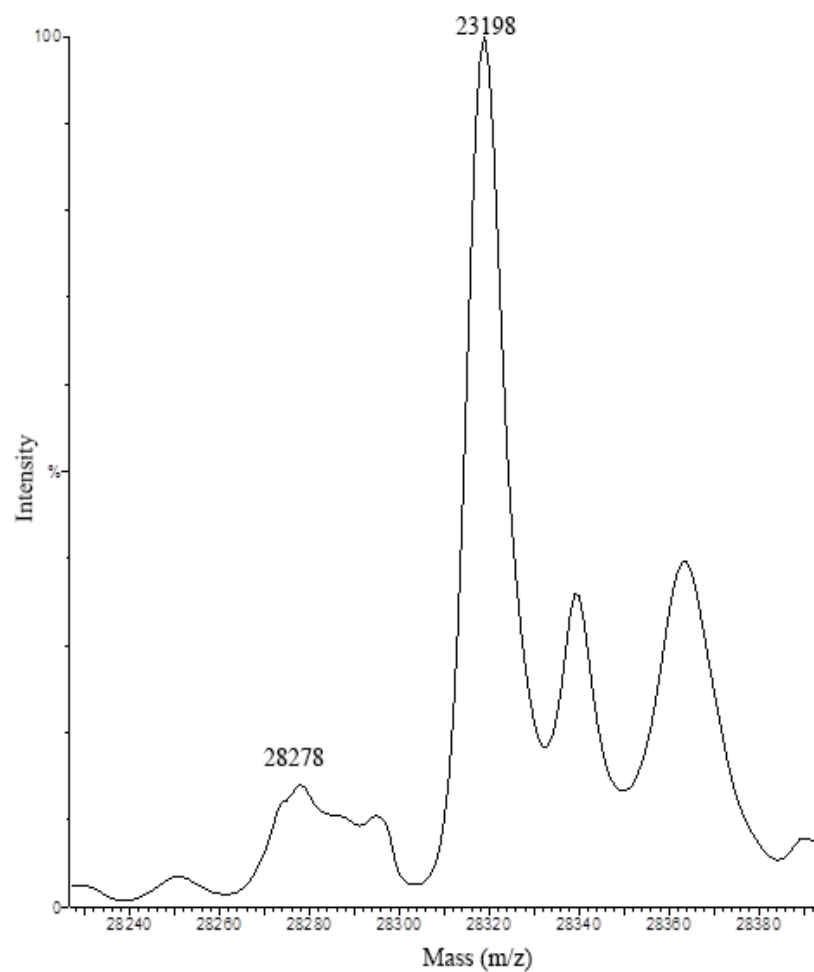


Figure 2.36. Mass spectrum of partially bleached DsRed in 10 mM acetate diluted 1:10 in a 50:50 water:acetonitrile mixture containing 0.1% formic acid.

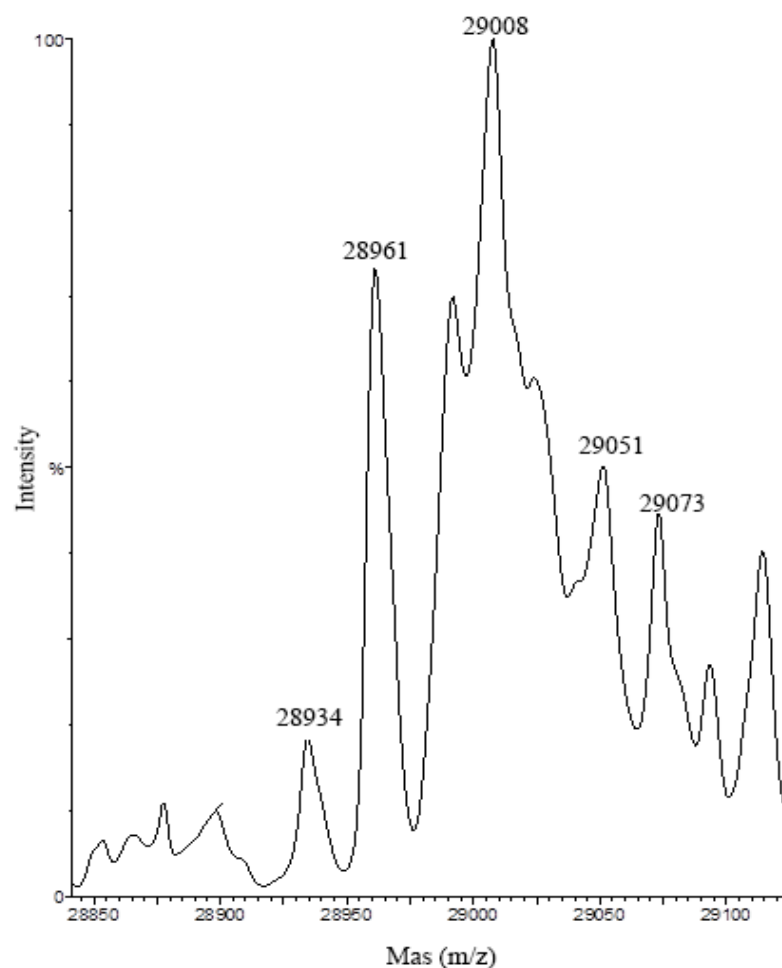


Figure 2.37. Mass spectrum of native KillerRed in 10 mM acetate diluted 1:10 in a 50:50 water:acetonitrile mixture containing 0.1% formic acid. Calculated MW of KillerRed is 28,961 Da which includes -24 Da for cyclization-dehydration-oxidation.

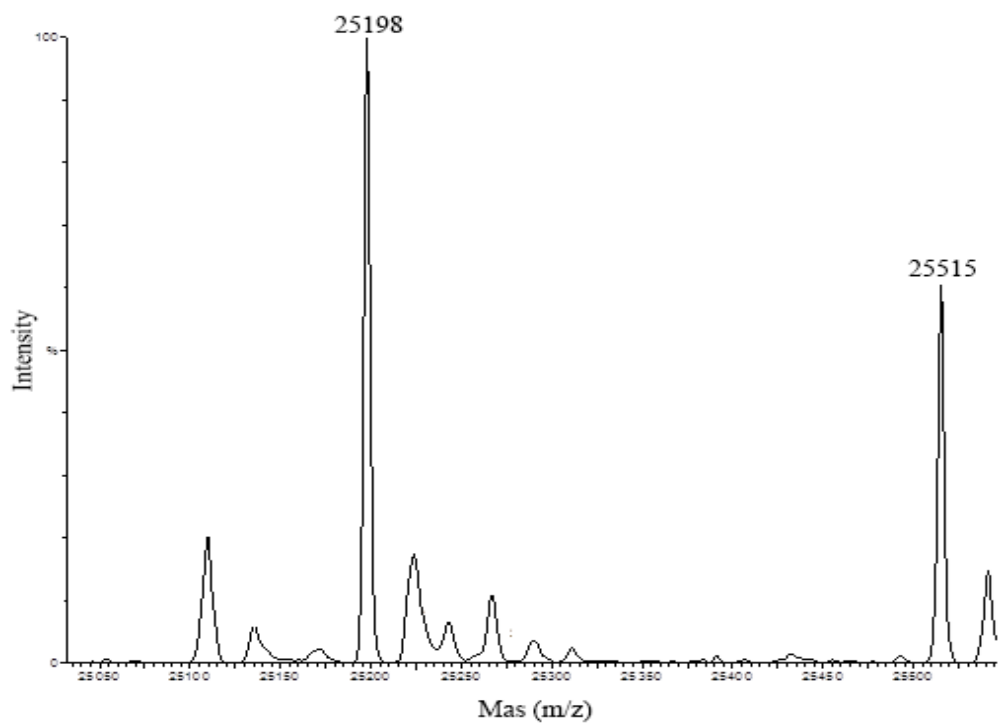


Figure 2.38. Mass spectrum of unbleached mRFP in 10 mM acetate diluted 1:10 in a 50:50 water:acetonitrile mixture containing 0.1% formic acid. Calculated MW of mRFP is 27,980 Da which includes -24 Da for cyclization-dehydration-oxidation.

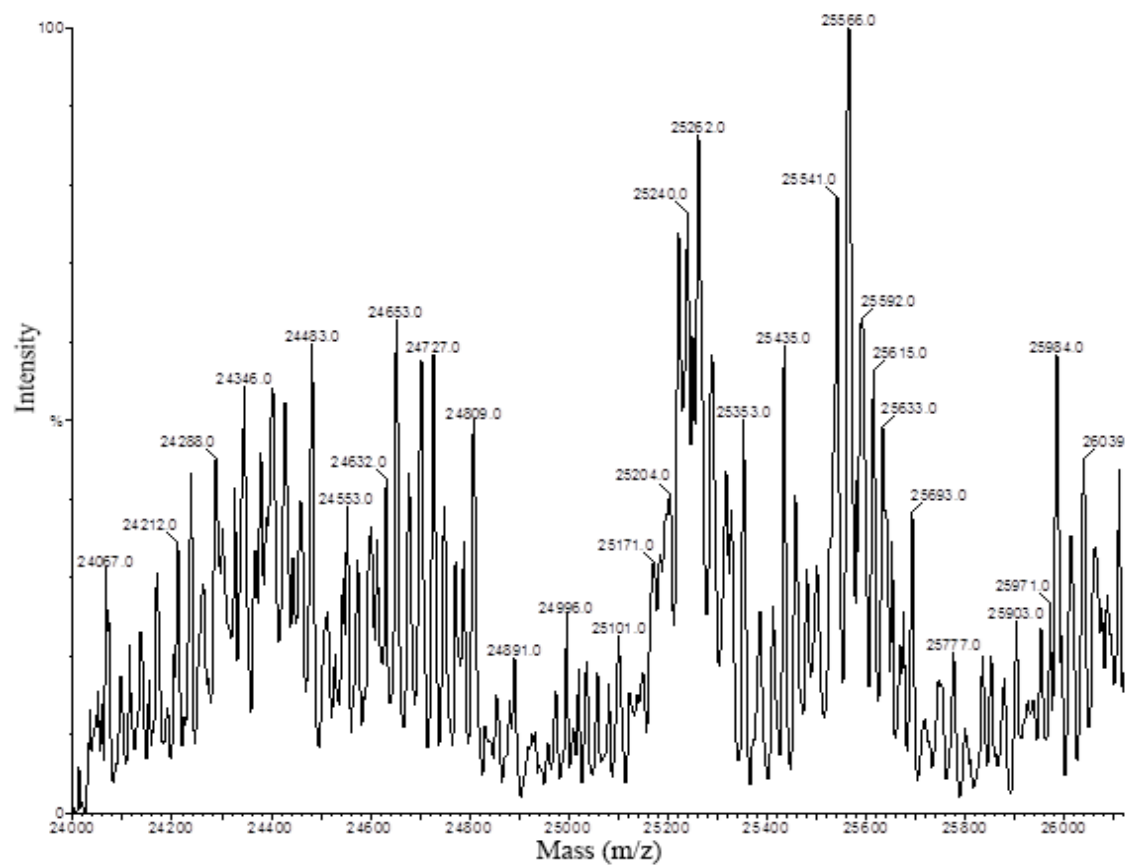


Figure 2.39. Mass spectrum of bleached mRFP in 10 mM acetate diluted 1:10 in a 50:50 water:acetonitrile mixture containing 0.1% formic acid. Calculated MW of mRFP is 27,980 Da which includes -24 Da for cyclization-dehydration-oxidation.

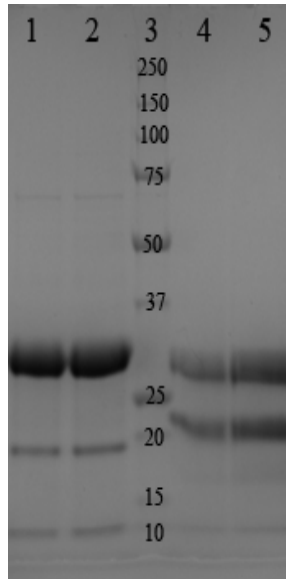


Figure 2.40. SDS PAGE (16%) of mRFP (lanes 1-2), protein ladder (lane 3), and KillerRed (lanes 4-5). Protein ladder contains 250, 150, 100, 75, 50, 37, 25, 20, 15, and 10 kD proteins (top to bottom).

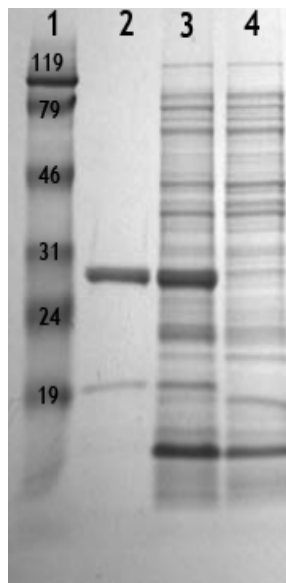


Figure 2.41. SDS PAGE of protein ladder (lane 1), mRFP (10 μ g, lane 2), induced cell lysate (lane 3), and non-induced cell lysate (lane 4). Protein ladder contains 119, 79, 46, 31, 24, and 19 kD proteins (top to bottom).

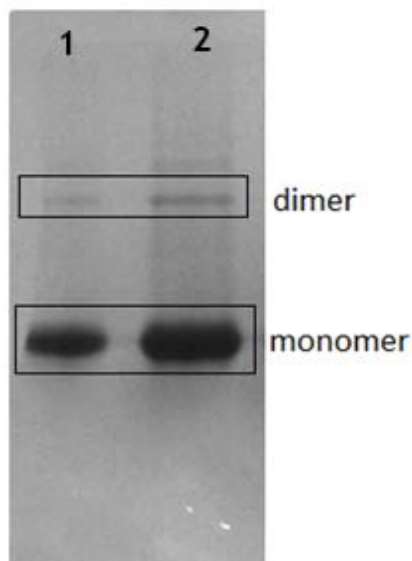


Figure 2.42. Native protein gel (16%) with 15 µg (lane 1) and 45 µg (lane 2) of purified KillerRed. The bottom band represents the monomer of KillerRed and the band above it is attributed to the dimer.

The protein structure of KillerRed was further investigated by peptide mass fingerprinting. Native and bleached KillerRed were digested into their tryptic fragments and subjected to MALDI-MS. The possible cleavage sites of KillerRed following trypsinolysis are illustrated in Figure 2.43. The mass spectral fingerprints of native KillerRed, 50% bleached KillerRed, and 80% bleached KillerRed are shown in Figures 2.44, 2.45, and 2.46 respectively. Most notably, the intensity of the ~2500 Da peak decreased significantly upon irradiation. The peptides of the tryptic digest were also purified by HPLC, the fractions lyophilized, and then subjected to MALDI-MS; however, there were no distinct differences between the fractions of native and bleached samples. Presumably, this is due to the presence of both green and red forms of the chromophore (Figure 2.2); therefore, one form may be unaffected by irradiation (green form) and its fragments will show up in the mass spectra giving false positives.

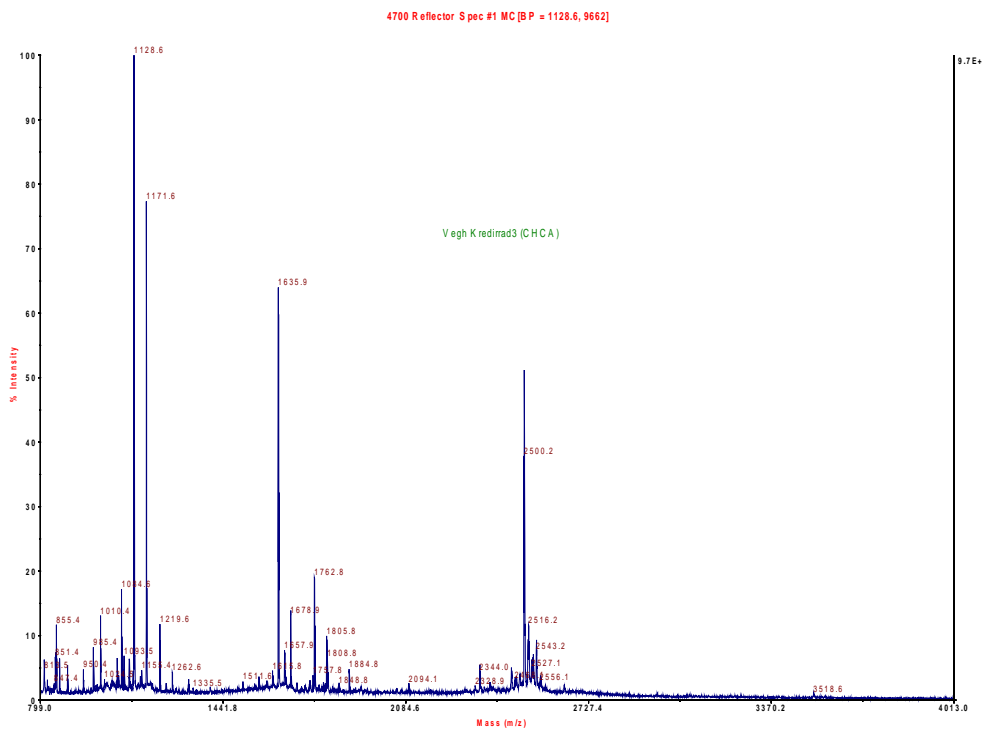


Figure 2.45. Peptide mass fingerprint of bleached KillerRed following trypsin digest. The protein was bleached 50% at 585 nm.

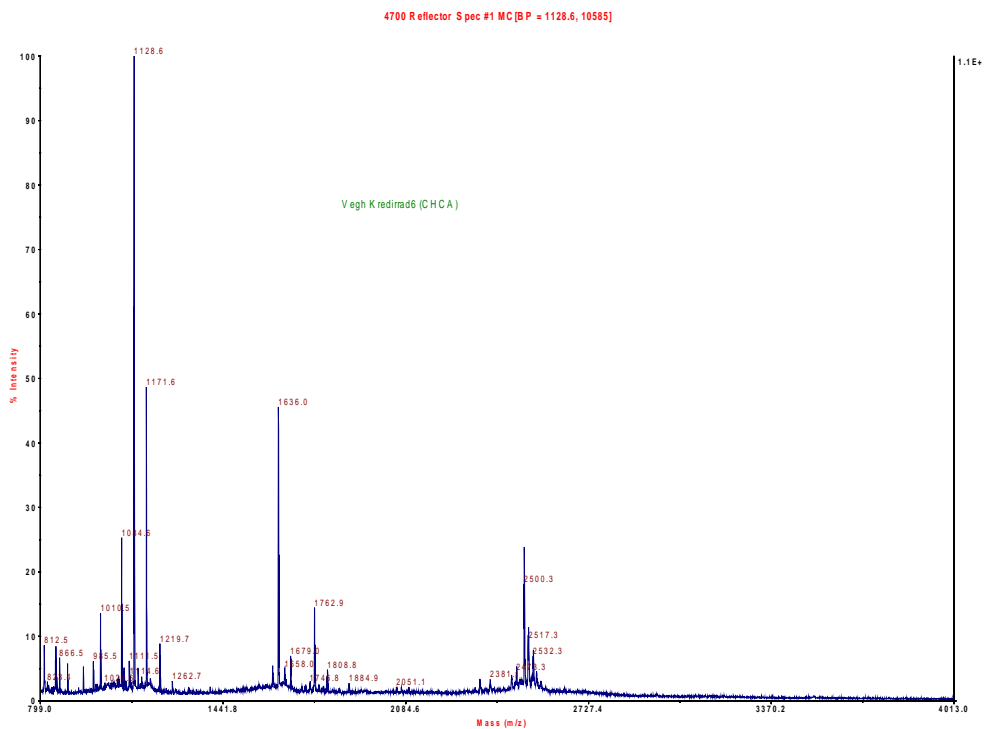


Figure 2.46. Peptide mass fingerprint of bleached KillerRed following trypsin digest. The protein was bleached 80% at 585 nm.

Transient absorption spectroscopy

Now attention will focus on the TA spectroscopy measurements of these proteins to help elucidate the mechanisms of ROS generation and bleaching. The subpicosecond TA spectra were acquired for KillerRed, mRFP, and DsRed. Transients spanned from 800 to 1400 nm as well as one centered at 430 nm (Figures 2.47 and 2.48) for all 3 FPs. Analysis of the transient decays measured at different wavelengths resulted in the same lifetimes of 2.8 ns, 2.2 ns, and 4.5 ns, in KillerRed, mRFP, and DsRed, respectively. All lifetimes were equal to the fluorescence lifetime of the proteins. Therefore, we attribute these transients to the simple decay of the singlet excited state population.

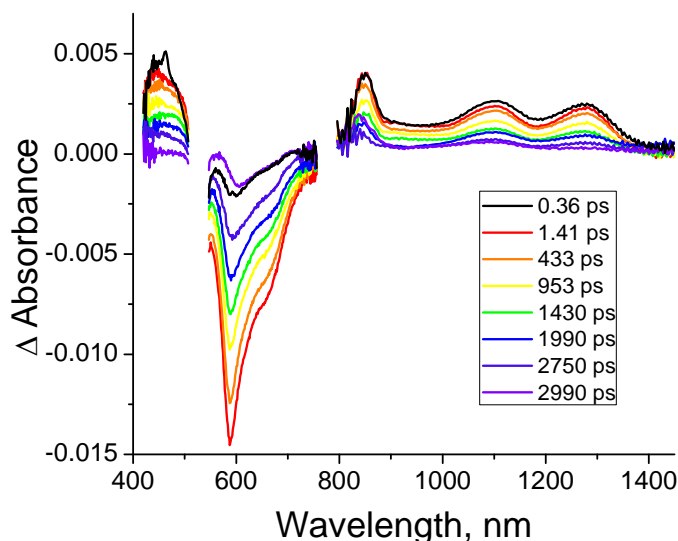


Figure 2.47. Sub-nanosecond TA spectra of KillerRed at pH 7.5 after excitation with 100 fs laser pulse (532 nm, 180 mW/cm²).

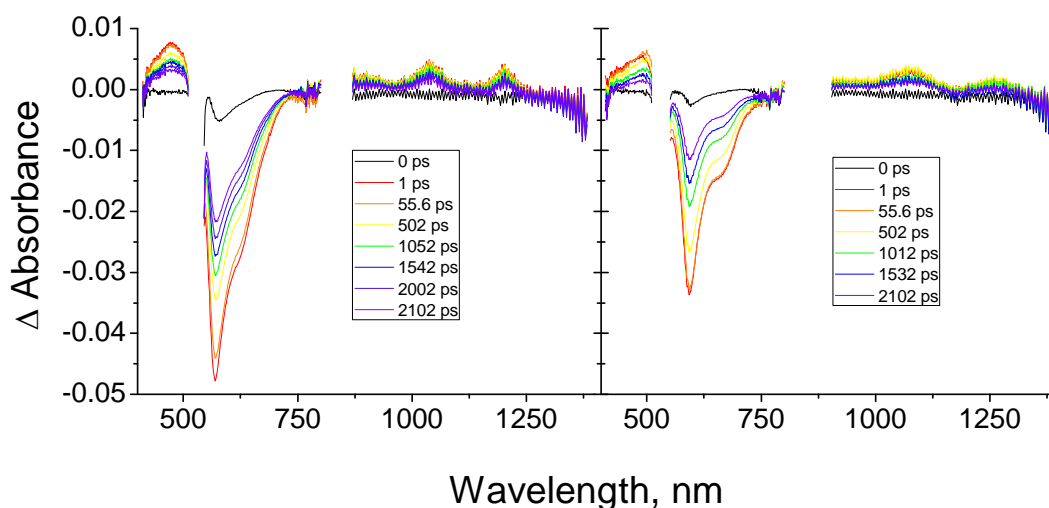


Figure 2.48. Sub-nanosecond TA spectra of mRFP (left) and DsRed (right) at pH 7.5 after excitation with 100 fs laser pulse (532 nm, 180 mW/cm²).

The TA of KillerRed in the μ s-second regime consisted of the ground state bleach at 585 nm concomitant with the appearance of bands with maxima at 430 nm and 735 nm (Figure 2.47). Most of the signal disappeared by 1 ms (Figure 2.49); however, the TA was measured on longer timescales to monitor the slow return of the ground state bleach. The best fit of the data (probed from 2 μ s-1 sec) gave 3 components: a $288 \pm 16 \mu$ s component, a $23 \pm 4 \mu$ s component and a 7.8 ± 0.1 ms component (Figure 2.50). The 288 μ s component, which contributes largely to the main peak of photolysis, has a λ_{\max} of 731 nm with an isosbestic point at 611 nm and its absorption spans beyond 1040 nm where we reach the limit of our detector (Figure 2.50). The 23 μ s component has a λ_{\max} of 623 nm and also includes some absorption at \sim 420 nm (Figure 2.50). The longer component contained very weak absorption at \sim 470 nm. The absorbance decays with their kinetic fits at selected wavelengths are shown in Figure 2.51.

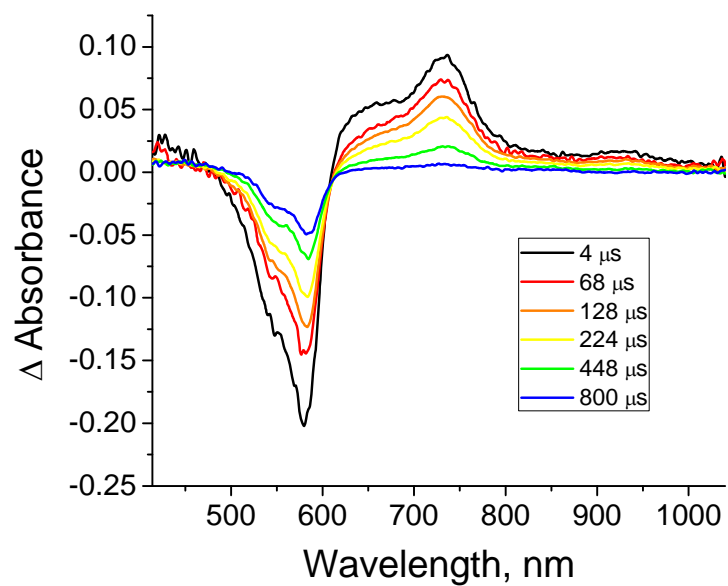


Figure 2.49. TA spectra of KillerRed following 532 nm excitation.

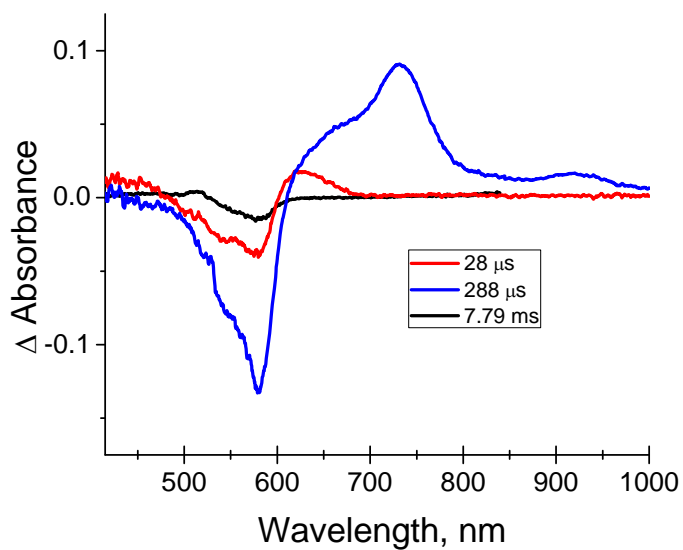


Figure 2.50. The result of the best multiexponential decay fit for the TA data of KillerRed.

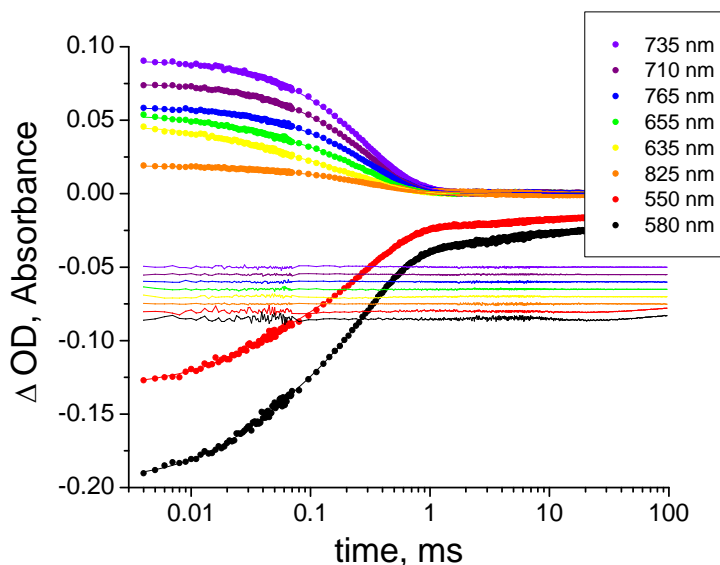


Figure 2.51. Absorbance decays (dots) with kinetic fits (solid lines) for KillerRed at various wavelengths. Residuals displayed at bottom of graph with different vertical offsets. Time constants of the exponential decay components are shown at the top.

Similarly, the μs to ms TA of mRFP consisted of the ground state bleach at 585 nm concomitant with the appearance of bands with maxima at 460 nm and 722 nm (Figure 2.52). Most of the signal was gone by ~ 1.5 ms (Figure 2.52); however, the TA was measured on longer timescales to monitor return of the ground state bleach and disappearance of the weak absorption at ~ 500 nm. Best exponential fit of the data (probed from 2 μs -1 sec) gave three components: a $49 \pm 5 \mu\text{s}$, a $270 \pm 10 \mu\text{s}$, and a 5.9 ± 0.1 ms component (Figure 2.53). The 270 μs component, which contributes largely to the main peak of photolysis, had a λ_{max} of 722 nm with an isosbestic point at 612 nm and absorption that spans beyond 1040 nm (Figure 2.53). The 49 μs component had weak absorption from ~ 420 nm to ~ 510 nm and from 612 nm to beyond 800 nm. The longer 5.9 ms component had absorption centered at ~ 500 nm and ~ 820 nm. The absorbance decays with their kinetic fits at selected wavelengths are shown in Figure 2.54.

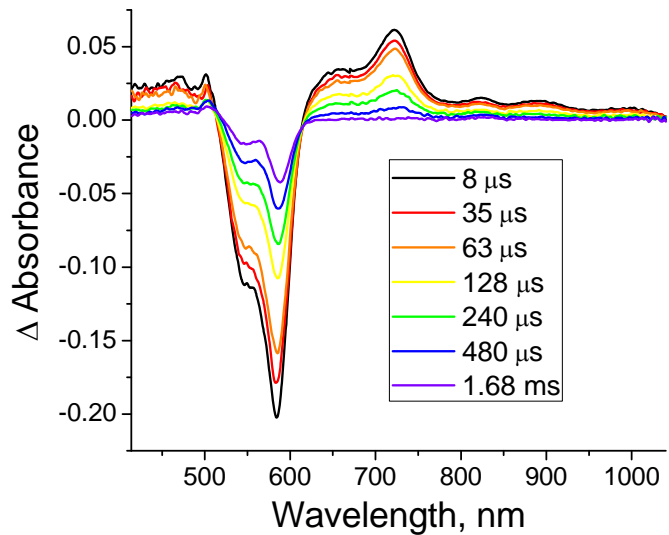


Figure 2.52. TA spectra of mRFP following 532 nm excitation.

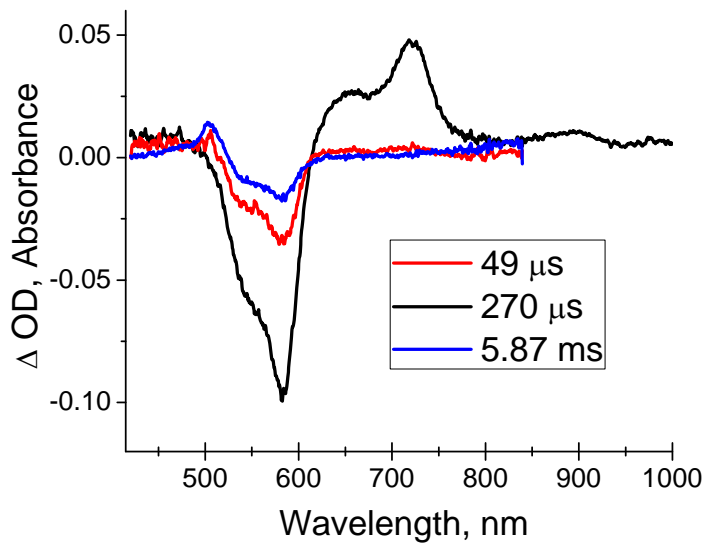


Figure 2.53. The result of the best multiexponential decay fit for the TA data of mRFP.

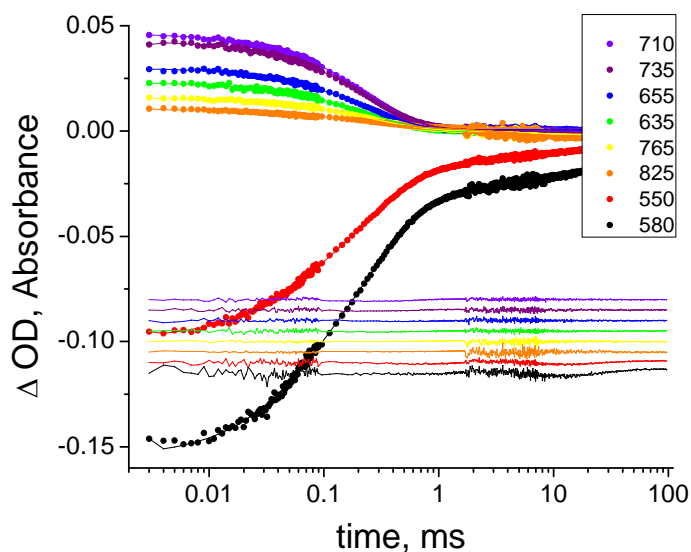


Figure 2.54. Absorbance decays (dots) with kinetic fits (solid lines) for mRFP at various wavelengths. Residuals displayed at bottom of graph with different vertical offsets.

Lastly, the μs to ms TA of DsRed consisted of the ground state bleach at 560 nm concomitant with the appearance of bands with maxima at 430 nm and 745 nm (Figure 2.55). Best fit of the TA data gave three components: a $26 \pm 4 \mu\text{s}$, a $909 \pm 100 \mu\text{s}$, and a longer $>14 \pm 0.1 \text{ ms}$ component (Figure 2.56). The $909 \mu\text{s}$ component had a λ_{max} of 740 nm and also contained weak absorption at $\sim 420 \text{ nm}$. The $26 \mu\text{s}$ component had λ_{max} at 752 nm with negative absorption below this peak. The longer component had very weak absorption spanning the entire region. The last time point (4 seconds) had absorption at 576 nm due to the production of the decarboxylated photoproduct (Figure 2.56) which was previously reported.¹⁴ The absorbance decays with their kinetic fits at selected wavelengths are shown in Figure 2.57.

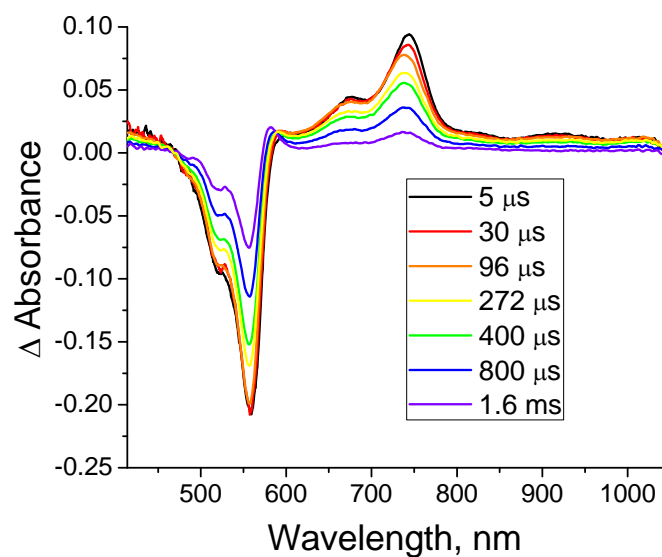


Figure 2.55. TA spectra of DsRed following 532 nm excitation. The sample was probed for 4 seconds.

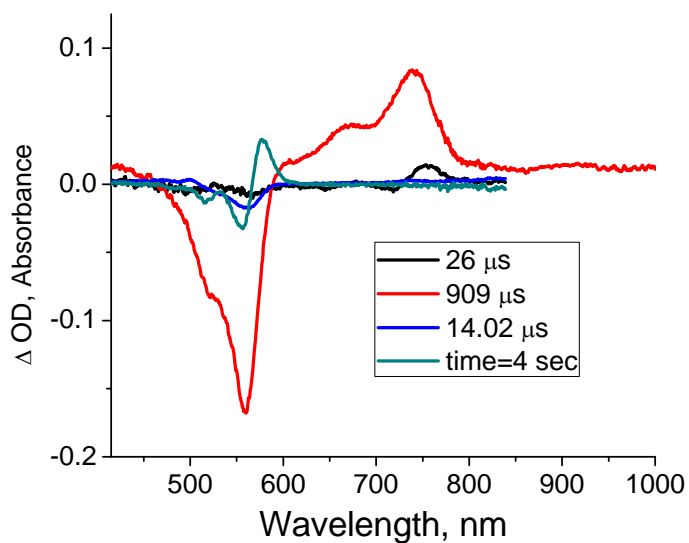


Figure 2.56. The result of the best multiexponential decay fit for the TA data of DsRed. The time point 4 sec is shown to demonstrate the production of decarboxylated photoproduct.

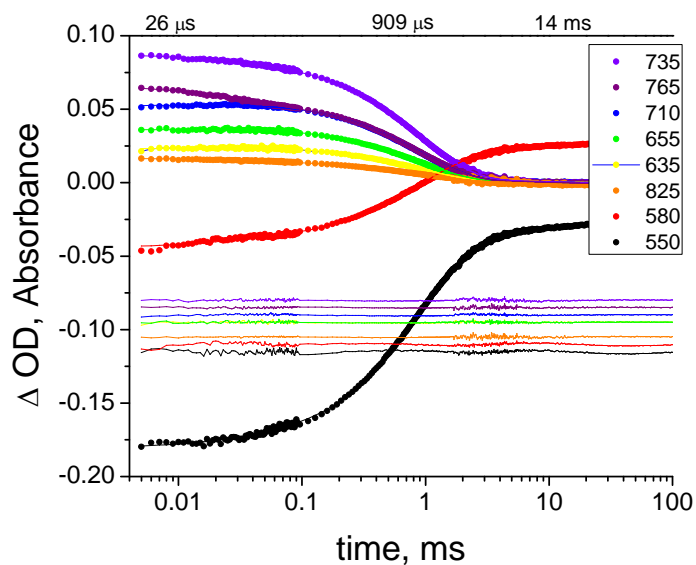


Figure 2.57. Absorbance decays (dots) with kinetic fits (solid lines) for DsRed at various wavelengths. Residuals displayed at bottom of graph with different vertical offsets. Time constants of the exponential decay components are shown at the top.

To help elucidate the identity of the main transient feature in each of the proteins, the TA was acquired under several conditions. First, the TA was acquired for samples in both fully aerobic and anaerobic conditions. The lifetimes of the transient signal decreased in the presence of oxygen for KillerRed and mRFP while DsRed remained unchanged (Figure 2.58). A primary isotope effect was observed for all three proteins (Figure 2.58).

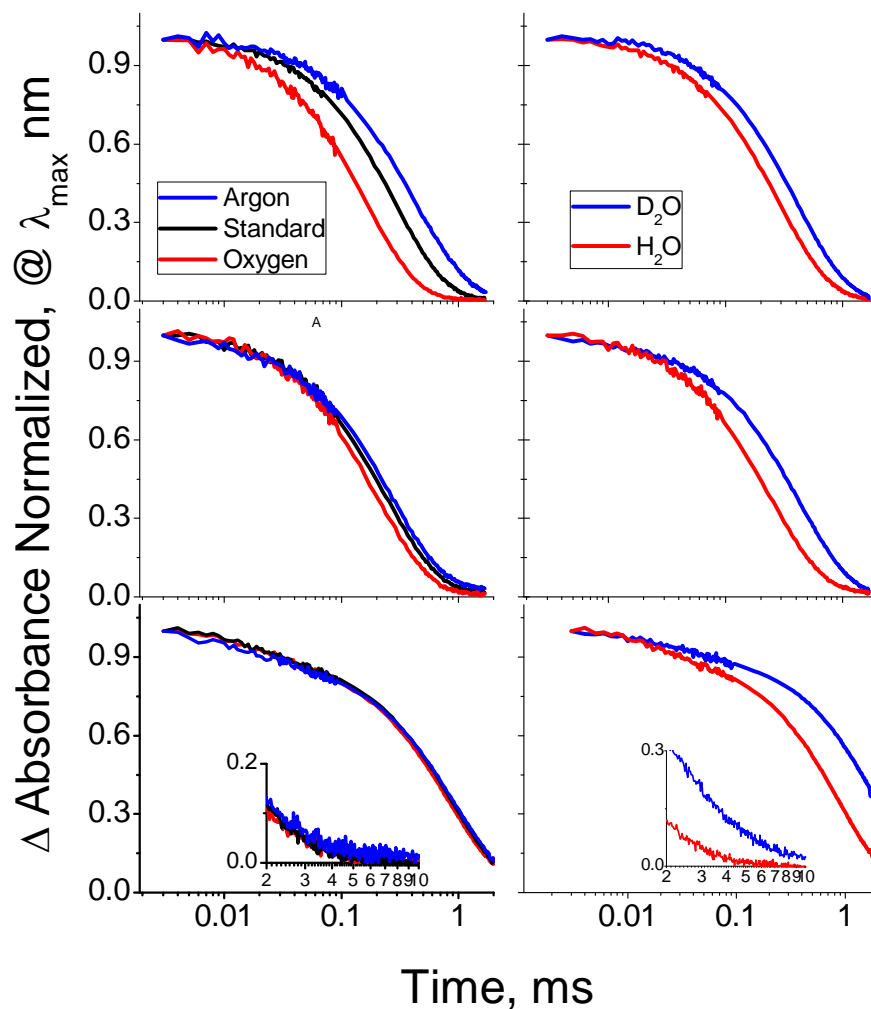


Figure 2.58. Decay of the transient signal at 731 nm for KillerRed for an oxygenated sample (top left, red line), a standard sample (top left, black line), an anaerobic sample (top left, blue line), and a sample in D₂O (top right). Decay of the transient signal at 722 nm for mRFP for an oxygenated sample (middle left, red line), a standard sample (middle left, black line), an anaerobic sample (middle left, blue line), and a sample in D₂O (middle right, blue line). Decay of the transient signal at 745 nm for DsRed for an oxygenated sample (bottom left, red line), a standard sample (bottom left, black line), an anaerobic sample (bottom left, blue line), and a sample in D₂O (bottom right, blue line).

The TA of KillerRed, mRFP and DsRed were measured in the presence of several oxidants and reductants (cytochrome C, β -mercaptoethanol, NAD⁺, potassium

ferricyanide, and flavin mononucleotide) to determine what effect, if any, they may have. In all three cases, the kinetics of the TA were unaffected. The oxidants and reductants are likely too large to penetrate the β -barrel and reach the chromophore; therefore, H_2O_2 was used since it is a smaller molecule and can act as both an oxidant and reductant. Surprisingly it had a profound effect on the lifetime of the transient signal in KillerRed (Figure 2.59). The lifetime of the transient signal in mRFP was also affected, but to a lesser extent while the lifetime of the transient signal in DsRed remained mostly unchanged (Figure 2.59). The same levels of H_2O_2 had little to no effect on the ground state absorption spectrum for all three proteins (Figures 2.28, 2.60, and 2.61).

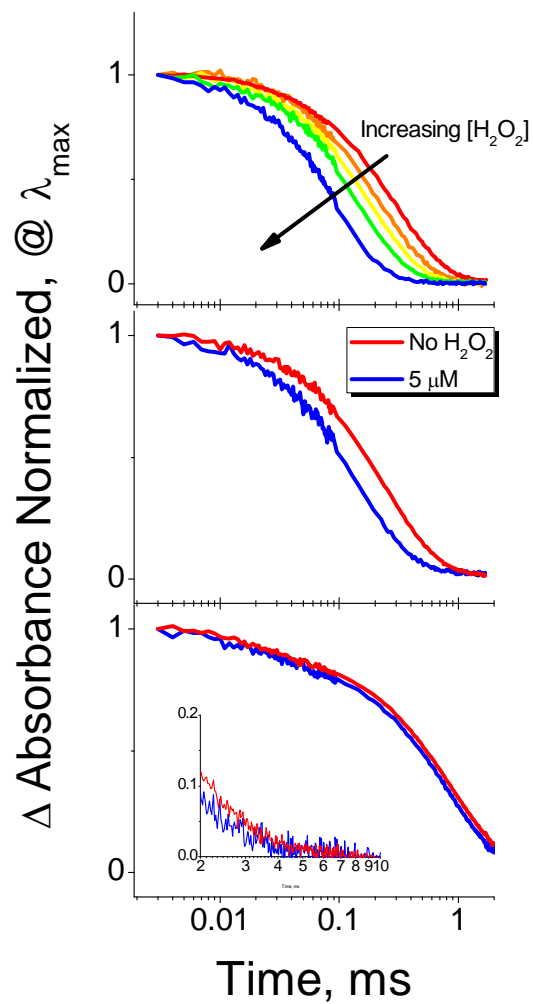


Figure 2.59. Kinetics of the transient absorption signal at 731 nm for KillerRed (top), at 722 nm for mRFP (middle), and at 745 nm for DsRed in the absence and presence of H_2O_2 .

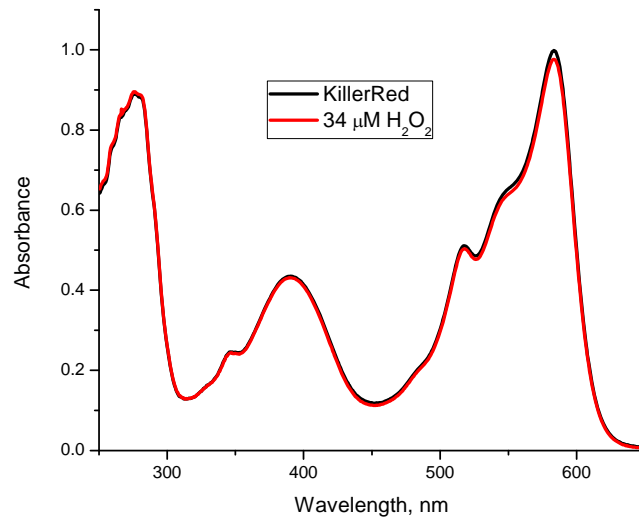


Figure 2.60. Ground state absorption spectra of KillerRed before and after addition of 34 μM H_2O_2 .

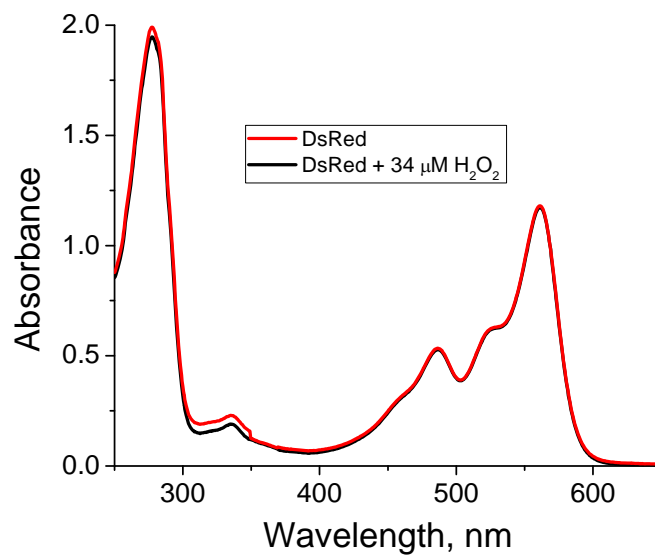


Figure 2.61. Ground state absorption spectra of DsRed before and after addition of 34 μM H_2O_2 .

Discussion

Using time-resolved phosphorescence measurements, it was demonstrated that no substantial quantities of $^1\text{O}_2$ could be detected following excitation of KillerRed. Thus, these data cannot confirm the involvement of the type II mechanism in KillerRed photodynamics. These results are consistent with the observation of Serebrovskaya *et al.*,⁶⁹ who observed lower phototoxicity of KillerRed chemical conjugate in D_2O compared to H_2O . The opposite trend was to be expected if a Type II, $^1\text{O}_2$ -mediated mechanism was playing a significant role in the phototoxicity of KillerRed.

Comparison of KillerRed and mRFP using *in vitro* CALI studies, whereby each protein was fused to β -galactosidase, indicates that mRFP is also phototoxic; but to a lesser extent than KillerRed. These results were confirmed using the radical trap TEMPO-9-ac. Irradiation of mRFP in the presence of this probe resulted in a large increase in TEMPO-9-ac fluorescence indicating radical production. Through previously published experiments, it has already been confirmed that DsRed is non-phototoxic.²²

Radical formation with KillerRed and mRFP, as monitored by TEMPO-9-ac trapping, is expected, since the electron photoejection and radical cation formation with the chromophore was observed previously even for non-toxic GFP synthetic chromophores in solutions,^{92,93} and in the gas phase,⁹⁴ as well as for several fluorescent proteins.⁹⁵ It was also proposed recently⁶⁷ that the direct long-range electron transfer, a mechanism involving the long hydrogen bond network through the channel, proceeds *via* a light-induced photoreduction of the chromophore followed by superoxide generation. A very strong dependence of the TEMPO-9-ac fluorescence adduct emission on the partial pressure of molecular oxygen (Figure 2.11) demonstrates an involvement of

the latter in radical reactions. O_2 commonly serves as a primary acceptor for electrons, forming O_2^- , which can react further to form a plethora of products, such as $\bullet OH$ and H_2O_2 . Therefore, the strong dependence of the TEMPO-9-ac fluorescence signal on oxygen pressure is not surprising.

The ESI-MS for the non-phototoxic fluorescent protein DsRed in the native form had a peak consistent with the molecular weight. In the spectra of photobleached DsRed, a peak appeared which was close the expected mass for decarboxylation, the work of which has been previously published.¹⁴ In the ESI-MS of KillerRed, a peak consistent with the molecular weight (28,961 Da) was observed; however, other higher and lower molecular weight species were also present. The PAGE of KillerRed indicated that the protein was in fact pure for ESI-MS analysis (Figure 2.42). The mass spectra of native mRFP had peaks at 25,196 Da and 25,515 Da (Figure 2.38) which are not consistent with the expected mass of 27,980 Da. The SDS-PAGE of mRFP contained multiple band which have been previously assigned to the partial hydrolysis of the acylamine chain;⁵⁶ however, the molecular weights observed were still far off from those expected for acylamine chain hydrolysis. It may also be possible that mRFP contains another site easily hydrolyzable under the given conditions (50:50 water:acetonitrile mixture containing 1% formic acid). Presumably, this may be the 6xHN histag and polylinker which has a molecular weight close to the difference between what is observed (25,196 Da/25,515 Da) and what is expected (27,980 Da). The mass spectra of bleached mRFP and bleached KillerRed were very noisy and the peaks were not well resolved. Because both of these proteins are phototoxic leading to generation of ROS, this can lead to oxidation of amino acid residue side chains, cleavage of peptide bonds, and formation of

covalent protein-protein cross-linked derivatives.⁹¹ Therefore, the poor quality of the spectra obtained after photobleaching is attributed to these factors.

MALDI-MS following trypsinolysis of KillerRed was used to elucidate the mechanism of bleaching. This method was previously applied to GFP to study chromophore maturation.^{7,96} The most notable difference in the peptide mass fingerprint of KillerRed before and after irradiation was the decrease in intensity of the ~2,500 Da peak. This peak may correspond either to residues 61-82 (residues 37-58 without polylinker and 6HN tag) or 161-182 (residues 137-158 without polylinker and 6HN tag); however, trypsin should cleave after lysine in residues 61-82 forming fragments 5 and 6 (Figure 2.43); therefore, this peak is most likely residues 161-182. From the crystal structure (Figure 2.62), it is shown that residues 161-182 are close to the chromophore and the water channel of KillerRed. They are also along the dimer interface where the electron density maps of bleached KillerRed indicate degradation of chain 161-182 in monomer B (Figure 2.63). The degradation of only one chain is expected since the dimer of KillerRed is presumably made up of a green and red monomer, and therefore, only the red form would be active.⁶⁵ In the crystal structure of bleached KillerRed, the chromophore also underwent degradation,^{64,65} however, from the mass spectra obtained herein, the chromophoric peptide was not observed.

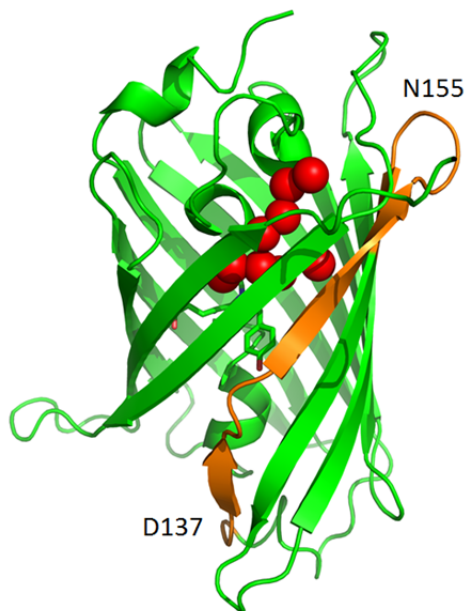


Figure 2.62. Representation of the β -barrel of KillerRed (PDB 3GL3) with the long-filled water channel in red and residues 137-158 highlighted in orange. Drawn using the PyMOL Molecular Graphics System, Version 1.2r3pre, Schrödinger, LLC.

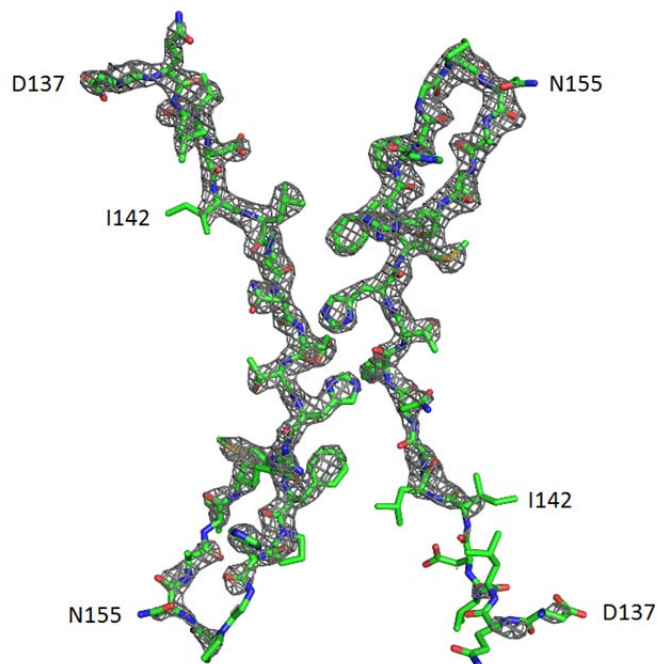


Figure 2.63. Electron density map of photobleached KillerRed (PDB 3GL4, $2mF_o-DF_c$ contoured at 2σ) showing residues 137-158 of monomer A (left) and monomer B (right). Drawn using the PyMOL Molecular Graphics System, Version 1.2r3pre, Schrödinger, LLC.

TA spectroscopy was used to study the dark states of RFPs in order to elucidate the mechanisms of bleaching. Interestingly, all three proteins showed a similar transient feature peaking close to 740 nm. When the axes are converted to energy, this feature is almost an exact mirror image of the ground state bleach. Since the triplet lifetime of KillerRed is no more than 40 μ s (Figure 2.6) and is one order of magnitude shorter than the transient centered at 721 nm, it is excluded in the identification of the main transient feature. Due to the decarboxylation mechanism proposed for DsRed^{13,16} and the production of radicals in KillerRed and mRFP, the most plausible identity of the transient would be radical dianion. In the phototoxic fluorescent proteins, KillerRed and mRFP, the dianion could then donate an electron to O₂ to generate superoxide. In the case of DsRed, presumably decarboxylation of E215 (E222 in wtGFP) leads to an alkyl radical^{13,16} which can then be quenched by radical dianion. However, one cannot ignore other possibilities such as a charge transfer complex or electron ejection leading to radical chromophore and solvated electrons.

As established in this work, the phototoxicity and radical production increases in the order: DsRed < mRFP < KillerRed. There is a direct correlation with these results and the quenching experiments where the main transient feature was quenched with O₂ and H₂O₂. For example, the lifetime of the transient signal in the most phototoxic fluorescent protein KillerRed decreased significantly in the presence of either H₂O₂ or O₂, while the lifetime of the transient in DsRed remains mostly unaffected. This phenomenon is likely attributed to the unique structure of the KillerRed interior.^{64,65} KillerRed, unlike most other fluorescent proteins, has a unique long water-filled channel (Figure 2.62). It is hypothesized that this channel allows the reactive oxygen species to escape and reach

their target, thereby contributing to KillerRed's phototoxicity. It is quite interesting that an agent as small as O_2 is unable to penetrate the β -barrel of DsRed; however, it is not that surprising since previous researchers had to use guanadinium HCl to add flexibility to a GFP mutant to detect singlet oxygen production.¹⁷

Conclusions

In summary, using fluorescent probes and EPR (Figures 2.21 and 2.22), we conclude that irradiation of KillerRed and mRFP results in the production of radicals supporting a type I photosensitization mechanism. The phototoxicity of mRFP was investigated using *in vitro* CALI studies and these results demonstrated that mRFP was phototoxic but to a lesser extent than KillerRed. The phototoxicity of KillerRed and mRFP as a CALI agent is likely due to protein cross-linking through radical reactions. It has been previously demonstrated that EGFP likely works in this same manner;⁴² however, the authors stated that 1O_2 inflicted the damage on the fused proteins and erroneously claimed this using the scavenger sodium azide, which is also known for quenching $\cdot OH$.⁹⁷ While it is possible that small amounts of 1O_2 are still produced by KillerRed, it is unlikely to be responsible for much of the phototoxicity, and thus we conclude that most of the phototoxicity stems from a type I photosensitization mechanism. Further, we find that KillerRed, mRFP and EGFP, feature catalase-like activity, as we observe significant consumption of H_2O_2 . Therefore, KillerRed demonstrates a unique Janus-type feature, acting as both ROS generator and antioxidant.

Through crystallographic evidence, it was previously shown that KillerRed bleaching is accompanied by degradation of the chromophore.^{64,65} The MS results obtained herein indicate degradation of residues 137-158, which are close to the

chromophore and at the dimer interface (Figure 2.61). From the bleached crystal structure of KillerRed, the electron density map supports the degradation of the residues 137-158. These residues are close to the chromophore, the site where ROS would first form; therefore, it is not surprising that irradiation of KillerRed would lead to degradation of this chain.

Bulina *et al.* suggested that N145 and A161 were indispensable for the phototoxicity of KillerRed. By mutating these two positions back to the wild-type residues found in anm2CP, it was demonstrated that these sites have a large effect on the *E/Z* isomerization of the chromophore (Figure 2.33) as well as the chromophore maturation. These effects were further supported by crystallographic evidence^{64,65} which demonstrated just how these residues participate in hydrogen bonding with the chromophore and therefore favor one state over the other.

The TA spectra of KillerRed, mRFP, and DsRed all contained a similar transient centered close to 740 nm. Quenching studies with O₂ and H₂O₂ demonstrated that the accessibility of the chromophore could play an important role in the phototoxicity of RFPs. In the phototoxic fluorescent protein KillerRed, small molecules such as O₂ and H₂O₂ were able to penetrate the β -barrel and drastically affect the lifetime of the transient, whereas in the non-phototoxic fluorescent protein DsRed, the transient was mostly unaffected. This evidence is further supported by the unique structure of the KillerRed interior which features a long water-filled channel extending from the chromophore to the outside environment.

CHAPTER 3

HIDDEN PHOTOINDUCED PROTON TRANSFER IN THE BLUE FLUORESCENT PROTEIN MKALAMA1

Introduction

The Green Fluorescent Protein (GFP), widely known due to its ubiquitous use as an *in vivo* fluorescent marker, is an 11-stranded β -barrel with an α -helix running through the center. The chromophore is midway of the α -helix and is formed by the three amino acids S65, Y66, and G67 through an autocatalytic post-translational cyclization only requiring molecular oxygen.¹²

Wild-type GFP (wtGFP) has 2 main absorption maxima at 398 nm (band A) and 478 nm (band B) corresponding to the chromophore and its conjugate base, respectively. Excitation of band A simultaneously yields a weak 460 nm and a strong 508 nm emission. The strong fluorescence at 508 nm occurs through an excited-state proton transfer (ESPT) mechanism, where the chromophore becomes deprotonated at the Y66 phenol group in the excited state resulting in a \sim 100 nm emission shift.¹² It has been established that in wtGFP, the proton is translocated via the major, well-defined Chromophore-Water22-S205-E222 proton wire.⁹⁸ Recently, Agmon proposed an existence of the less efficient alternative proton wire that involves a nearby T203 residue.⁹⁹ It was proposed that excitation of the chromophore induces a conformational change in T203 expelling the proton to the solvent. Then, in the ground state, the chromophore can be reprotonated by

E222 which in turn can acquire a proton from the outside environment via the E5 entry pathway located near the N-terminal on the GFP surface.⁹⁹

Mutations to wtGFP have resulted in a plethora of fluorescent proteins with various photophysical and photochemical properties. Mutating the Y66 residue of wtGFP to histidine and tryptophan gives the blue (BFP) and cyan fluorescent proteins (CFP) respectively.⁸ Until recently, BFPs reported in literature were only based off the histidine and phenylalanine chromophores, as well as on the unique non-matured red chromophore in mTagBFP.¹⁰⁰ Then, in 2007, the synthesis and properties of two BFPs based on the Y66 chromophore were reported.^{29,34} Both T203V/S205V³⁴ (ex/em 390/459 nm, fluorescent quantum yield $\phi = 0.29$) and mKalama1²⁹ (ex/em 385/456 nm, $\phi = 0.45$) are the variants of the wtGFP in which the main (via S205) and the alternative (via T203) proton wires are blocked. Therefore, the bright single-band fluorescence of these proteins belongs to the neutral chromophore in the most stable Z configuration (Z^N).⁹⁸

Many studies have been conducted to investigate the dynamics in FPs. However, measurements in the microsecond to second time domain are rarely reported and mostly involve the Fluorescence Correlation Spectroscopy (FCS),¹⁰¹⁻¹⁰⁵ single-wavelength phosphorescence^{19,20} and single-wavelength TA^{106,107} measurements. The processes with relaxation times in this time range have been ascribed to protonation and/or conformational dynamics of the GFP chromophore.¹⁰² However, no detailed spectral information about the nature of the transients in μ s-s regime is available and the mechanisms still remain elusive. In this work we undertook the investigation of photochemical and photophysical properties of the BFP mKalama1 and unveiled the broad band TA spectroscopy measurements from picoseconds to seconds.

Materials and Methods

Protein expression and purification

The gene encoding mKalama1 was purchased from AddGene (Cambridge, MA). The gene is inserted between the *Xho*I and *Eco*RI restrictions sites in pBAD-His B and contains an N-terminal hexahistidine tag. The plasmid was transformed into *E. coli* DH5 α Pro. A 5 mL culture was inoculated into 1 L of LB (pH 7) containing 50 μ g/mL of ampicillin, grown to an OD600 of 0.5 at 37 °C (2-3 h), and protein expression was induced with 0.2% arabinose. We overexpressed mKalama1 to 20% of total cell protein and purified the protein via Ni²⁺-NTA-immobilized metal affinity chromatography (IMAC). All measurements were performed in PBS (50 mM sodium phosphate, 250 mM NaCl, pH 7.5) unless otherwise stated.

Transient absorption spectroscopy measurements (μ s-s time domain)

TA measurements were performed on the same set-up as mentioned in the Materials and Methods of Chapter 2. Photolysis of the ground-state mKalama1 was achieved with single-flash laser excitation at 355 nm (180 mJ/cm², 4 ns per pulse). The time-wavelength matrix of the TA changes in the 1 μ s – 1 min time window following the photolysis was decomposed into a multiexponential decay function (Equation 3.1) using a global fit algorithm:

$$\Delta A(t, \lambda) = \sum_i \varepsilon_i(\lambda) \exp(-t/\tau_i) \quad (\text{Eq. 3.1})$$

where $\Delta A(t, \lambda)$ is the optical absorption change at time t ($t = 0$ at the instance of laser flash) and at wavelength λ , and $\varepsilon_i(\lambda)$ and τ_i are the characteristic spectrum and time

constant for the i -th exponential decay component, respectively. Measurements and data processing were performed by Dr. Dima Bloch and Russell Vegh.

Transient absorption spectroscopy measurements (ps-ns time domain)

Femtosecond TA measurements were performed using the same set-up as mentioned in the materials and methods of chapter 2, except the pump wavelength was 375 nm. The intensity of the pump was 145 mW/cm². The protein solutions had an OD₃₉₀ of ~0.5 in 2 mm path-length cuvettes, and were stirred continually throughout the data acquisition. Measurements were performed in Dr. Joseph Perry's lab (GA Tech, Atlanta, NC).

Time-correlated single photon counting measurements.

Time-resolved fluorescence was acquired using the Time-Correlated Single Photon Counting method (TCSPC). Picosecond pulsed diode lasers were used to excite the samples. Excitation of both the neutral and anionic chromophore was achieved using 372 nm and 476 nm diodes respectively. Details of the set-up and data processing can be found in the Materials and Methods of Chapter 2.

Isotopic measurements

For the kinetic measurements in D₂O, the concentrated protein samples were diluted in 99.9% D₂O-based PBS buffer (pD 7.5); the final H₂O concentration in the samples did not exceed 2%. pD was adjusted with a KOD or DCl, taking into account the typical pH correction for the pH glass electrode: $pD = pH^{app}(D_2O) - 0.4$.⁷⁷ The samples were incubated for 14 h in the D₂O medium before measurements.

Aerobic and anaerobic measurements

Anaerobic samples were prepared using a gas/vacuum line of local design. A 4 x 10 x 30 mm fluorescence quartz cell was sealed to a Kimble-Kontes high-vacuum stopcock, which had a vacuum O-ring connection to the vacuum line. As a typical degassing procedure, 20 cycles of exchanging vacuum (10^{-3} bar) and pure Ar were followed by shaking the cell filled with Ar for 15 min on an orbital shaker; then the procedure was repeated 2 more times. 99.99% Ar was additionally purified using the Agilent Technologies BOT-2 and IOT oxygen scrubbers. Aerobic samples were bubbled with oxygen for 10 minutes.

Results

First, the spectral and kinetic behavior of mKalamal at neutral pH is described. The absorption and emission of mKalamal have almost structureless peaks with maxima at 390 and 455 nm (Figure 3.1a), respectively, and are close to the reported values.²⁹ The fluorescence decay at pH 7.5 was fit with a bi-exponential decay with lifetimes of 0.8 ns and 1.9 ns and an amplitude ratio of 0.25 (Figure 3.2). At pH 11.25 ($\lambda_{\text{ex}} = 476$ nm), the data was fit with a bi-exponential decay and had lifetimes of 78.0 ns and 3.9 ns with an amplitude ratio of 0.005; therefore, the 78 ns component is negligible (Figure 3.3). If mKalamal exhibited ESPT, one would expect to see a rise time as well as an increase in the decay time since the lifetime of the anion is longer (3.9 ns) than that of the neutral (0.8 ns and 1.9 ns). Therefore, at pH 7.5, the absence of both a rise time component at the red edge of the spectrum and an increase of the decay time¹⁰⁸ (Figure 3.3) indicates there is no anionic emission and hence no ESPT.

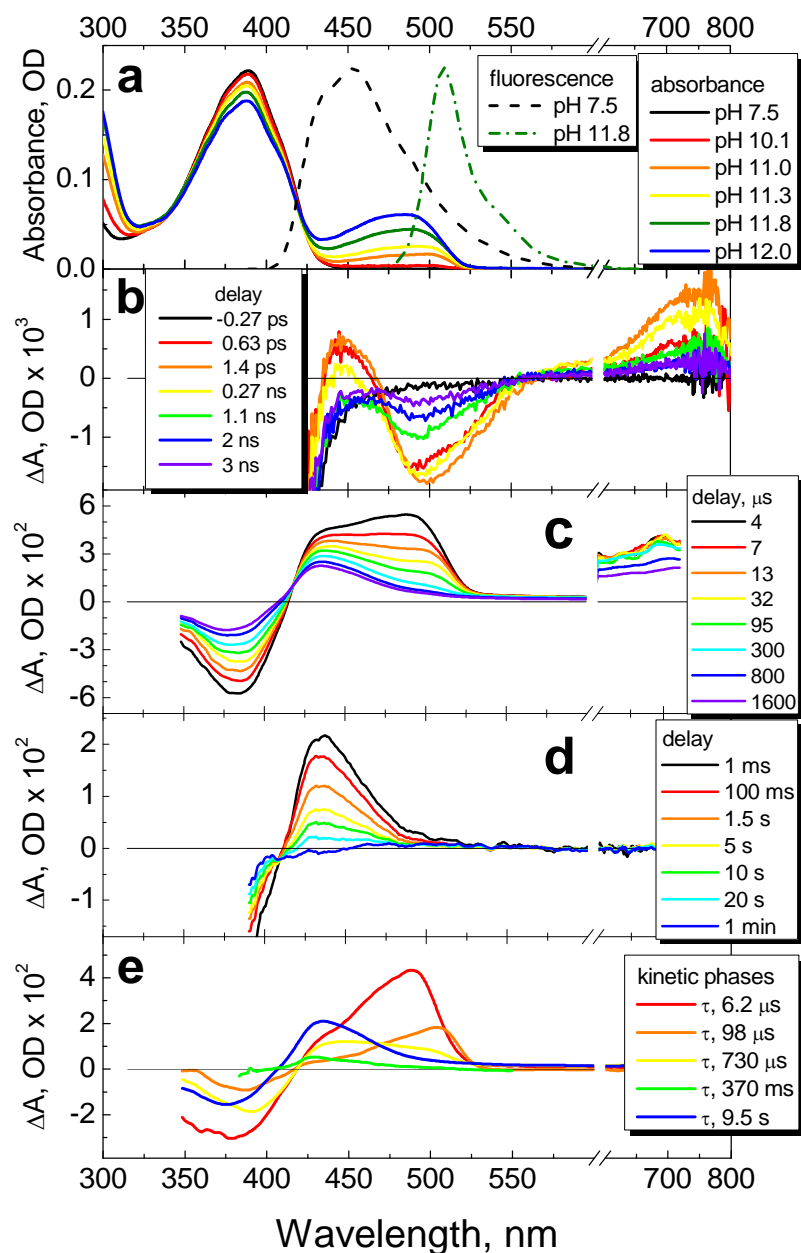


Figure 3.1. Optical properties of mKalama1. (a) Absorption and emission spectra of mKalama1 at various pH. Buffer: CCPBS (20 mM CAPS, 20 mM CABS, 20 mM KPi, 200 mM NaCl); pH adjusted with KOH. (b) TA spectra of mKalama1 at pH 7.5 after excitation with 100 fs 355 nm laser pulse (145 mw/cm^2). (c) TA spectra of mKalama1 at pH 7.5 after excitation with 4 ns 355 nm laser pulse. The 600-750 nm part was magnified by the factor of 10 for better visualization. (d) Same as (c), but monitored in 1 ms - 1 min time window. (e) The results of the best multiexponential decay fit (Eq. 1) of the data from graph (c). The spectrum at $t = 0$ was calculated by the extrapolation of the fit. Buffer: PBS (pH 7.5). $\epsilon(\lambda)$: normalized to 1 mg/mL protein.

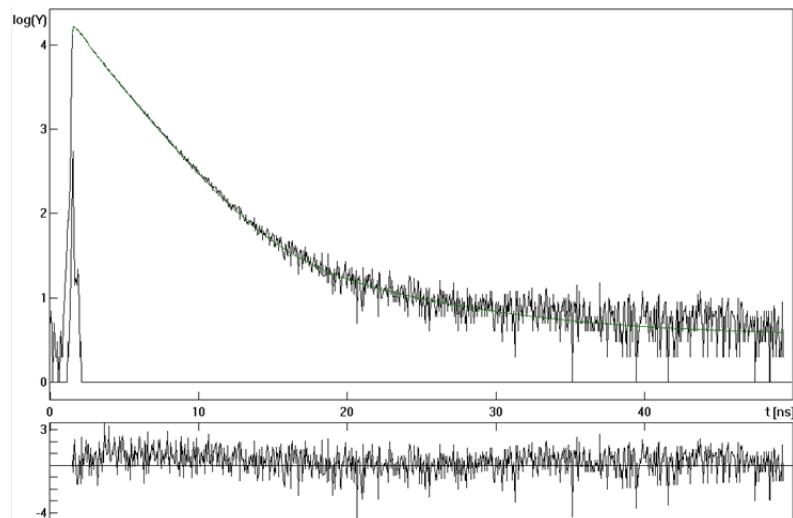


Figure 3.2. Fluorescence decay of mKalama1 at 460 nm excited with a 372 nm pulsed diode at pH 7.5 (upper panel) and multiexponential fit residuals (lower panel).

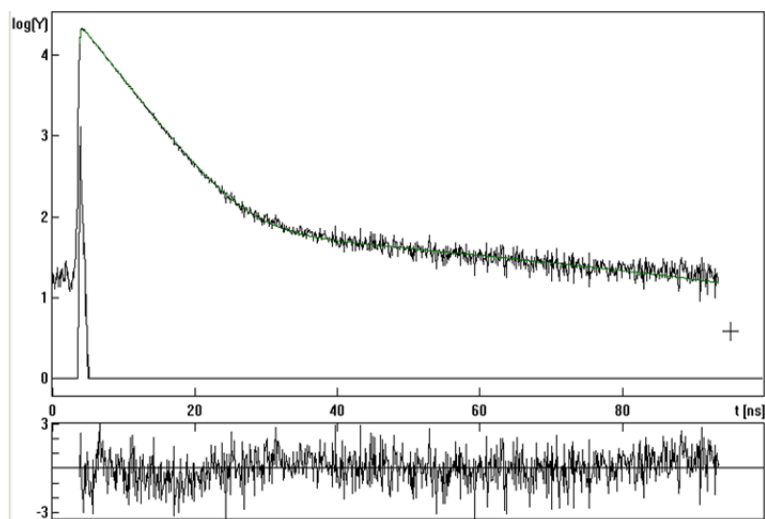


Figure 3.3. Fluorescence decay of mKalama1 at 510 nm excited with a 476 nm pulsed diode at pH 11.25 (upper panel) and multiexponential fit residuals (lower panel).

Irradiation of mKalama1 was carried out using a xenon lamp coupled to a monochromator. mKalama1 at pH 7.5 was irradiated with 385 ± 5 nm light (10 mW/cm^2) for 1, 2, and 5 hours total. The absorption spectra collected at the various intervals show a photoproduct at ~ 338 nm with an isobestic point at 356 nm (Figure 3.4). Irradiation of

the photoproduct at 340 ± 5 nm (2 mW/cm²) for 10 minutes (Figure 3.5) resulted in an increase of the 390 peak. The nature of the 340 nm photoproduct still remains elusive but one cannot rule out the possibility of decarboxylation of E222 to form the neutral chromophore.

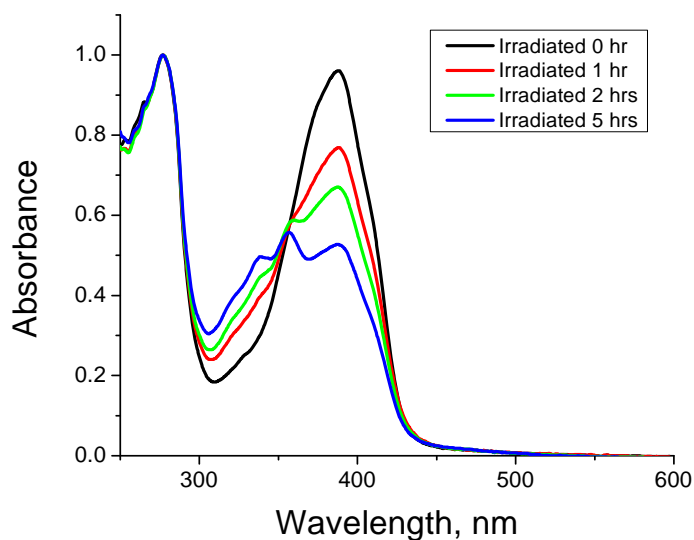


Figure 3.4. Absorption spectra of mKalamal (pH 7.5) irradiated for 0 hours (black), 1 hour (red), 2 hours (green), and 5 hours (blue) with 385 ± 5 nm light (10 mW/cm²). Irradiation of mKalamal was carried out using a xenon lamp coupled to a monochromator.

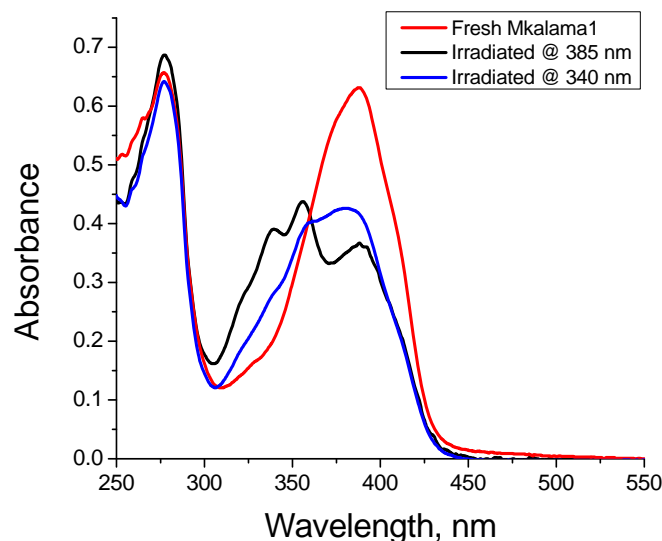


Figure 3.5. Absorption spectra of mKalama1 before irradiation (red), after 4 hours irradiation at 385 nm (black, 10 mW/cm²), and then irradiated at 340 nm (2 mW/cm²) for 10 minutes (blue). Irradiation of mKalama1 was carried out using a xenon lamp coupled to a monochromator.

The subpicosecond TA spectra, acquired at pH 7.5, are shown in Figure 3.1b. Analysis of the transient decays measured at different wavelengths resulted in the same lifetimes of 1.6 ns for all spectral features, which is very close to the average fluorescence lifetime for mKalama1. Therefore, the time evolution of these relatively simple spectra at 740 nm and 445 nm likely arise from the decay of the singlet excited-state population of neutral chromophore ($*Z^N$). Note that the 445 nm band heavily overlaps with the strong negative stimulation emission signal. It is interesting that the fs-ns TA spectra of mKalama1 are very close to the one of *p*-HBDI⁹³ (the synthetic chromophore of the wtGFP and mKalama1), but the S_1 lifetime of the latter is three orders of magnitude shorter due to photoisomerization-induced deactivation.

Increasing the pH resulted in a slight decrease of the major absorption band of the ground-state chromophore at 390 nm concomitant with the appearance of a green band at

505 nm belonging to the chromophore anion, presumably in Z-configuration (Z^A) (Figure 3.1a). The majority of the high pH-induced changes were fully reversible (Figure 3.6), suggesting lack of significant irreversible denaturing of the protein at high pH. Upon increasing pH, a blue shift of the anionic peak was observed. Interestingly, the apparent pK_a value of the protein was unusually high (> 12), much higher than any of the HBDI derivatives. This transition in the optical spectrum is likely caused by titration of nearby amino acids.¹⁰⁹ We assume that the perturbation of the native protein structure at this extremely high pH may lead to the disturbance of the chromophore planar structure leading to the hypsochromic shift in the absorption spectra. Excitation and emission spectra of mKalamal acquired at pH 11.5 demonstrated that the anionic form was also fluorescent with excitation and emission maxima of 470 and 509 nm, respectively (Figures 3.1a and 3.7).

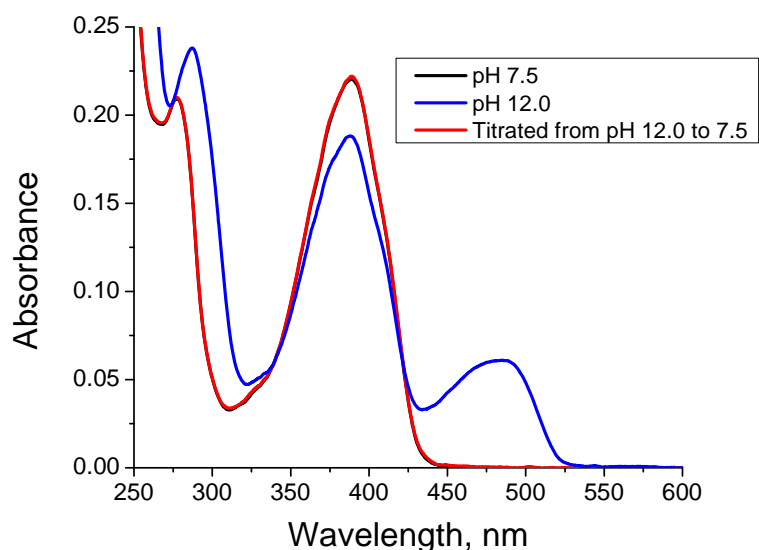


Figure 3.6. Absorption spectra of mKalamal at pH 7.5 (red), at pH 12.0 (blue), and then titrated from pH 12.0 to pH 7.5 (black).

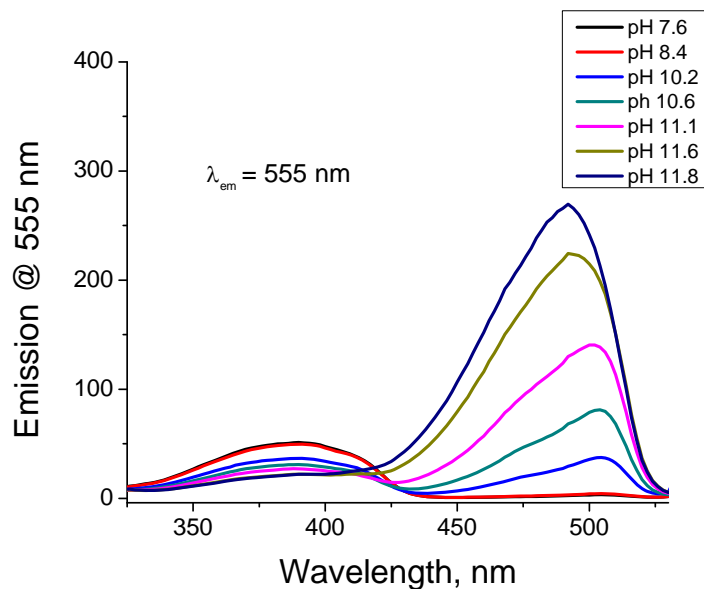


Figure 3.7. Excitation spectra of mKalama1 at various pH ($\lambda_{em} = 555$ nm).

So far, these data show no deviations from the expected behavior of mKalama1 as a brightly fluorescent, inert BFP. However, the microsecond-to-second TA measurements surprisingly reveal the hidden, photoinduced reactivity of this protein. The transient signal in the $1 \mu\text{s} - 2$ ms time window consisted of the ground-state bleach at 385 nm and the TA bands with the 430 nm and 490 nm maxima (Figure 3.1c). Also, a very weak but detectable broad band was detected around 650-700 nm (Figure 3.1c, inset). Upon time evolution, the intensity of the 430 nm peak decreased insignificantly, while the 490 nm band exhibited a slight bathochromic shift and disappeared. The remaining peak at 430 nm was monitored in the 1 ms – 1 min window (Figure 3.1d), where it disappeared at the end of this time interval without any change of the spectral shape. The best fit gave three components with submillisecond time constants: $\tau_1 = 6.2 \pm 1 \mu\text{s}$, $\tau_2 = 98 \pm 10 \mu\text{s}$ and $\tau_3 = 730 \pm 100 \mu\text{s}$, a minor 370 ms component, and very long-lived component (Figure 3.1e).

All submillisecond components have an isosbestic point at 418 ± 1 nm; the two faster components have sharp peaks at 489 nm ($6.2 \mu\text{s}$) and 505 nm ($98 \mu\text{s}$), respectively, both contributing largely to the ~ 490 nm peak of the photolysis (light-*minus*-dark) difference spectrum. The selected kinetic traces and residuals are presented in Figure 3.8.

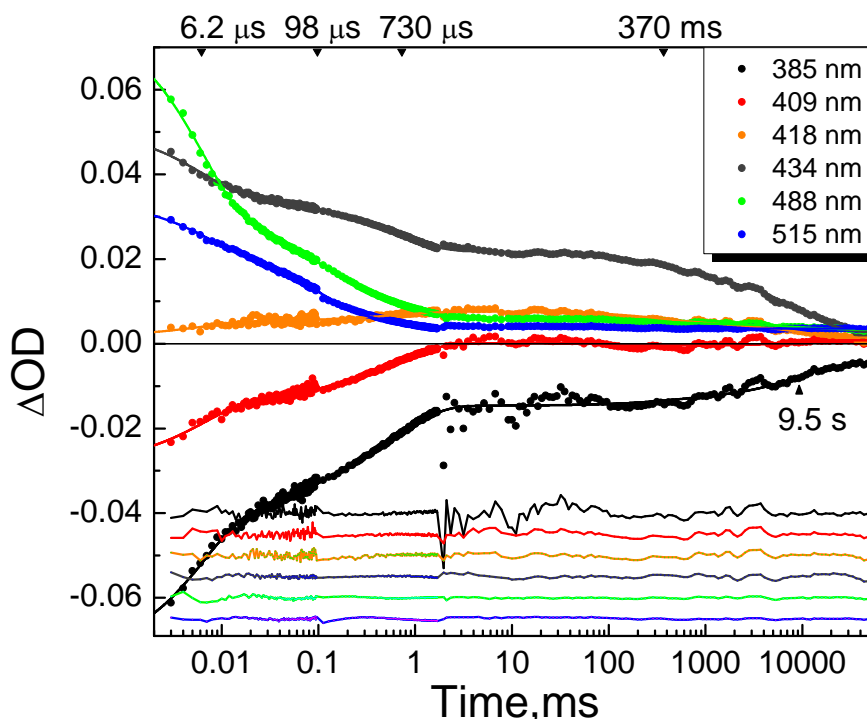


Figure 3.8. Absorbance decays (dots) with kinetic fits (solid lines) at various wavelengths. Residuals displayed at bottom of graph with different vertical offsets. Time constants of the exponential decay components are shown at the top.

Discussion

The observed non-exponential decay of the fluorescence may be caused by either ground state heterogeneity or by chromophore flexibility leading to photoisomerization-induced deactivation which has been shown for both the protein^{110,111} and the free chromophore in all protonation states⁹³. Our group^{112,113} and others¹¹⁴ have demonstrated almost complete restoration of the fluorescence in “locked” compounds. Megley *et al.* have demonstrated the correlation between the phenyl-imidazolone dihedral angle in

several FP chromophores and their fluorescent lifetimes¹¹⁵. However, one cannot ignore other deactivation pathways such as the barrierless torsional deformation of the phenyl single bond.^{116,117}

Based on the striking similarity between the spectra of the 6.2 and 98 μ s TA components at pH 7.5 and the high pH-induced spectra of mKalamal (Figure 3.1a), it is proposed that the submillisecond kinetic phases reflect "delayed" reprotonation of the chromophore ground-state anion. Since the formation of Z^A at pH 7.5 is thermodynamically unfavorable, and the $*Z^A$ form has not been detected in the emission spectra it is concluded that the anionic species detected in the TA spectra at early times at 485 nm is the anion in a twisted configuration (\hat{Z}^A) gradually relaxing to planar Z^A configuration. Supporting our hypothesis for "delayed" reprotonation, the kinetics of the first (6.2 μ s) and second (98 μ s) components exhibited a pronounced 3-fold H/D kinetic isotope effect (Figure 3.9). Comparison of the submillisecond kinetics at various pH shows that the 98 μ s component is sensitive to pH while the 6.2 μ s remains mostly unchanged (Figure 3.10). Therefore the 98 μ s component is attributed to the true reprotonation of the chromophore. Indeed, coupled isomerization/protonation of the ground-state anion is a continuous phenomenon and the two distinct kinetic phases might be not enough for the full description; therefore, the two phases should be regarded as a "first approximation" of the kinetics. Unfortunately, we were unsuccessful in monitoring the submicrosecond TA because the fluorescence of mKalamal "blinds" the detector and the detector does not recover until 1 μ s (our first time point); therefore, we were unable to determine the rise times of the components.

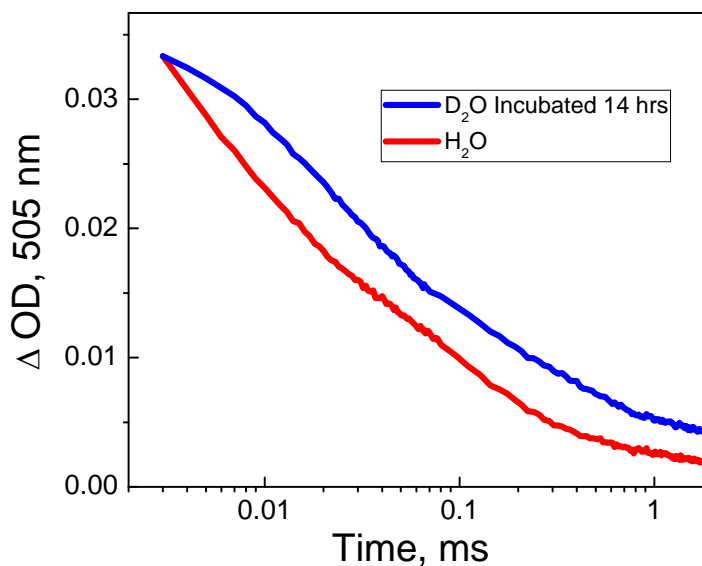


Figure 3.9. TA kinetics at 505 nm for mKalamal in H₂O (red) and for mKalamal incubated in D₂O for 14 h (blue). Kinetics of H₂O was scaled to match intensity of that in D₂O.

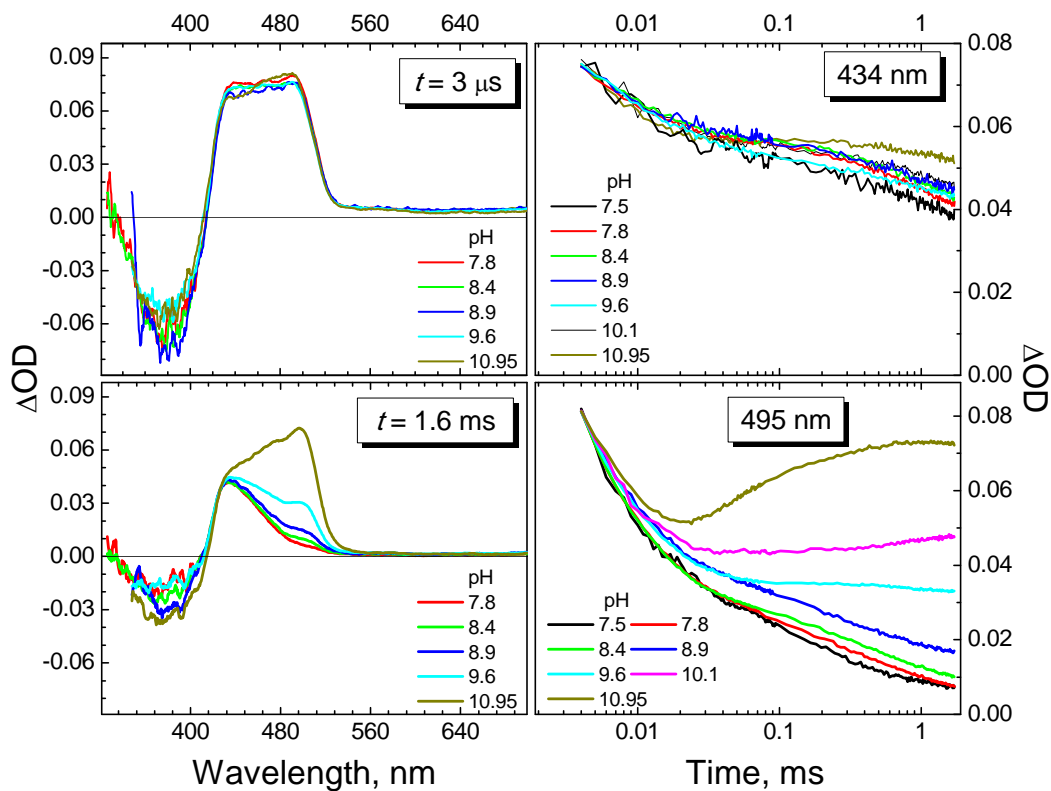


Figure 3.10. Left column: TA spectra of mKalamal at various pH after excitation with a 355 nm laser pulse. Right column: TA decays at various pH.

The decay of the 430 nm TA band (Figure 3.1d) contained the 370 ms and 9.5 s components (Figure 3.1e). However, due to design of the optical setup, where only part of the sample was illuminated, the role of diffusion could not be excluded in the apparent long-time decay of the 430 nm TA band. Therefore, only the lower limit of the lifetime of its transient could be determined. The kinetic and spectral analyses demonstrated that the 430 nm transient had no appreciable rise time, and appeared synchronously with \hat{Z}^A within experimental error. Since the spectral shape of the 430 nm transient did not change over six orders of magnitude in time and its lifetime was much longer than that of $\hat{Z}^A \rightarrow Z^N$ evolution, it was excluded from the photoinduced proton-transfer photocycle (Figure 3.11). The absorption maximum of this transient did not match the spectral windows for any Z^N or Z^A tyrosine-based FPs, which renders its assignment problematic. However, taking into account the bathochromic shift due to encapsulation of the chromophore, the absorption matches that of the radical cation of *p*-HBDI which was observed in both methanol/water and acetonitrile (Figure 3.12).⁹³ This radical cation formation may be responsible for the blinking phenomena observed in many FPs.¹¹⁸ In fact, the same species is observed for wtGFP but only slightly red shifted (Figure 3.15).

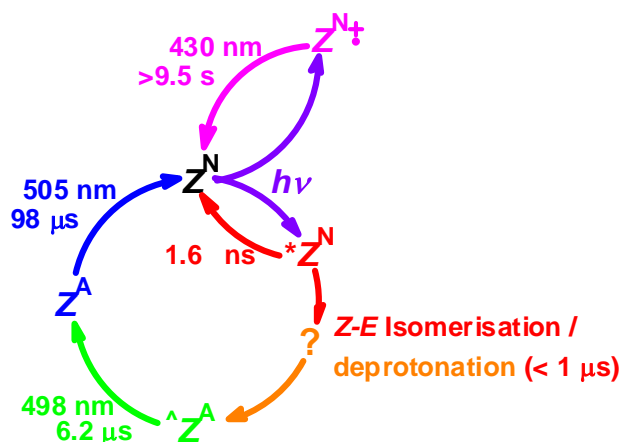


Figure 3.11. Photocycle of mKalama1 showing the characteristic decay times and the wavelengths of the detected intermediates.

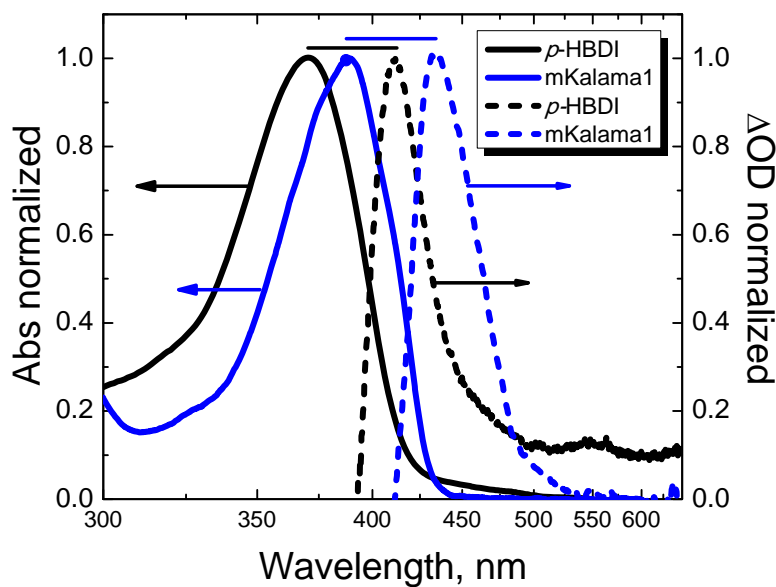


Figure 3.12. Normalized absorption spectra of p-HBDI in methanol (solid black) and mKalama1 (solid blue) with their respective radical cation transients (dotted lines).

There is also a broad, weak absorption band which spans beyond 500 nm (Figures 3.1c and 3.13). It is known that solvated electrons absorb in this region,^{119,120} however, their behavior in protein environments is poorly understood. Solvated electrons were

observed in the photoactive yellow protein containing a *p*-coumaric acid chromophore from the 2 photon photoionization of the chromophore.^{120,121} They have also been observed for the free chromophores of the photoactive yellow protein^{115,118} and of GFP in solution.^{92,93} Therefore, the broad absorption band spanning beyond 500 nm is assigned to the formation of solvated electrons. Presumably, in the protein, the electrons could be stabilized by nearby amino acid residues (similar to solvation). The lifetime of solvated electrons is close to that of the third component (730 μ s) and is also oxygen-sensitive (Figure 3.14). This is not surprising since they can react with oxygen to form superoxide.¹²²⁻¹²⁴ Additionally, long-lived radicals have been detected in various fluorescent proteins upon photolysis using EPR spectroscopy.²⁰ Since the optical absorption extinction coefficient of solvated electron is difficult to estimate, we were unable to determine what fraction of the protein enters a photoinduced pathway producing solvated electrons; however, since the yield of other products is high relative to the solvated electrons, the production of solvated electrons cannot be very efficient in mKalamal.

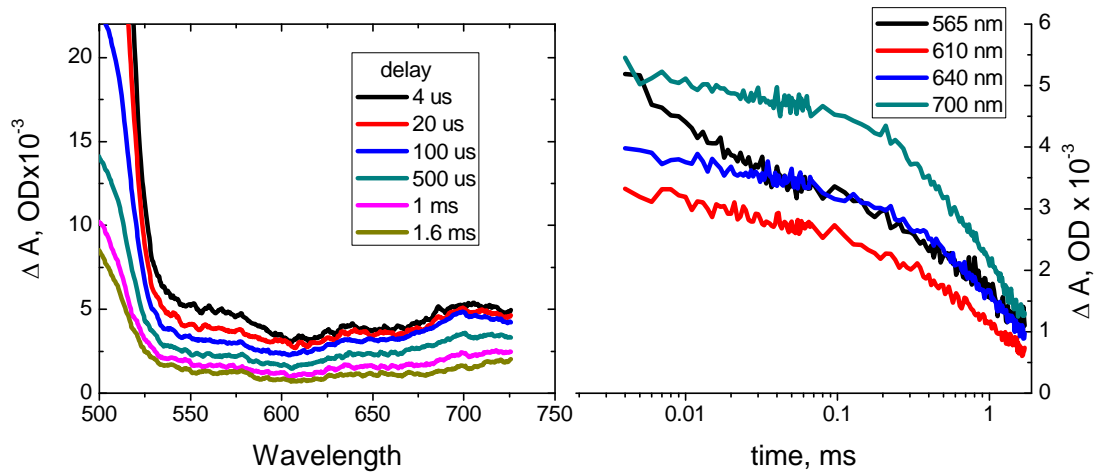


Figure 3.13. TA spectra of Mkalama showing the weak bands from 525 nm to 725 nm (left) with the kinetic traces at selected wavelengths (right).

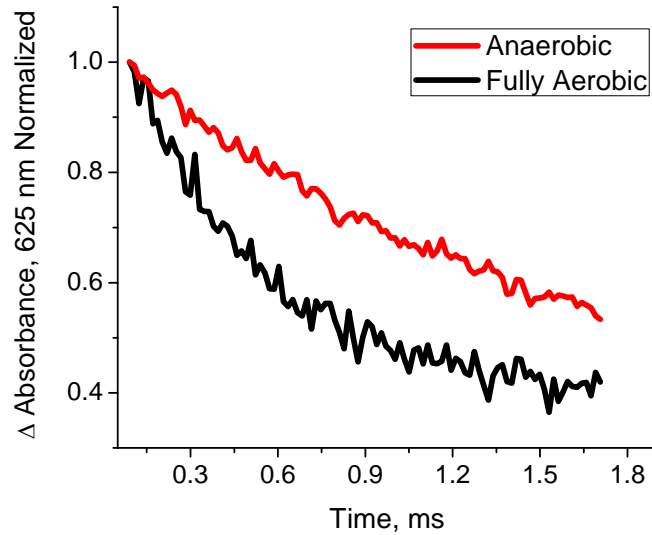


Figure 3.14. TA kinetics at 625 nm for anaerobic conditions (red) and fully aerobic conditions (black).

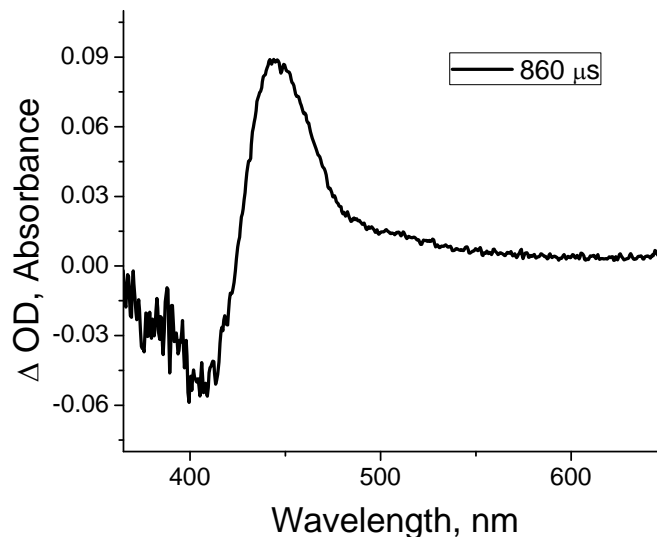


Figure 3.15. Transient absorption time slice at 860 μs for wtGFP (pH 7.5).

The mechanism of the observed photoinduced deprotonation in mKalamal ($*Z^N \rightarrow \hat{Z}^A$) is unknown because of unsuccessful attempts in monitoring the TA at sub- μs timescales due to huge fluorescence intervention. Therefore, the “time zero” in the TA experiment reflects the moment in a protein that has already completed deprotonation and starts the reverse isomerization/reprotonation cycle. The following pathways can be proposed for the submicrosecond processes: i) a $*Z^N \rightarrow E^N$ non-adiabatic isomerization followed by E^N deprotonation or ii) isomerization-coupled non-adiabatic ESPT from $*Z^N$ resulting in \hat{Z}^A . Again, the sequence of isomerization/deprotonation events (parallel/coupled/ consecutive) is unclear since we currently do not have sub- μs data. Furthermore, photoinduced proton transfer does not necessarily require a complete Z - E isomerization of the chromophore, but only a partial twist. Since the spectrum of the third (730 μs) component can be roughly represented as a linear combination of the two faster components, this 730 μs transition can reflect slower phases of chromophore

reprotonation coupled with reverse isomerization; its kinetics can be rate-limited either by slower modes of conformational changes of the chromophore or by proton transfer; however, due to its oxygen sensitivity (Figure 3.16) one cannot rule out the Z^N triplet formation.

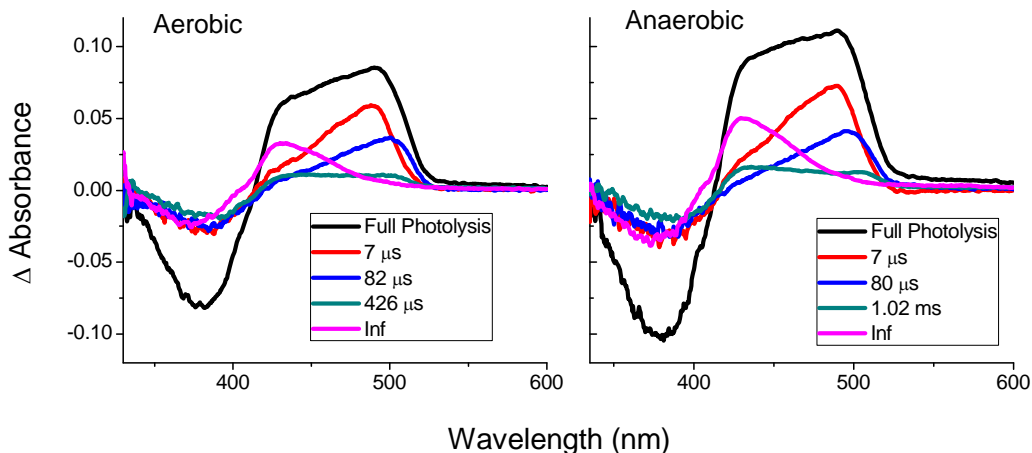


Figure 3.16. Results of the multi-exponential decay fit for mKalamal under aerobic conditions (left) and anaerobic conditions (right). Data was fit using 1 μ s-1.7 ms time frame.

Further corroboration for a reprotonation/deprotonation-isomerization process comes from the study of other GFP variants. It is noteworthy that our timescales match those of the GFP variant GFPmut2, with the 3 mutations S65A, V68L, and S72A.¹²⁵ The photodynamics of GFPmut2 and its variant, E222Q (GFPmut2Q), which is photoswitchable, have been extensively studied using FCS and single wavelength TA.^{101,102,107,126} Bosisio's FCS analysis of the GFPmut2Q revealed 2 components with similar lifetimes to the transients found in mKalamal: a 10-100 μ s component and a 100-600 μ s laser-power-dependent component¹⁰² which were attributed to protonation-

deprotonation of the GFP chromophore and excited-state conformational dynamics, respectively.

Lastly, Krishnamoorthy *et al.* investigated the sub-millisecond protonation dynamics of the chromophore in the S65T variant of the GFP using pH-jump experiments.¹²⁷ They proposed that protonation was a sequential process involving two steps: a) proton transfer from solvent to the chromophore, and b) internal structural rearrangements to stabilize a protonated chromophore. They also used the same pH-jump experiments to investigate the kinetics of proton transfer in wtGFP and found that the rate of proton transfer was inversely proportional to solvent viscosity, suggesting that the rate-limiting step was transfer of the protons through the protein matrix, i.e. that protein dynamics controlled the rate of proton transfer.¹²⁸ Investigation of a YFP (YFP 10C) demonstrated that protonation of the chromophore was a 2 step process¹²⁹ similar to what we observe in mKalama1 but on different timescales.

It is noteworthy that similar photoinduced behavior (photoionization and photoisomerization/deprotonation) was observed in the GFP mutant T203V/S205V but the kinetics of the TA is indeed a bit different (Figure 3.17). Since the crystal structures of mKalama1 and T203V/S205V haven't been reported, the published structure of the GFP S205V mutant (PDB: 2QLE) was used to identify possible proton acceptors. Based on the GFP S205V crystal structure, Y145 and H148 were identified as possible proton acceptors (for chromophore Z^N state, Figure 3.18) but these residues are hydrophobic in mKalama1 (Y145M and H148G) and therefore we rule out their role in the photoinduced proton transfer. By modeling various twisted states of the chromophore into the crystal structure (Figure 3.19), we identified H180 (conserved in mKalama1) as a possible

proton acceptor if twisting/isomerization plays a role. Again, it is difficult to say what effect the 23 mutations from T203V to mKalamal have had on the overall structure, so we can only draw parallels between the two.

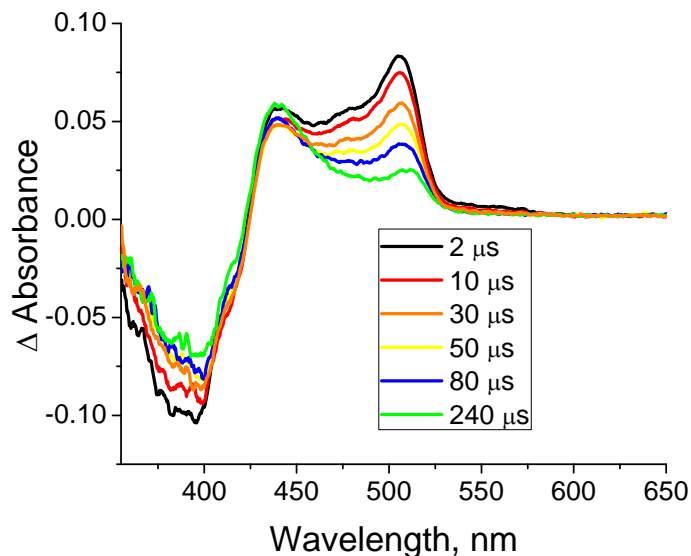


Figure 3.17. TA time slices for wtGFP T203V/S205V after 355 nm excitation.

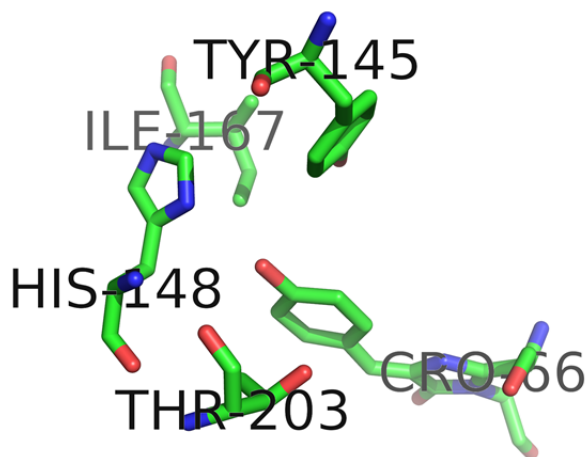


Figure 3.18. The chromophore of GFP T203V (PDB 2QLE) and nearby residues. Drawn using the PyMOL Molecular Graphics System, Version 1.2r3pre, Schrödinger, LLC.

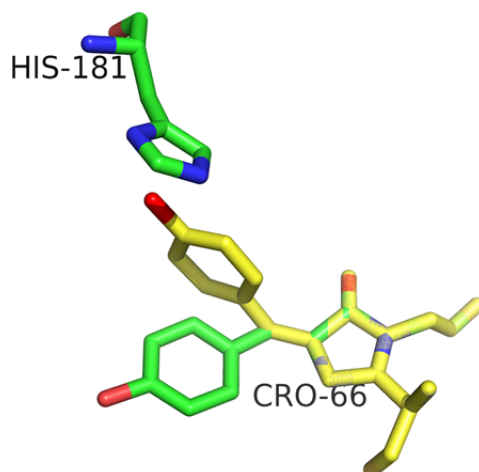


Figure 3.19. The chromophore of GFP T203V (PDB 2QLE) is shown in a slightly twisted version (yellow) to illustrate H180 as possible proton acceptor. Drawn using the PyMOL Molecular Graphics System, Version 1.2r3pre, Schrödinger, LLC.

Conclusions

In conclusion, for the first time, broadband TA spectroscopy measurements in the μs -s time scale were used to identify the dark states in the blue fluorescent protein mKalama1. The complete photocycle of this protein spanning fifteen orders of time magnitude was established (Figure 3.11). The combination of the TA at pH 7.5 and pH-titration data indicate that mKalama1 undergoes a photoinduced proton transfer. The 3-fold isotope effect exhibited by the $6.2 \mu\text{s}$ (Z^A) and $98 \mu\text{s}$ (Z^A) components point to bond making/breaking. This isotope effect and the hydrophobic nature of the chromophore pocket in the Z^N state suggests that the chromophore likely undergoes isomerization or twisting in order to deprotonate. The TA data and previously published results suggest the formation of a radical cation (Z^{N+} , $\tau \geq 9.5\text{s}$, Figure 3.11) and solvated electrons by two photon excitation of the chromophore.

Prior to this work, no full spectral information about the transients appearing at μs -s times was available, and the mechanistic details of photoinduced processes in FPs have remained elusive. Certainly, the reactivity of other fluorescent proteins will differ drastically since most GFPs and RFPs are already deprotonated in the ground state. This unique, previously unexplored reactivity of fluorescent proteins will not only bring understanding of the photoinduced dynamics in FPs, but also demonstrates low-frequency fluorescence modulation, the keystone of modern super-resolution microscopy.¹³⁰

CHAPTER 4

OPTICAL MODULATION OF FLUORESCENT PROTEINS

Introduction

The development of fluorescent probes, as well as advances in fluorescence microscopy, has revolutionized molecular biology, providing the basic tools to help investigate and understand complex processes in living cells. However, a common problem is the relatively poor signal-to-noise ratio, which causes background fluorescence to overwhelm the artificially induced fluorescence from the exogenous and endogenous fluorophores. Therefore, further advances in development of fluorescent probes and optics are needed in order to perform true single molecule studies.

Photoswitchable fluorescent proteins such as Dronpa,⁵¹ its fast-switchable variant rsFastLime14,¹³¹ and mTFP0.7¹³² have attracted much attention over the years due to their ability to be switched between fluorescent on-states and dark off-states and therefore yield sensitivity gains over non-photoswitchable fluorescent proteins. The proteins typically yield emission when illuminated until the chromophore stochastically switches into the non-fluorescent off-state. The fluorescence can then be restored upon excitation at shorter wavelengths. *Z-E* isomerization of the chromophore as well as protonation-deprotonation events are responsible for their photoswitching behavior.^{50,51,132} Alternatively, if these dark states were transient, eventually relaxing back to the fluorescent on-state, one could optically depopulate this state and therefore accelerate relaxation back to the ground state and modulate the fluorescence. Optical depopulation of the transient dark state would have to be lower in energy than the collected

fluorescence to avoid the increase of background fluorescence. Thus, the ideal system would be one in which the dark (*E*) state would be transient, undergoing either photoinduced *E-Z* isomerization or, conversely, thermal reconversion on a slower time scale. We note, parenthetically, that the range of such lifetimes ranges from “long”, i.e., isolable *E* proteins, to very short, i.e., “blinking”. The “sweet” spot for modulatable fluorophores, therefore, lies between the two extremes where data acquisition at an acceptable rate allows images to be acquired.

Fluorescence modulation has already been achieved through the use of exogenous fluorophores.^{133,134} The Dickson group has developed single-stranded DNA (ssDNA)-encapsulated Ag nanodot-based fluorophores, which have improved photostability and much lower incident intensities than most photoswitching fluorophores.^{133,135} These have been used to extract signals from high fluorescence backgrounds of cyanine 5. Although these types of fluorophores hold great promise, it would be much more beneficial to have endogenous, genetically encoded fluorophores. Therefore, attention has been focused on developing fluorescent proteins capable of modulation based fluorescence enhancement.

Starting with the two BFPs mKalamal and GFP T203V/S205V, a series of mutations were made in order to generate modulatable fluorescent proteins. The intention was to use a secondary wavelength, red shifted from the emission, to depopulate dark states and thereby increase the overall fluorescence. In wtGFP the anionic chromophore is ~80 nm red-shifted from the neutral, therefore the goal was to create a BFP (incapable of ESPT with only the neutral form of chromophore present in ground state) based off the tyrosine moiety that is capable of photoisomerization. Thus, the *E* state would be

transient and anionic, and therefore, could be modulated at longer secondary wavelengths than the emission (Figure 4.1).

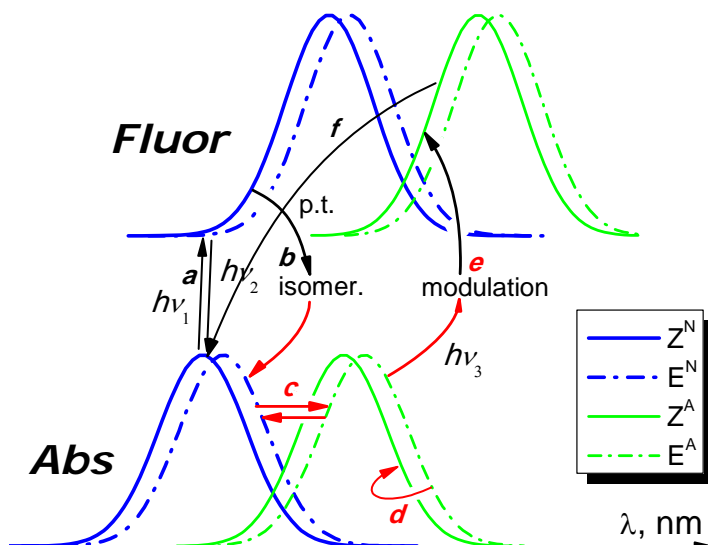


Figure 4.1. Spectral representation of strategy behind the research: a) excitation of Z^N ; b) excited state isomerization and relaxation of Z^{N*} ; c) acid-base equilibration; d) ground-state isomerization of E^A ; e) excitation and photoisomerization of E^A (modulation); f) relaxation and reprotonation of Z^A .

This work was extended to include green fluorescent proteins. The PFP Padron*, which has 10 mutations to the PFP Dronpa,³³ is capable of modulation based fluorescence enhancement using 476 nm primary and 561 nm secondary excitation. A series of mutations were carried out to optimize the frequencies used for modulation.

Materials and Methods

Protein expression and purification

The gene encoding mKalama1 was purchased from AddGene (Cambridge, MA). The gene is inserted between the *XhoI* and *EcoRI* restriction sites in pBAD-His B and contains an N-terminal hexahistidine tag. The plasmid was transformed into *E. coli* DH5 α Pro. A 5 mL culture was inoculated into 1 L of LB containing 50 μ g/mL of ampicillin, grown to an OD600 of 0.5 at 37 °C (2-3 h), and protein expression was induced with 0.2% arabinose. The gene encoding GFP-F99S/M153T/V163A/T203V/S205V was obtained from Jim Remington (Oregon). The gene encoding Padron* was obtained from Marin Andresen (Max Planck Institute for Biophysical Chemistry, Göttingen, Germany). The genes encoding GFP-F99S/M153T/V163A/T203V/S205V and Padron* were inserted between *BamHI* and *HindIII* restriction sites in PQE-30 and each protein contains an N-terminal hexahistidine tag. The plasmids were transformed into *E. coli* M15 cells. A 5 mL culture was inoculated into 1L of LB containing 50 μ g/mL of ampicillin, grown to an OD600 of 0.5 at 37 °C (2-3 h), and then induced with 1 mM IPTG. Proteins were expressed to 20% of total cell protein and purified the protein via Ni²⁺-NTA-immobilized metal affinity chromatography (IMAC). All measurements were performed in phosphate buffer (50 mM sodium phosphate, 250 mM NaCl, pH 7.5) unless otherwise stated.

Site-directed mutagenesis

Mutagenesis of the mKalama1, GFP-F99S/M153T/V163A/T203V/S205V, and Padron* genes were performed using the rapid-PCR (polymerase chain reaction) site-directed mutagenesis method.⁷¹ The PCR reaction was carried out using the same protocol as in

the materials and methods of Chapter 2. Primers for the mutants of mKalama1, Padron*, and GFP-F99S/M153T/V163A/T203V/S205V are found in Tables 4.1-4.6. Transformation of the mutant DNA was carried out by adding 2 μ L of the reaction mixture to 100 μ L of XL1-Blue competent cells. The cells were heated to 42°C for 1 minute to increase the permeability. Then, 400 μ L of LB was added and the sample was incubated in a thermomixer at 37°C for 1 hour with shaking at 700 RPM. The sample was then plated on agar plates containing LB and ampicillin. Colonies were picked, grown overnight, and the DNA was extracted and purified using the QIAprep Spin Miniprep kit (Qiagen, USA). The purified DNA was sent to Eurofins MWG Operon (Huntsville, Alabama) where sequencing analysis confirmed the amplified product.

Table 4.1. Forward (F) and reverse (R) primers used to generate mutants of GFP-F99S/M153T/V163A/T203V/S205V.

Mutation	Primers
Y145K	F: 5' CTTGGACACAAATTGGAATACAACAAAACTCACACAATGTATACATCACC 3'
	R: 5' GGTGATGTATACATTGTGTGAGTTTTTGTGTATTCCAATTTGTGTCCAAG 3'
H148K	F: 5' GACACAAATTGGAATACAAC TATAACTCAAAGAATGTATACATCACCGCAGACAAAC 3'
	R: 5' GTTTGTCTGCGGTGATGTATACATTCTTTGAGTTATAGTTGTATTCCAATTTGTGTGC 3'
H148R	F: 5' GACACAAATTGGAATACAAC TATAACTCAAGAAATGTATACATCACCGCAGACAAAC 3'
	R: 5' GTTTGTCTGCGGTGATGTATACATTCTTTGAGTTATAGTTGTATTCCAATTTGTGTGC 3'
H148G	F: 5' CAAATTGGAATACAAC TATAACTCAGGCAATGTATACATCACCGCAG 3'
	R: 5' CTGCGGTGATGTATACATTGCCTGAGTTATAGTTGTATTCCAATTTG 3'
H148D	F: 5' CAAATTGGAATACAAC TATAACTCAGACAATGTATACATCACCGCAG 3'
	R: 5' CTGCGGTGATGTATACATTGCTGAGTTATAGTTGTATTCCAATTTG 3'
H148Y	F: 5' CACAAATTGGAATACAAC TATAACTCATAAATGTATACATCACCGCAGAC 3'
	R: 5' GTCTGCGGTGATGTATACATTGTATGAGTTATAGTTGTATTCCAATTTGTG 3'
T203K	F: 5' CAGACAACCATTACCTGTCCAAACAAGTCGCCCTCTCAAAAG 3'
	R: 5' CTTTGTGAGAGGGCGACTTGTGTTGGACAGGTAATGGTTGTCTG 3'
S147K	F: 5' GACACAAATTGGAATACAAC TAAACAACAATGTATACATCACCGCAG 3'
	R: 5' CTGCGGTGATGTATACATTGTGTTTGTATAGTTGTATTCCAATTTGTGTGC 3'

Table 4.2. Forward (F) and reverse (R) primers used to generate mutants of GFP-F99S/M153T/V163A/T203V/S205V.

Mutation	Primers
S147R	F: 5' CACAAATTGGAATACAAC TATAACAGACACAATGTATACATCACCGC 3'
	R: 5' GCGGTGATGTATACATTGTGTCTGTTATAGTTGTATTCCAATTTGTG 3'
F165H	F: 5' GAATGGAATCAAAGCGAAC CACAAAATTAGACACAACATTGAAG 3'
	R: 5' CTTC AATGTTGTGTCTAATTTTGTGGTTCGCTTTGATTCCATT C 3'
Q183E	F: 5' GTTCAACTAGCAGACCATTATGAACAAAATACTCCAATTGGCG 3'
	R: 5' CGCCAATTGGAGTATTTTGTTCATAATGGTCTGCTAGTTGAAC 3'
V150A	F: 5' GAATACAAC TATAACTCACACAATGCATACATCACCGCAGACAAAACAAAAG 3'
	R: 5' CTTTTGTTTGTCTGCGGTGATGTATGCATTGTGTGAGTTATAGTTGTATT C 3'
F165L	F: 5' CAAAAGAATGGAATCAAAGCGAACCTGAAAATTAGACACAACATTGAAGATGG 3'
	R: 5' CCATCTTCAATGTTGTGTCTAATTTTCAGGTTTCGCTTTGATTCCATTCTTTT G 3'
F165D	F: 5' GAATGGAATCAAAGCGAACGACAAAATTAGACACAACATTGAAG 3'
	R: 5' CTTC AATGTTGTGTCTAATTTTGTTCGTTTCGCTTTGATTCCATT C 3'
Q183A	F: 5' GTTCAACTAGCAGACCATTATGCACAAAATACTCCAATTGGCG 3'
	R: 5' CGCCAATTGGAGTATTTTGTGCATAATGGTCTGCTAGTTGAAC 3'

Table 4.3. Forward (F) and reverse (R) primers used to generate mutants of mKalama1.

Mutation	Primers
G194H	F: 5' GGAGTACAACATGAACGTCCACAACGTCTATATCACGGCC 3'
	R: 5' GGCCGTGATATAGACGTTGTGGACGTTTCATGTTGTACTCC 3'
G149K	F: 5' GGAGTACAACATGAACGTCAAGAACGTCTATATCACGGCC 3'
	R: 5' GGCCGTGATATAGACGTTCTTGACGTTTCATGTTGTACTCC 3'

Table 4.4. Forward (F) and reverse (R) primers used to generate mutants of Padron*.

Mutation	Primers
H194V	F: 5' CTATCACTCTGTGGACCACGTCATTGAGATTA AAAAGCCACGAC 3'
	R: 5' GTCGTGGCTTTTAATCTCAATGACGTGGTCCACAGAGTGATAG 3'
H194I	F: 5' CTATCACTCTGTGGACCACATCATTGAGATTA AAAAGCCACGAC 3'
	R: 5' GTCGTGGCTTTTAATCTCAATGATGTGGTCCACAGAGTGATAG 3'
H194N	F: 5' CTATCACTCTGTGGACCACAACATTGAGATTA AAAAGCCACGAC 3'
	R: 5' GTCGTGGCTTTTAATCTCAATGTTGTGGTCCACAGAGTGATAG 3'
H194L	F: 5' CTATCACTCTGTGGACCACCTGATTGAGATTA AAAAGCCACGACAAAG 3'
	R: 5' CTTTGTCGTGGCTTTTAATCTCAATCAGGTGGTCCACAGAGTGATAG 3'
H194M	F: 5' CTATCACTCTGTGGACCACATGATTGAGATTA AAAAGCCACGACAAAG 3'
	R: 5' CTTTGTCGTGGCTTTTAATCTCAATCATGTGGTCCACAGAGTGATAG 3'
H194C	F: 5' CTATCACTCTGTGGACC ACTGCATTGAGATTA AAAAGCCACGAC 3'
	R: 5' GTCGTGGCTTTTAATCTCAATGCAGTGGTCCACAGAGTGATAG 3'
H194T	F: 5' CTATCACTCTGTGGACCACACCATTGAGATTA AAAAGCCACGAC 3'
	R: 5' GTCGTGGCTTTTAATCTCAATGGTGTGGTCCACAGAGTGATAG 3'
H194D	F: 5' CTATCACTCTGTGGACCACGATATTGAGATTA AAAAGCCACGAC 3'
	R: 5' GTCGTGGCTTTTAATCTCAATATCGTGGTCCACAGAGTGATAG 3'

Table 4.5. Forward (F) and reverse (R) primers used to generate mutants of Padron*.

Mutation	Primers
H194P	F: 5' CTATCACTCTGTGGACCACCCGATTGAGATTA AAAAGCCACGACAAAG 3'
	R: 5' CTTTGTCGTGGCTTTTAATCTCAATCGGGTGGTCCACAGAGTGATAG 3'
H194S	F: 5' CTATCACTCTGTGGACCACAGCATTGAGATTA AAAAGCCACGAC 3'
	R: 5' GTCGTGGCTTTTAATCTCAATGCTGTGGTCCACAGAGTGATAG 3'
H194A	F: 5' CTATCACTCTGTGGACCACGCCATTGAGATTA AAAAGCCACGAC 3'
	R: 5' GTCGTGGCTTTTAATCTCAATGGCGTGGTCCACAGAGTGATAG 3'
H194W	F: 5' CTATCACTCTGTGGACC ACTGGATTGAGATTA AAAAGCCACGACAAAG 3'
	R: 5' CTTTGTCGTGGCTTTTAATCTCAATCCAGTGGTCCACAGAGTGATAG 3'
H194Y	F: 5' CTATCACTCTGTGGACC ACTACATTGAGATTA AAAAGCCACG 3'
	R: 5' CGTGGCTTTTAATCTCAATGTAGTGGTCCACAGAGTGATAG 3'
H194F	F: 5' CTATCACTCTGTGGACC ACTTCATTGAGATTA AAAAGCCACGAC 3'
	R: 5' GTCGTGGCTTTTAATCTCAATGAAGTGGTCCACAGAGTGATAG 3'
H194Q	F: 5' CACTCTGTGGACC ACCAGATTGAGATTA AAAAGCCACGAC 3'
	R: 5' GTCGTGGCTTTTAATCTCAATCTGGTGGTCCACAGAGTG 3'
H194R	F: 5' CTATCACTCTGTGGACC ACCGCATTGAGATTA AAAAGCCACGACAAAG 3'
	R: 5' CTTTGTCGTGGCTTTTAATCTCAATGCGGTGGTCCACAGAGTGATAG 3'

Table 4.6. Forward (F) and reverse (R) primers used to generate mutants of Padron*.

Mutation	Primers
H194K	F: 5' GACTATCACTCTGTGGACCACAAAATTGAGATTA AAAAGCCACGAC 3'
	R: 5' GTCGTGGCTTTTAATCTCAATTTTGTGGTCCACAGAGTGATAGTC 3'
G157T	F: 5' GGAGTGCTGAAGTCTGATACCAACTACGCTCTGTCGCTTG 3'
	R: 5' CAAGCGACAGAGCGTAGTTGGTATCAGACTTCAGCACTCC 3'
G157E	F: 5' GGAGTGCTGAAGTCTGATGAAA ACTACGCTCTGTCGCTTG 3'
	R: 5' CAAGCGACAGAGCGTAGTTTTTCATCAGACTTCAGCACTCC 3'
G157S	F: 5' GGAGTGCTGAAGTCTGATTCTAACTACGCTCTGTCGC 3'
	R: 5' GCGACAGAGCGTAGTTAGAATCAGACTTCAGCACTCC 3'
S142V	F: 5' GACTGTGAAATGGGAGCGGGTGACTGAGAAATTGTATGTGCG 3'
	R: 5' CGCACATACAATTTCTCAGTCACCCGCTCCCATTTACAGTC 3'
H193L	F: 5' GACTATCACTCTGTGGACCTCCACATTGAGATTA AAAAGCC 3'
	R: 5' GGCTTTTAATCTCAATGTGGAGGTCCACAGAGTGATAGTC 3'
H193A	F: 5' CAGACTATCACTCTGTGGACGCGCACATTGAGATTA AAAAGCCAC 3'
	R: 5' GTGGCTTTTAATCTCAATGTGCGCGTCCACAGAGTGATAGTCTG 3'
H193K	F: 5' CAGACTATCACTCTGTGGACAAACACATTGAGATTA AAAAGCCAC 3'
	R: 5' GTGGCTTTTAATCTCAATGTGTTTGTCCACAGAGTGATAGTCTG 3'

Modeling of chromophore

Modeling the Z form of the chromophore was done in PyMOL. The chromophore was saved and exported to ChemBioDraw where it was rotated 180° to simulate the Z form. It was then saved and reopened in PyMOL. No energy minimization was performed.

Work in the Dickson group. The following two experimental sections are included for the sake of completeness and are abstracted from the experimental section provided by Amy Jablonski. The data on modulation efficiency was also obtained by Amy Jablonski.

Fluorescence microscopy

Microscopy was performed on an inverted microscope (Olympus IX71) using a 60x water-immersion objective (Olympus 1.2 NA). All solution data was taken by focusing 30 microns into solution. The signal was collected in a confocal arrangement with a 100- μm multimode fiber serving as the pinhole and directing the emission to a photon counting avalanche photodiode (APD, Perkin-Elmer). Intensity trajectories were recorded using a Becker-Hickl (SPC 630) or Time Harp (Picoquant) photon counting module. Continuous wave primary excitation was used near the excitation maximum of the blue fluorescent proteins (405 nm) using a temperature controlled fiber-coupled diode (ThorLabs). Pulsed excitation was produced by laser diode (Picoquant) at 372 nm and a repetition rate of 10 MHz. A tunable Ar^+ laser (Coherent) was used as secondary excitation. Appropriate band pass filters centered near the emission wavelength of BFPs were used to efficiently block both primary and secondary laser excitation. For dual-laser excitation experiments, lasers were overlapped using a dichroic mirror prior to entering the microscope. Modulation of the secondary laser was performed with an electro-optical modulator (EOM, ConOptics, Model 350-210) with square wave input. Unless otherwise stated, primary intensities were 500 W/cm^2 at 405 nm and 178 W/cm^2 at 372 nm. Secondary intensities (514 nm) were 76 kW/cm^2 for both cases.

Data analysis^a

Modulated sample time traces were binned at a rate at least 2.2 times faster than the highest modulation frequency used. Fourier transformations of the time traces reveal the

^a Work performed by Amy Jablonski

modulation frequency component. The frequency component is divided by the DC component and multiplied by two to determine the enhancement. Modulation depth, m vs. modulation frequency, ν_{mod} , curves enabled extraction of characteristic frequencies through Equation 4.1:

$$m = a(1 + (2\pi\nu_{\text{mod}}\tau)^2)^{1/2} \quad (\text{Eq. 4.1})$$

where a is the maximum modulation depth, ω is the angular frequency, and τ is the characteristic lifetime. The characteristic frequency is defined by the frequency at which the modulation depth drops to 50% of its original value.

Results

Starting with wtGFP T203V/S205V, the mutations F99S/M153T/V163A were incorporated via site-directed mutagenesis. These mutations are known to increase folding efficiency and brightness while not directly interacting with the chromophore.^{136,137} The wtGFP F99S/M153T/V163A/T203V/S205V will be referred to as T203V/S205V from here on for simplicity. It should be noted that mKalamal already contains the M153T and V163A mutation but not F99S. Mutations to T203V/S205V were guided by the published crystal structure of wtGFP T203V (PDB code: 2QLE)³⁴ and were chosen based on their proximity to the chromophore in both Z and E isomers with the goal of affecting isomerization efficiency and thereby altering the modulation depth and frequency. Mutations around the chromophore can drastically affect the range of isomerization lifetimes and the “sweet” spot for modulatable fluorophores lies between the two extremes, where data acquisition at an acceptable rate allows images to be acquired; therefore, each key surrounding residue (Figure 4.2) was mutated to a variety of

amino acids. The mutants were expressed and those which matured were purified and analyzed by fluorescence microscopy.

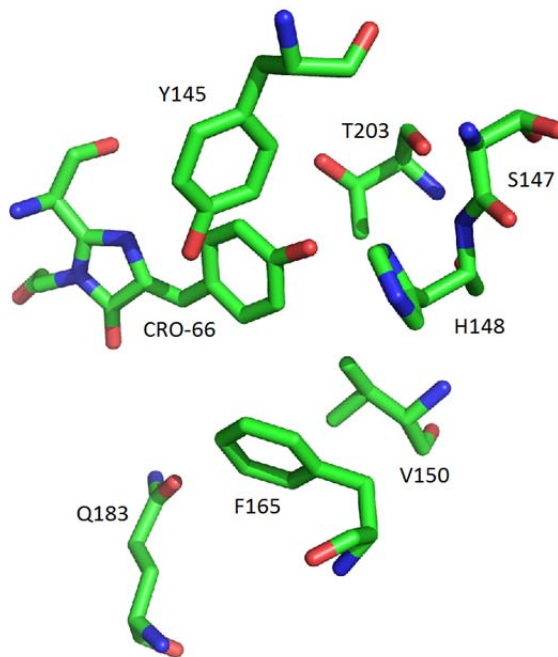


Figure 4.2. Chromophore of GFP T203V (PDB 2QLE) with key surrounding residues. Drawn using the PyMOL Molecular Graphics System, Version 1.2r3pre, Schrödinger, LLC.

The ground state absorption spectra of T203V/T205V (Figure 4.3) and all of its mutants (Figures B.1-B.10) have a λ_{\max} at ~ 390 nm corresponding to the neutral chromophore and a shoulder at ~ 505 nm (pH 7.5) due to the anionic *E* or *Z* form. Irradiation of T203/S205V and its mutants resulted in a decrease of the main absorption peak and an increase in the anionic form (Figures 4.3 and B.1-B.10). Both peaks were slightly blue-shifted following irradiation. The bleaching of these proteins is very similar to that of wtGFP and likely occurs through a decarboxylation mechanism as well.¹⁶

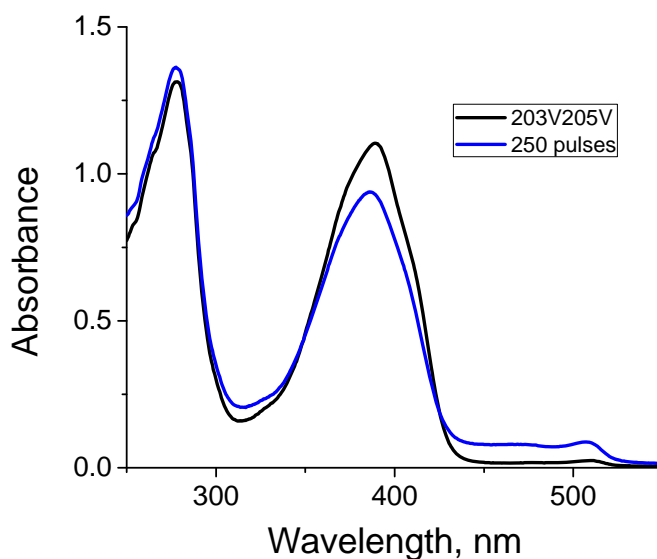


Figure 4.3. Ground state absorption spectra of T203V/S205V before and after irradiation with 355 nm light.

Co-excitation of T203V/S205V with 405 nm primary (cw) and 514 nm secondary excitation yields a 4% enhancement in fluorescence (Table 4.7).^b This fluorescence enhancement arises from establishing a steady state dark population with the primary laser, coupled with rapid depopulation with the secondary laser and can be defined as the ratio of emission produced from dual-laser excitation to that with single-laser illumination. The characteristic frequency can be obtained from the sum of the rate out of the bright state and the natural dark state decay, $k_{\text{bright}} + k_{\text{decay}}$. Therefore, modulating the secondary wavelength intensity can dynamically increase or decrease the dark state population and alter the collected fluorescence. The variants of T203V/S205V are shown in Table 4.1 with the H148K mutant giving the best enhancement (15%) and F165L yielding virtually no enhancement.

^b Work performed by Amy Jablonski

As k_{bright} is the product of excitation rate, k_{exc} , and dark state quantum yield, ϕ_{dark} , this rate generally increases with primary laser intensity. Consequently, increased primary excitation should simultaneously increase modulation depth and characteristic modulation frequency, as observed for other modulatable species.¹³⁵ Plotting characteristic frequency vs. primary intensity should yield a line that, extrapolated to zero primary intensity, yields k_{decay} as the y-intercept. The inverse of this rate gives the natural dark state decay time that, when coupled with the characteristic frequency, also yields the time spent in the fluorescent manifold ($\tau_{\text{bright}} = k_{\text{bright}}^{-1}$). The characteristic times for a given set of excitation conditions are given in Table 4.1. As the primary intensity decreases, the characteristic frequencies of the T203V/S205V and H148K also decrease (Figure 4.4 B).^c The low primary intensity k_{decay} values of both mutants are very similar at ~ 6 Hz. It is clear that the photophysics are quite different in the τ_{bright} at 560 W/cm^2 with approximate lifetimes for T203V/S205V and H148K of ~ 100 ms and ~ 30 ms, respectively. This indicates more efficient photoinduced dark state formation in H148K compared to that in the double mutant. As enhancement is dictated by the ratio of the off-time and on-time, the recorded photophysical times support the best enhancement of H148K (Table 4.7).

^c Data provided by Amy Jablosnki

Table 4.7. Photophysical parameters of T203V/S205V mutations for cw 405 nm excitation.*Low fluorescence enhancements make absolute frequencies hard to obtain, so these are not very reliable.

Mutation	Enhancement (%)	Characteristic Frequency (Hz)	τ_{bright} (ms)	τ_{decay} (ms)
Wild-type	4	16	100	167
H148D	4	47	66	114
H148G	6	30	57	222
H148K	15	37	32	167
H148R	3	5*		
H148Y	2	6*		
V150A	10	47	40	164
F165H	2	10*		
F165L	0	N/A	N/A	N/A

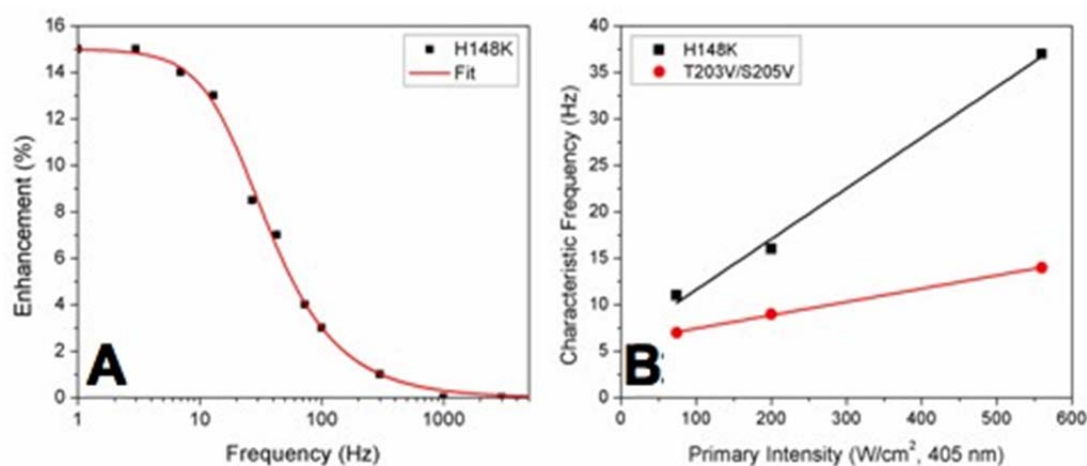


Figure 4.4. A) Enhancement as a function of modulation frequency fit to phase-resolved lifetime equations. B) Characteristic frequencies are plotted as a function of 405 nm primary excitation for T203V/S205V and T203V/S205V/H148K. Linear fit was performed to obtain the natural k_{decay} of each protein.

The fluorescence enhancement versus primary intensity for 405 nm is shown for both T203V/S205V and its mutant H148K (Figure 4.5 B).^d Unexpectedly, all fluorescent

^d Data provided by Amy Jabloski

proteins exhibited a decrease in fluorescence enhancement upon increasing primary intensity. Therefore, the primary intensity must be optimized to populate the dark state while avoiding an increase in its decay rate. The most optimal intensity achieved was less than $\sim 100 \text{ W/cm}^2$.

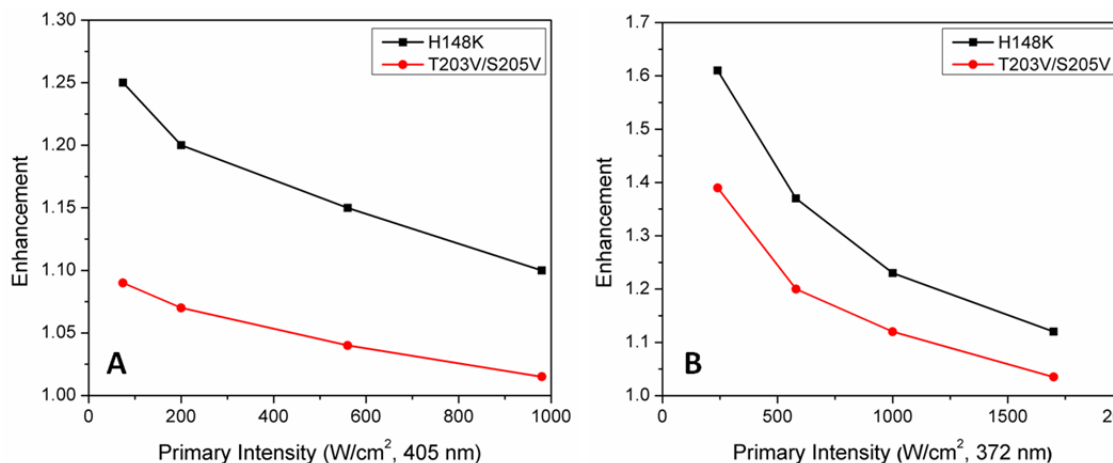


Figure 4.5. Enhancement factor versus primary intensity of (A) 405 nm and (B) 372 nm excitation of T203V/S205V and T203V/S205V/H148K. Enhancement factor of 1.0 indicates no fluorescent increase over primary alone.

As it was previously shown for rose bengal and other xanthene dyes,¹³⁴ pulsed primary excitation offers the opportunity to increase k_{bright} , and therefore dark state population, without increasing dark state decay, k_{decay} . This may allow for the use of higher primary intensities and therefore higher overall signal and thus was applied to the blue fluorescent proteins. Using $\sim 100 \text{ ps}$ pulses at 372 nm, the primary excitation only populates dark states within a short time window, allowing the modulated continuous wave (cw) secondary laser to depopulate the dark state over longer periods, without primary laser interference. In fact, switching from cw 405 nm to pulsed 372 nm primary

excitation, each with secondary illumination at 514 nm, increases enhancement to 20% for T203V/S205V and 40% for H148K for similar intensities (Table 4.8).^e As long as primary induced dark state creation is more efficient than dark state decay, such pulsed excitation prepares the dark state with a single pulse, allowing the secondary laser to optically regenerate the emissive state. Characteristic frequencies with pulsed primary excitation should yield longer natural dark state decay times. However, the lifetimes actually decreased with pulsed primary excitation indicating the non-ideal behavior of this system (Table 4.8).

Table 4.8. Mutants of T203V/S205V with the corresponding fluorescence enhancement and characteristic frequency following co-excitation with 372 nm and 515 nm.

Mutation	Enhancement (%)	Characteristic Frequency (Hz)	τ_{bright} (ms)	τ_{decay} (ms)
Wild-type	20	11	357	122
H148D	15	19	212	71
H148G	11	14	434	88
H148K	37	28	115	81
H148R	15	23	179	57
H148Y	5			
V150A	20	24	120	90
F165H	5			
F165L	0	N/A	N/A	N/A

For mKalama1, no fluorescence enhancement was observed with 372 nm primary and 514 nm secondary co-excitation. However, the single point mutation of mKalama1 G149K increased the fluorescence enhancement to 6% with co-excitation. The ground state absorbance spectrum for mKalama1 and its mutant is shown in Figure 4.6. The

^e Data provided by Amy Jablonski

major difference is the appearance of the anion in the G149K mutant. Plotting the fluorescence enhancement vs. modulation frequency of the G149K mutant reveals a characteristic frequency of ~90 Hz (~10 ms).

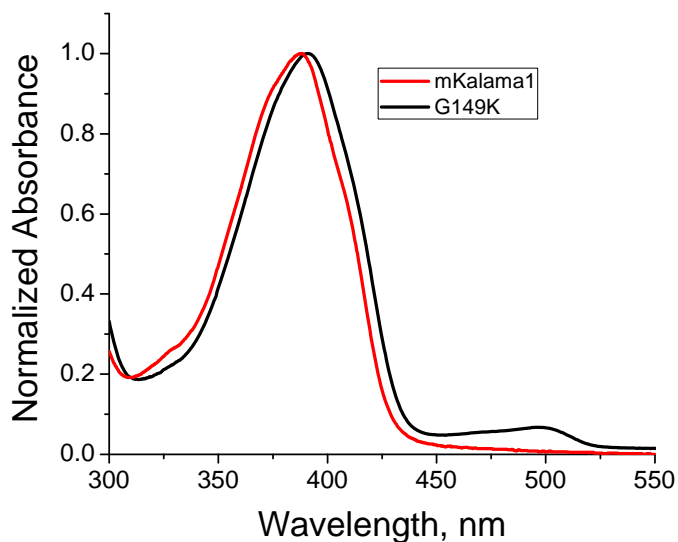


Figure 4.6. Ground state absorption spectra of mKalama1 (red) and mKalama1 G149K (black).

Using 476 nm primary and 561 nm secondary excitation, the green PFP Padron* also exhibited fluorescence enhancement. The characteristic frequencies, as well as on and off times for Padron* and its mutants are shown in Table 4.9.^f

^f Data obtained by Amy Jablonski

Table 4.9. Characteristic frequencies, as well as on and off times for Padron* and its mutants.

Mutation	ν_c @ 3.4 kW/cm²	On Time (ms)	Off Time (ms)
Wild-type	1173	1.74	1.67
H194A	2638	0.45	2.47
H194C	1804	0.8	1.82
H194E	2113	0.62	1.92
H194F	1768	0.69	3.12
H194G	2350	0.67	1.17
H194K	1121	1.28	2.93
H194M	2156	0.57	2.37
H194S	1102	1.57	2.14
H194V	1466	0.98	2.22

TA spectroscopy was employed in order to identify the nature of the dark state(s). The evolution of the TA for GFP T203V/S205V is shown in Figure 4.7. After $\sim 500 \mu\text{s}$, very little decay of the transients is seen; eventually, at longer timescales, an increase is evident. This is likely due to the probe light “modulating” the transient species in the protein. In fact, transient species are generated with only white lamp and no primary excitation. Furthermore, the absorption at 430 nm grows in after $\sim 80 \mu\text{s}$ (Figure 3.17). This same trend is observed for the H148K mutant except that the fast decay at $\sim 500 \text{ nm}$ ($< 80 \mu\text{s}$) is not observed (Figure 4.8).

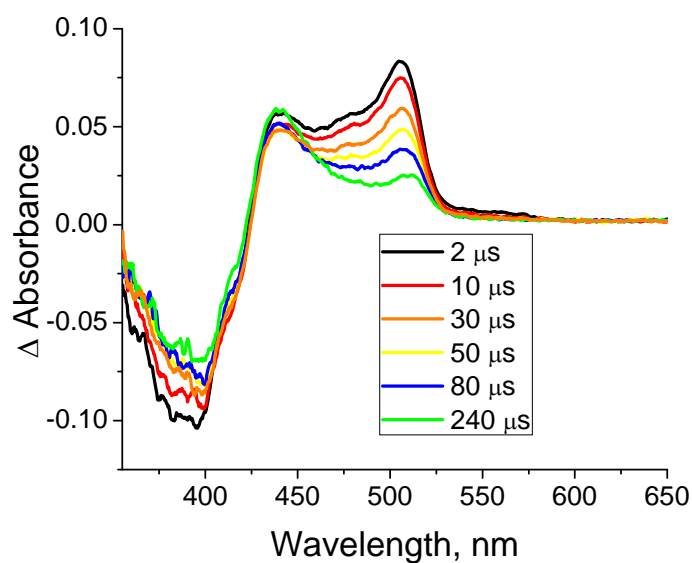


Figure 4.7. TA spectra for T203V/S205V at 2, 10, 30, 50, 80, and 240 μs after excitation with a 355 nm laser.

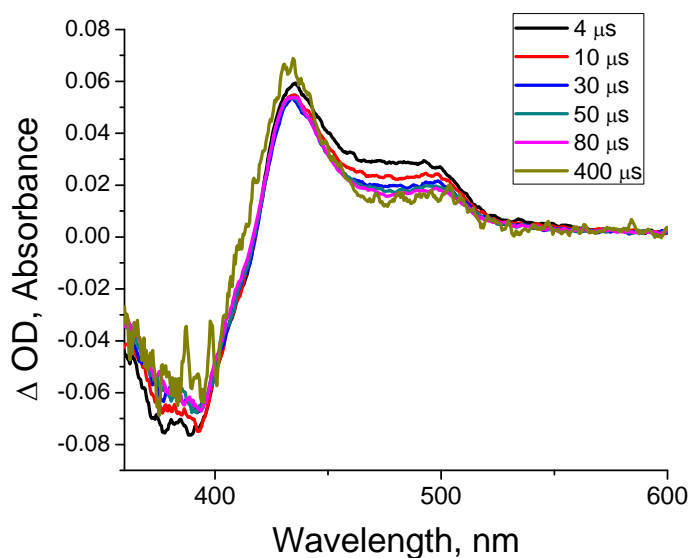


Figure 4.8. TA spectra for H148K at 4, 10, 30, 50, 80, and 400 μs after excitation with a 355 nm laser.

The evolution of the TA varies drastically for mKalama1 and its mutant G149K (Figures 3.1 and 4.9), as the G149K mutant has lost all faster components. It should be

noted that the 1.66 ms time slice has absorption that spans to ~525 nm and resembles anionic absorption (Figure 4.9). Again, the kinetics of the transitions were affected by the probe light as can be seen from the increase of absorption at ~430 nm (Figure 4.9).

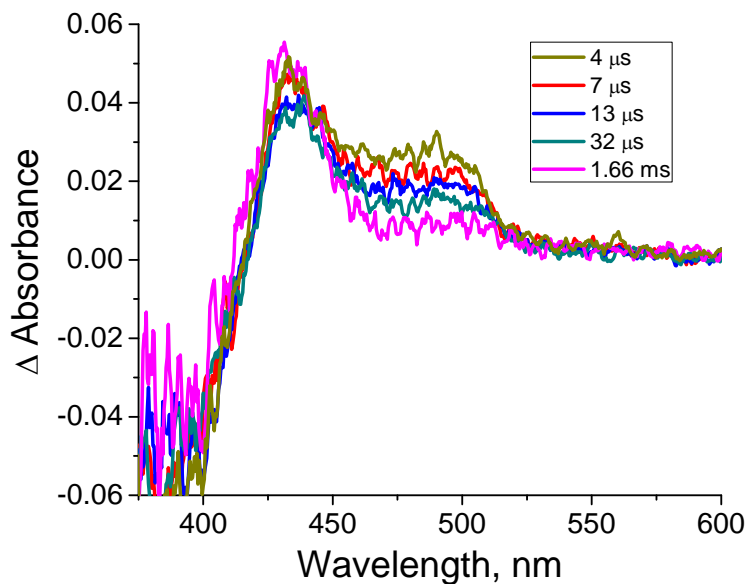


Figure 4.9. TA spectra for mKalama1 G149K at 4, 7, 13, 32, and 1660 μ s after excitation with a 355 nm laser. The kinetics of the transitions are affected by the probe light.

Discussion

Mutating key residues in the chromophore environment for 203V/205V has altered modulation depth and frequency yielding BFPs with greater fluorescence enhancement. The greatest enhancement at long wavelength was observed with the H148K mutant of GFP 203V/205V; therefore, the equivalent site G149 was mutated in the non-modulatable mKalama1. The resulting mKalama1 G149K mutant yielded a 6% fluorescence enhancement confirming the importance of the 148 position. This site is well known for shielding the chromophore from the solvent and mutations to smaller

residues, such as glycine, increase solvent access.^{40,138,139} Mutations to position 148 are also known to affect the conformational flexibility of the β -sheets by disturbing the interstrand hydrogen bonding network.¹³⁹ This added backbone flexibility may affect the chromophore stabilizing network and therefore increase the rate of isomerization.¹³⁹ The F165L mutation of mKalamal virtually turns off fluorescence enhancement. Because this residue is close to the *Z* configuration (Figure 4.10), it is likely to affect the *Z-E* isomerization as well as the protonation state of the chromophore. In Figure 4.10, the *E* state of the chromophore is modeled into the GFP 203V crystal structure. The placement of a more basic side chain in the pocket would likely raise the pK_a of the chromophore in the *E* configuration.

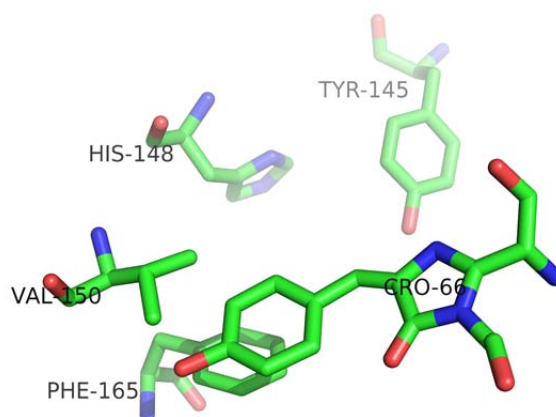


Figure 4.10. The chromophore of GFP T203V (PDB 2QLE) modeled in the *E* configuration with key surrounding residues. Drawn using the PyMOL Molecular Graphics System, Version 1.2r3pre, Schrödinger, LLC.

The TA spectra of mKalamal G149K, T203V/S205V, and H148K are quite similar. The TA of all three proteins contain ground state bleach (~ 390 nm), a band at ~ 430 nm, and a band at ~ 500 nm. Unfortunately, the TA is affected by the probe light. There is also the appearance of the photoproduct, absorbing at ~ 390 nm and ~ 500 nm,

which complicates the kinetics. Although it is difficult to identify the exact nature of the dark state, it is certain that the photophysics of these proteins can vary drastically by one single mutation. mKalamal was well behaved for these types of TA measurements, given that the decay of all transients were observed. However, the single point mutation G149K drastically modified the photophysics and created a mutant capable of modulation based fluorescence enhancement. Although one can speculate on the nature of the dark state, ultimately the whole picture is a bit more complex.

The complexity of the photodynamics in these proteins is further demonstrated by the fluorescence enhancement versus primary excitation intensity. It would be expected that at higher primary excitation intensities, more dark state population would be generated which could, in turn, be depopulated with the secondary laser to yield greater enhancement. However, the opposite trend is observed for these proteins, likely because the dark state absorption competes with the secondary excitation to independently depopulate the same dark state. It was previously demonstrated that depopulation of the triplet state in rose bengal led to fluorescence enhancement.¹³⁴ Similar to the BFPs, the rose bengal triplet state absorption of primary excitation competes with that of the secondary excitation; therefore, at higher primary intensities, little to no fluorescence enhancement is observed because the primary excitation intensity is neutralizing gains by off-time shortening. This was solved by using pulsed primary excitation whereby the long time interval between pulses allowed the secondary laser to independently depopulate the triplet state and resulted in large fluorescence enhancement. When pulsed primary excitation was applied to the fluorescent proteins, larger enhancements were, in

fact, observed. However, increasing primary intensities still decreased overall fluorescence enhancement.

Conclusions

Blue fluorescent protein utility in fluorescence microscopy remains somewhat limited in cellular imaging due to weak fluorescence, poor photostability, and high background resulting from cellular autofluorescence. Through dual-laser fluorescence modulation this problem has been circumvented by allowing depopulation of dark states thereby increasing the overall fluorescence. The dark state depopulation occurs at wavelengths longer than the collected fluorescence, preventing an increase in background fluorescence and allowing for better signal discrimination.

Mutations of residues in the vicinity of the chromophore have altered the photophysics and allowed for variants with improved fluorescence enhancement over the wild-type. The mutant H148K yielded the greatest fluorescence enhancement out of all T203V/S205V mutants. Given the structural analysis, TA results, previously published results, and dark state lifetimes the most reasonable explanation for the modulation based enhancement is the *Z-E* isomerization of the chromophore. However, one cannot rule out other photophysical processes. Further research to extend the color palette of modulatable fluorescent proteins to include RFPs would be of significant interest to increase tissue penetration and further avoid cellular autofluorescence.

CHAPTER 5

CONCLUSIONS AND FUTURE WORK

In this dissertation, the photophysics and photochemistry of a variety of fluorescent proteins were investigated. This work focused extensively on these proteins and helped shed light on new mechanisms through a previously unexplored area of fluorescent protein research. The photosensitization mechanism of the phototoxic RFP KillerRed, which is a matter of debate in the scientific community, was investigated through numerous experiments. The results indicate that no $^1\text{O}_2$ was detected by its characteristic phosphorescence at 1278 nm. While it is still possible that small amounts of $^1\text{O}_2$ are formed, it is unlikely to contribute significantly to the phototoxicity. Furthermore, irradiation of KillerRed in the presence of the radical trap TEMPO-9-ac confirmed the production of radicals, supporting a type I photosensitization mechanism. Not surprisingly, radical production in KillerRed was oxygen dependent since far less radicals were generated in a deoxygenated sample. Interestingly, DsRed, which has the same chromophore as KillerRed, was previously found to be non-phototoxic. Yet the *in vitro* CALI studies presented herein show that mutations to DsRed, to create mRFP, result in a phototoxic protein. It was also shown that the phototoxicity of mRFP stems from radical production through the probe TEMPO-9-ac.

In order to characterize the radicals produced by KillerRed and mRFP, the spin trap DMPO was used. However, several attempts to trap radicals with this probe failed. Interestingly, excitation of KillerRed, mRFP, and DsRed produced a long-lived carbon

centered radical detected by EPR spectroscopy. For the non-phototoxic DsRed, this is not surprising since the proposed mechanism of decarboxylation invokes radical intermediates.

It is known that superoxide can dismutate to produce H_2O_2 . Therefore, the Amplex® Red reagent was employed for the detection of H_2O_2 . This assay demonstrated that illumination of mRFP and KillerRed produces H_2O_2 which is then consumed by the protein. Surprisingly, H_2O_2 had little to no effect on the ground state absorbance of any of the proteins investigated. These data reveal that these proteins feature a Janus-type feature acting as both an ROS generator and an antioxidant.

The broad-band TA spectroscopy was applied to these proteins to help reveal their photocycles as well as to identify the mechanisms of ROS generation. Although KillerRed and mRFP vary greatly from the non-phototoxic DsRed, a similar transient feature was observed in each of the proteins which spanned from the ~600-1040 nm. This transient was susceptible to quenching with H_2O_2 and O_2 in both mRFP and KillerRed, but not DsRed. The identity of the transient remains elusive; however, radical dianion seems most plausible due to the previously proposed decarboxylation mechanism. However, one cannot ignore other possibilities such as a CT complex or electron ejection leading to radical chromophore/solvated electron formation. TA studies using various quenchers indicate that the tight packing of the β -barrel could play a critical role in the phototoxicity of these proteins. This hypothesis is confirmed by the crystal structure of KillerRed which indicates a long-filled water channel extending from the chromophore to the outside environment. It is hypothesized that this the likely path in which ROS can travel.

Future TA studies on RFPs mutants would be important in identifying the transient species. For example, in the widely accepted decarboxylation mechanism of E222, it is suggested that E222 donates an electron to the chromophore.¹⁶ Therefore, it would be of great interest to generate mutants of this residue to see what effect they may have on the transient/transient lifetime. The E222D mutation would allow for the same electrostatics while providing a shorter chain length; thereby decreasing the distance between it and the chromophore. Additionally, mutations to KillerRed that would block the water channel would be useful to determine the pathway that these ROS travel. Then, through CALI, ROS probes, and TA spectroscopy, the toxicity of these mutants could be evaluated. If the water channel is blocked, then O₂ and H₂O₂ would be less likely to quench the transients if this is the pathway by which small molecules can get in and out of the protein.

The same techniques applied to the RFPs in this work were also applied to the BFP mKalama1 to reveal some interesting, previously unexplored dynamics. Although mKalama1 does not contain anion in the ground state and is incapable of ESPT, it goes through two anionic intermediates which have lifetimes on the μ s timescale. The proton acceptor of these intermediates remains elusive; however, possible acceptors have been identified through analysis of the wtGFP 203V crystal structure which has 89% identity to mKalama1. TA analysis of mutants at these sites should help to uncover the identity of these intermediates. The TA results along with previous published data suggest the formation of a radical cation and solvated electron by two photon excitation. This is the first observation of these species in the GFP family. This radical cation may explain the blinking behavior observed on the single molecule level for numerous fluorescent

proteins. The nature of the 700 μ s oxygen sensitive component still remains elusive; however, the crystal structure of mKalama1 as well as the TA of various mutants will help elucidate the nature of the unidentified species. Work is currently in progress to acquire the TA for various mutants.

The identification of the dark states in mKalama1 and other BFPs has helped pave the way to improving these proteins for cellular imaging. These data demonstrate that optical depopulation of such dark states can yield fluorescence gains. This fluorescence enhancement arises from establishing a steady state dark population with the primary laser, coupled with rapid depopulation with the secondary laser. The secondary laser was lower in energy than the collected fluorescence in order to avoid increasing background fluorescence. Several mutations, to the BFPs T203V/T205V and mKalama1 were made to increase fluorescence enhancement. The best performing mutant of T203V/S205V was H148K with a 37% fluorescence enhancement. While fluorescence enhancement of mKalama1 could not be achieved with dual lasers, the single mutation G149K (148 in wtGFP) resulted in a 4% fluorescence enhancement, again revealing the importance of the 148 position. Dark states were observed in the TA close to the 515 nm secondary wavelength. However, the decay was complicated by secondary white light excitation and photoproduct formation. The importance of position 148 (149 in mKalama1) on the photophysics is realized through these experiments. Mutation of this position is known to alter the solvent accessibility to the chromophore and also might affect isomerization efficiency. Work is in progress to expand this dual wavelength fluorescence enhancement to RFPs to achieve better tissue penetration depth and separation from autofluorescence.

This previously unexplored arena holds great promise for future development and understanding of fluorescent proteins.

APPENDIX A

DNA AND AMINO ACID SEQUENCES

Table A.1. Amino acid sequences of KillerRed, mRFP, and DsRed each containing a polylinker and a 6xHN affinity tag. The 6xHN affinity tag and polylinker are underlined. The three residues which make up the chromophore are highlighted in red.

Protein	Amino Acid Sequence
KillerRed	<u>GHNHNHNHNHNHNGDDDDKVV</u> MEGGPALFQSDMTFKIFIDGEV NGQKFTIVADGSSKFPHGDFNVHAVCETGKLPMSWKPICHLI QYGE PF FARYPDGISHFAQECPPEGLSIDRTVRFENDGTMTSHHTYELDDTCVVS ITVNCDFGQPDGPIMRDQLVDILPNETHMFPHPGNAVRQLAFIGFTTAD GGLMMGHFDSKMTFNQSRRAIEIPGPHFVTIITKQMRDTSDKRDHVCQR EVAYAHSVPRITSAIGSDED
mRFP	<u>GHNHNHNHNHNHNGDDDDKVV</u> MASSEDVIKEFMRFKVRMEGS VNGHEFEIEGEGEGRPYEGTQTAKLKVTKGGPLPFAWDILSPQF QYGS K AYVKHPADIPDYKLSFPEGFKWERVMNFEDGGVVTVTQDSSLQDGEF IYKVKLRGTNFPDGPVMQKKTMGWEASTERMYPEDGALKGEIKMRL KLDGGHYDAEVKTTYMAKKPVQLPGAYKTDIKLDITSHNEDYTIVEQ YERAEGRHSTGA
DsRed	<u>GHNHNHNHNHNHNGDDDDKVV</u> MASSENVITEFMRFKVRMEGT VNGHEFEIEGEGEGRPYEGHNTVKKLVTKGGPLPFAWDILSPQF QYGS K VYVKHPADIPDYKLSFPEGFKWERVMNFEDGGVATVTQDSSLQDGC FIYKVKFIGVNFSDGPVMQKKTMGWEASTERLYPRDGVKGETHKAL KLDGGHYLVEFKSIYMAKKPVQLPGYYYVDAKLDITSHNEDYTIVEQ YERTEGRHHLFL

Table A.2. The DNA sequence of the KillerRed gene inserted between *Sall* and *NotI* restriction sites in Pprotet.

Number	Nucleotide Sequence
1	ATGGAAGGGG GTCCGGCGCT GTTCCAGTCG GACATGACTT TCAAGATTTT
51	CATCGACGGC GAGGTCAATG GCCAGAAATT CACCATCGTG GCCGACGGGT
101	CCAGCAAATT TCCGCACGGA GACTTTAATG TGCATGCGGT CTGCGAAACC
151	GGCAAACCTGC CGATGAGCTG GAAACCGATT TGCCATCTGA TTCAGTATGG
201	CGAACCGTTT TTTGCTCGTT ATCCGGACGG CATTAGCCAT TTTGCGCAGG
251	AATGCTTCCC GGAAGGCCTG TCCATAGACC GTACCGTGCG TTTTGAAAAT
301	GACGGCACCA TGACAAGCCA CCATACCTAT GAACTGGATG ATACTTGCGT
351	GGTGAGCCGT ATTACCGTAA ATTGCGATGG CTTTCAGCCA GACGGCCCAA
401	TTATGCGTGA CCAGCTGGTG GACATTCTGC CGAATGAAAC CCATATGTTC
451	CCGCATGGCC CGAATGCGGT GCGTCAGCTG GCGTTTATTG GCTTTACTAC
501	CGCGGATGGC GGCCTGATGA TGGGGCATT TCGACAGCAAG ATGACCTTCA
551	ACGGCTCCCG TGCATTGAG ATACCCGGTC CGCACTTCGT AACCATTATC
601	ACCAAACAGA TGCGCGACAC GAGCGACAAG CGTGATCATG TGTGTCAACG
651	CGAAGTGGCA TACGCTCATA GCGTGCCTCG CATTACCAGC GCAATAGGCT
701	CAGACGAAGA T

Table A.3. Amino acid sequences containing polylinker and hexahistidine tag (underlined/bolded) for mKalama1 and GFP F99S/M153T/V163A/T203V/S205V. The three residues which make up the chromophore are highlighted in blue.

Protein	Amino Acid Sequence
mKalama1	<u>SHHHHHHGMASMTGGQQMGRDLYENLYFOGSS</u> MVSKGEELFTGV VPILVEMDGDVNGRKFSVRGVGEGDATHGKLTLLKFICTSGKLPVWPWT LVTTLSYGVQCFSRYPDHMKQHDFFKSAMPEGYVQERTIFFKDDGSYK TRAEVKFEGDTLVNRIVLKGTDFKEDGNILGHKLEYNMNVGNVYITAD KQKNGIKANFEIRHNVEDGGVQLADHYQQNTPIGDGSVLLPDNHYSV QVKLSKXPNEKRDHMLLEFRTAAGITPGMDELYK
T203V/S205V/F99S/ M153T/V163A	<u>SHHHHHHGS</u> MVSKGEELFTGVVPILVELDGDVNGHKFSVSGEGDAT YGKLTLLKFICTTGKLPVWPWTLVTTFSYGVQCFSRYPDHMKRHDFKS AMPEGYVQERTISFKDDGNYKTRAEVKFEGDTLVNRIELKIDFKEDGN ILGHKLEYNYNVYITADKQKNGIKANFKIRHNIEDGSVQLADHYQ QNTPIGDGPVLLPDNHYSVQVALSKDPNEKRDHMLLEFVTAAGITH GMDELYK

Table A.4. Amino acid sequences containing polylinker and hexahistidine tag (underlined/bolded) for EGFP and Padron*. The three residues which make up the chromophore are highlighted in green.

Protein	Amino Acid Sequence
Padron*	<u>SHHHHHHTDP</u> MMSVIK PDMKIKLRMEGAVNGHPFAIEGVGLGKPFEGK QSMDLKVKEGGPLPFA YDILTMAF CYGN RVFAKYPENIVDYFKQSFPE GYSWERSMHYEDGGSCNATNDITLDGDCYIYEIRFDGVNFPANGPVMQ KRTVKWERSTEKLYVRDGVLSKSDGN YALSLEGGGHYRCDFKTTYKAK KVVQLPDYHSVDHHIEIKSHDKDYSNVNLHEHAEAHSELPRQA
EGFP	<u>GHNHNHNHNHNHNGDDDDKVV</u> D MASKGEELFTGVVPILVELDGD VNGHKFSVSGEGEGDATY GKLTLKFICTTGKLPVPWPTLVTTL CYGV VQ CFSRYPDHMKRHDFFKSAMPEGYVQERTIFFKDDGNYKTRAEVKFEF DTLVNRIELK GIDFKEDGNILGHKLEYNYN SHNVYIMADKQKNGIKVN FKTRHNIEDGSVQLADHYQQNTPIGDGPVLLPDNHYLSTQSALS KDPNE KRDHMLLEFVTAAGITHGMDELYN

Table A.5. The DNA sequence of the mKalamal Gene inserted between *Xho*I and *Eco*RI restriction sites in pBad-HisB.

Number	Nucleotide Sequence
1	ATGGTGAGCA AGGGCGAGGA GCTGTTACCC GGGGTGGTGC CCATCCTGGT
51	CGAGATGGAC GGCGACGTAA ACGGCCGCAA GTTCAGCGTG CGCGGCGTGG
101	GCGAGGGTGA TGCCACCCAC GGCAAGCTGA CCCTGAAGTT CATCTGCACC
151	TCCGGCAAGC TGCCCGTGCC CTGGCCTACC CTCGTGACCA CCCTGTCTTA
201	CGGCGTGCAG TGCTTCTCCC GCTACCCCGA CCACATGAAG CAGCACGACT
251	TCTTCAAGTC CGCCATGCCC GAAGGCTACG TCCAGGAGCG CACCATCTTC
301	TTCAAGGACG ACGGCAGCTA CAAGACCCGC GCCGAGGTGA AGTTCGAGGG
351	CGACACCCTG GTGAACCGCA TCGTGCTGAA GGCACCGAC TTCAAGGAGG
401	ACGGTAACAT CCTGGGGCAC AAGCTGGAGT ACAACATGAA CGTCGGGAAC
451	GTCTATATCA CGGCCGACAA GCAGAAGAAC GGCATCAAAG CGAACTTCGA
501	GATCAGGCAC AACGTCGAGG ACGGCGGCGT GCAGCTCGCC GACCACTACC
551	AGCAGAACAC CCCCATCGGC GACGGCTCCG TGCTGCTGCC CGACAACCAC
601	TACCTGAGCG TGCAGGTGAA GCTGAGCAAA GANCCCAACG AGAAGCGCGA
651	TCACATGGTC CTGCTGGAGT TCCGCACCCG CGCCGGGATC ACTCCCGGCA
701	TGGACGAGCT GTACAAG

Table A.6. The DNA sequence of the 203V/205V gene inserted between *Bam*HI and *Hind*III restriction sites in PQE-30.

Number	Nucleotide Sequence				
1	ATGAGTAAAG	GAGAAGAAGT	TTTCACTGGA	GTTGTCCCAA	TTCTTGTTGA
51	ATTAGATGGT	GATGTTAATG	GGCACAAATT	TTCTGTCAGT	GGAGAGGGTG
101	AAGGTGATGC	AACATACGGA	AAACTTACCC	TTAAATTTAT	TTGCACTACT
151	GGAAAAC TAC	CTGTTCCATG	GCCAACACTT	GTCAC TACTT	TCTCTTATGG
201	TGTTCAATGC	TTTTCAAGAT	ACCCAGATCA	TATGAAACGG	CATGACTTTT
251	TCAAGAGTGC	CATGCCCGAA	GGTTATGTAC	AGGAAAGAAC	TATAAGCTTC
301	AAAGATGACG	GGAAC TACAA	GACACGTGCT	GAAGTCAAGT	TTGAAGGTGA
351	TACCCTTGTT	AATAGAATCG	AGTTAAAAGG	TATTGATTTT	AAAGAAGATG
401	GAAACATTCT	TGGACACAAA	TTGGAATACA	ACTATAACTC	ACACAATGTA
451	TACATCACCG	CAGACAAACA	AAAGAATGGA	ATCAAAGCGA	ACTTCAAAAT
501	TAGACACAAC	ATTGAAGATG	GAAGCGTTCA	ACTAGCAGAC	CATTATCAAC
551	AAAATACTCC	AATTGGCGAT	GGCCCTGTCC	TTTTACCAGA	CAACCATTAC
601	CTGTCCGTAC	AAGTCGCCCT	CTCAAAAGAT	CCCAACGAAA	AGAGAGACCA
651	CATGGTCCTT	CTTGAGTTTG	TAACAGCTGC	TGGGATTACA	CATGGCATGG
701	ATGAACTATA	CAAA			

Table A.7. The DNA sequence of the Padron* gene inserted between *Bam*HI and *Hind*III restriction sites in PQE-31.

Number	Nucleotide Sequence				
1	ATGAGTGTGA	TTAAACCAGA	CATGAAGATC	AAGCTGCGTA	TGGAAGGCGC
51	TGTAATGGA	CACCCGTTTCG	CGATTGAAGG	AGTTGGCCTT	GGGAAGCCTT
101	TCGAGGGAAA	ACAGAGTATG	GACCTTAAAG	TCAAAGAAGG	CGGACCTCTG
151	CCTTTCGCCT	ATGACATCTT	GACAAATGGCG	TTCTGTTACG	GCAACAGGGT
201	ATTCGCCAAA	TACCCAGAAA	ATATAGTAGA	CTATTTCAAG	CAGTCGTTTC
251	CTGAGGGCTA	CTCTTGGGAG	CGAAGCATGC	ATTACGAAGA	CGGGGGCTCA
301	TGTAACGCGA	CAAACGACAT	AACCCTGGAT	GGTGACTGTT	ATATCTATGA
351	AATTCGATTT	GATGGCGTGA	ACTTTCCTGC	CAATGGTCCA	GTTATGCAGA
401	AGAGGACTGT	GAAATGGGAG	CGGTCCACTG	AGAAATTGTA	TGTGCGTGAT
451	GGAGTGCTGA	AGTCTGATGG	TAACTACGCT	CTGTGCTTGG	AAGGAGGTGG
501	CCATTACCGA	TGTGACTTCA	AAACTACTTA	TAAAGCTAAG	AAGGTTGTCC
551	AGTTGCCAGA	CTATCACTCT	GTGGACCACC	ACATTGAGAT	TAAAAGCCAC
601	GACAAAGATT	ACAGTAATGT	TAATCTGCAT	GAGCATGCCG	AAGCGCATTC
651	TGAGCTGCCG	AGGCAGGCCA	AC		

APPENDIX B

ABSORPTION SPECTRA OF BLUE FLUORESCENT PROTEINS

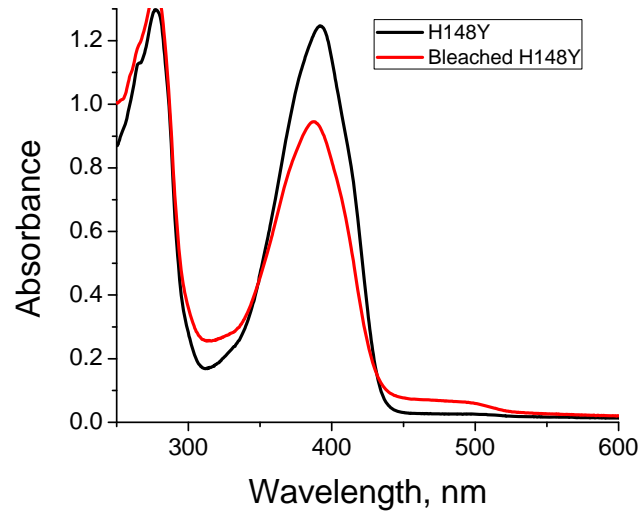


Figure B.1. Absorption spectra of the H148Y mutant of T203V/S205V for native sample (black) and partially bleached sampled (red).

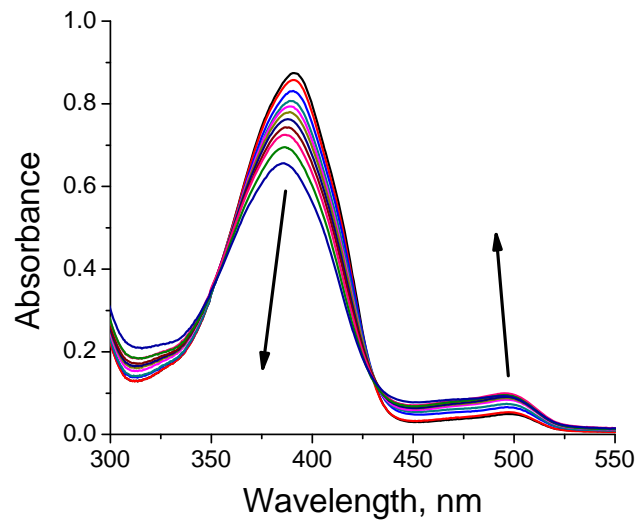


Figure B.2. Absorption spectra of the H148K mutant of T203V/S205V at various irradiation times. The neutral absorption decreased while the anionic absorption increased.

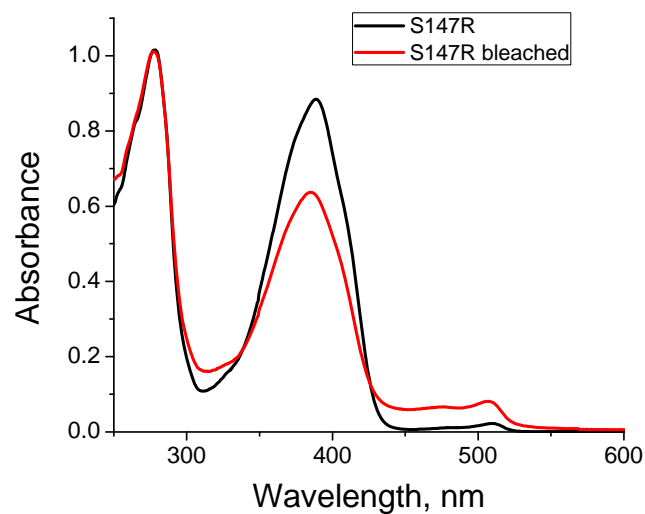


Figure B.3. Absorption spectra of the S147R mutant of T203V/S205V for native sample (black) and partially bleached sampled (red).

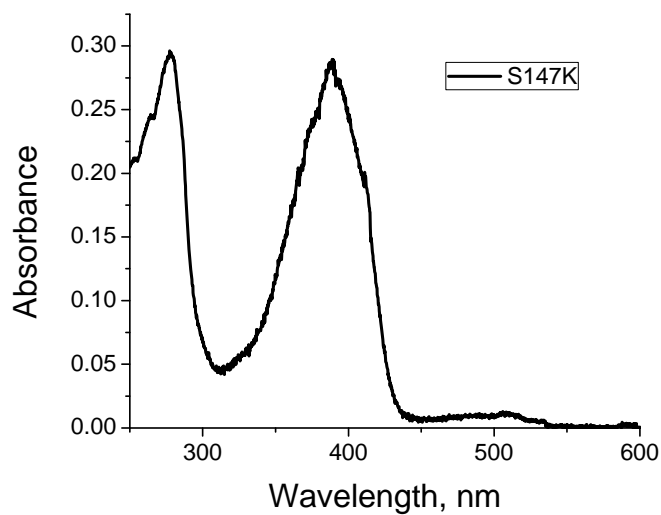


Figure B.4. Absorption spectrum of the S147K mutant of T203V/S205V.

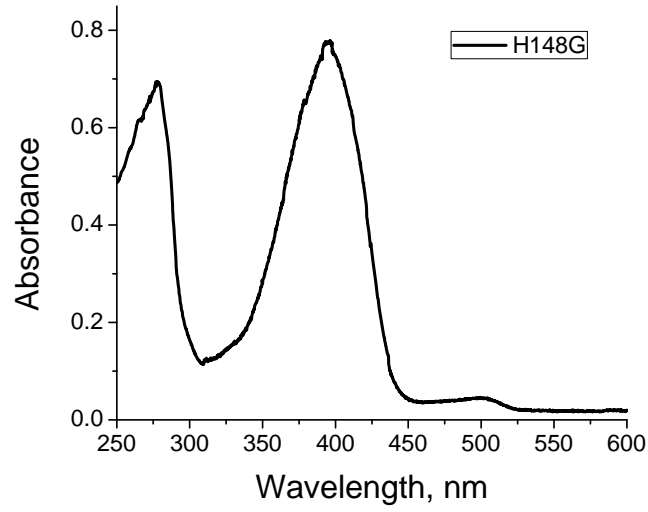


Figure B.5. Absorption spectrum of the H148G mutant of T203V/S205V.

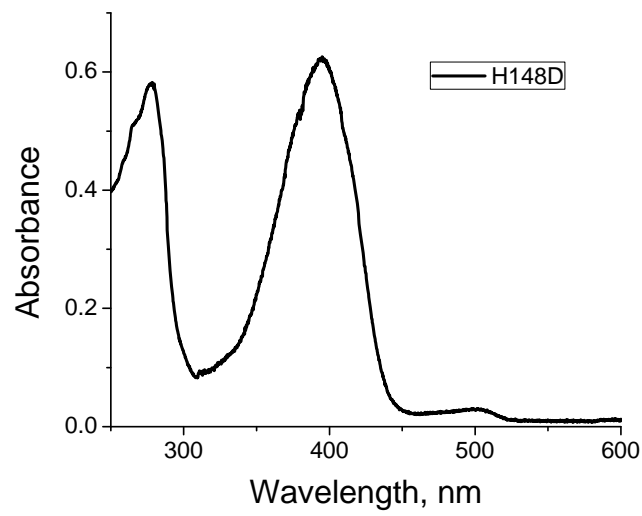


Figure B.6. Absorption spectrum of the H148D mutant of T203V/S205V.

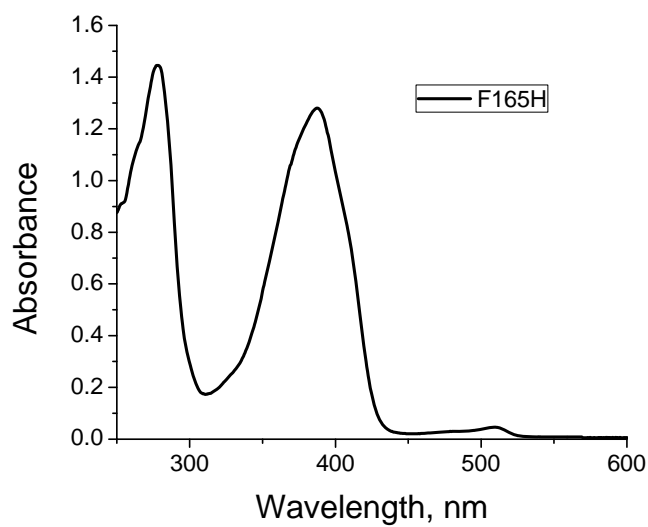


Figure B.7. Absorption spectrum of the F165H mutant of T203V/S205V.

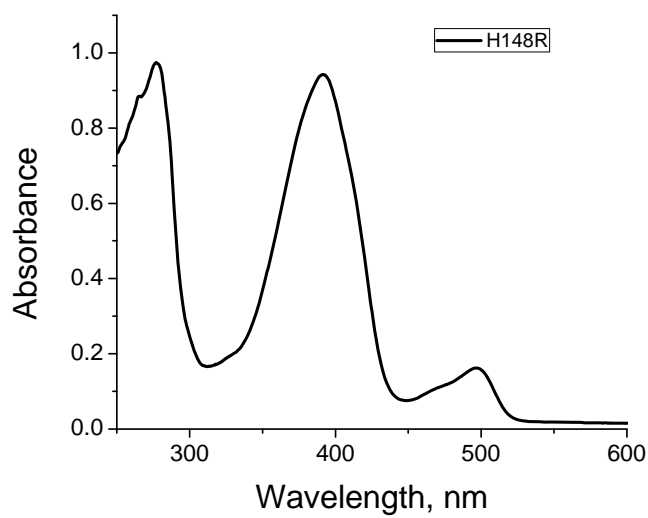


Figure B.8. Absorption spectrum of the H148R mutant of T203V/S205V.

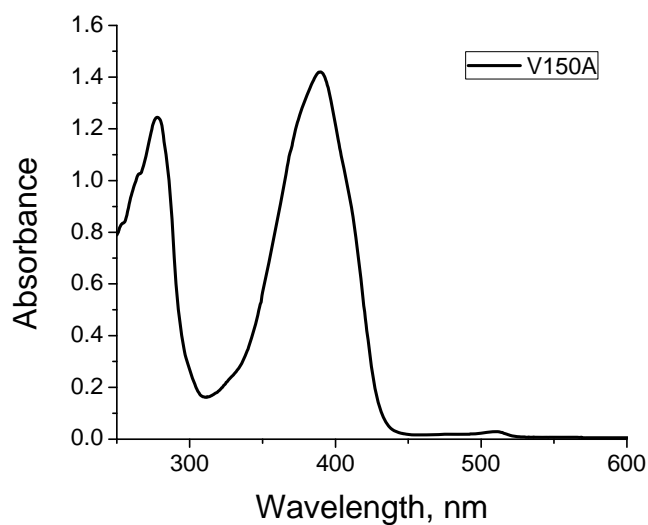


Figure B.9. Absorption spectrum of the V150A mutant of T203V/S205V.

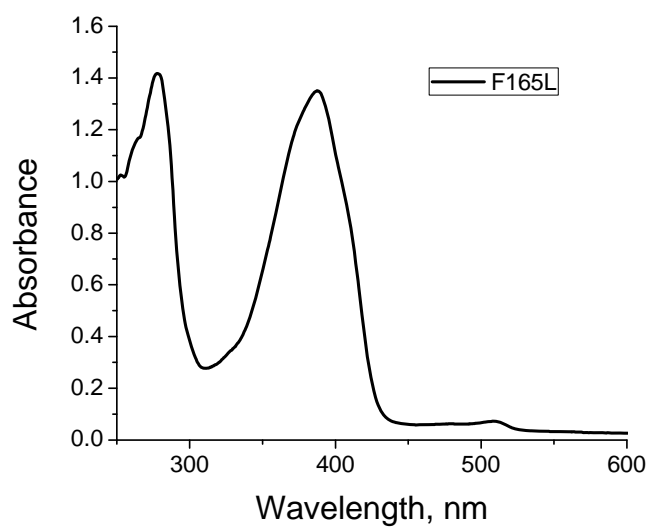


Figure B.10. Absorption spectrum of the F165L mutant of T203V/S205V.

REFERENCES

- (1) Davenport, D.; Nicol, J. A. C. *Proceedings of the Royal Society of London Series B-Biological Sciences* **1955**, *144*, 399.
- (2) Shimomura, O.; Johnson, F. H.; Saiga, Y. *Journal of Cellular and Comparative Physiology* **1962**, *59*, 223.
- (3) Shimomura, O.; Johnson, F. H. *Proceedings of the National Academy of Sciences* **1978**, *75*, 2611.
- (4) Ohmiya, Y.; Hirano, T. *Chemistry and Biology* **1996**, *3*, 337.
- (5) Ormo, M.; Cubitt, A. B.; Kallio, K.; Gross, L. A.; Tsien, R. Y.; Remington, S. J. *Science* **1996**, *273*, 1392.
- (6) Yang, F.; Moss, L. G.; Phillips, G. N. *Nature Biotechnology* **1996**, *14*, 1246.
- (7) Zhang, L.; Patel, H. N.; Lappe, J. W.; Wachter, R. M. *Journal of the American Chemical Society* **2006**, *128*, 4766.
- (8) Heim, R.; Prasher, D. C.; Tsien, R. Y. *Proceedings of the National Academy of Sciences of the United States of America* **1994**, *91*, 12501.
- (9) Barondeau, D. P.; Putnam, C. D.; Kassmann, C. J.; Tainer, J. A.; Getzoff, E. D. *Proceedings of the National Academy of Sciences of the United States of America* **2003**, *100*, 12111.
- (10) Wood, T. I.; Barondeau, D. P.; Hitomi, C.; Kassmann, C. J.; Tainer, J. A.; Getzoff, E. D. *Biochemistry* **2005**, *44*, 16211.
- (11) Kojima, S.; Ohkawa, H.; Hirano, T.; Maki, S.; Niwa, H.; Ohashi, M.; Inouye, S.; Tsuji, F. I. *Tetrahedron Letters* **1998**, *39*, 5239.
- (12) Tsien, R. Y. *Annual Review of Biochemistry* **1998**, *67*, 509.

- (13) van Thor, J. J.; Gensch, T.; Hellingwerf, K. J.; Johnson, L. N. *Nature Structural Biology* **2002**, *9*, 37.
- (14) Habuchi, S.; Cotlet, M.; Gensch, T.; Bednarz, T.; Haber-Pohlmeier, S.; Rozenski, J.; Dirix, G.; Michiels, J.; Vanderleyden, J.; Heberle, J.; De Schryver, F. C.; Hofkens, J. *Journal of the American Chemical Society* **2005**, *127*, 8977.
- (15) Barondeau, D. P.; Kassmann, C. J.; Tainer, J. A.; Getzoff, E. D. *Journal of the American Chemical Society* **2006**, *128*, 4685.
- (16) Bell, A. F.; Stoner-Ma, D.; Wachter, R. M.; Tonge, P. J. *Journal of the American Chemical Society* **2003**, *125*, 6919.
- (17) Greenbaum, L.; Rothmann, C.; Lavie, R.; Malik, Z. *Biological Chemistry* **2000**, *381*, 1251.
- (18) Remington, S. J. *Current Opinion in Structural Biology* **2006**, *16*, 714.
- (19) Jimenez-Banzo, A.; Nonell, S.; Hofkens, J.; Flors, C. *Biophysical Journal* **2008**, *94*, 168.
- (20) Vegh, R. B.; Solntsev, K. M.; Kuimova, M. K.; Cho, S.; Liang, Y.; Loo, B. L. W.; Tolbert, L. M.; Bommarius, A. S. *Chemical Communications* **2011**, *47*, 4887.
- (21) Bulina, M. E.; Chudakov, D. M.; Britanova, O. V.; Yanushevich, Y. G.; Staroverov, D. B.; Chepurnykh, T. V.; Merzlyak, E. M.; Shkrob, M. A.; Lukyanov, S.; Lukyanov, K. A. *Nature Biotechnology* **2006**, *24*, 95.
- (22) Bulina, M. E.; Lukyanov, K. A.; Britanova, O. V.; Onichtchouk, D.; Lukyanov, S.; Chudakov, D. M. *Nature Protocols* **2006**, *1*, 947.
- (23) Lukyanov, K. A.; Serebrovskaya, E. O.; Lukyanov, S.; Chudakov, D. M. *Photochemical & Photobiological Sciences* **2010**, *9*, 1301.
- (24) Vitriol, E. A.; Uetrecht, A. C.; Shen, F. M.; Jacobson, K.; Bear, J. E. *Proceedings of the National Academy of Sciences of the United States of America* **2007**, *104*, 6702.

- (25) Shirmanova, M. V.; Serebrovskaya, E. O.; Lukyanov, K. A.; Snopova, L. B.; Sirotkina, M. A.; Prodanetz, N. N.; Bugrova, M. L.; Minakova, E. A.; Turchin, I. V.; Kamensky, V. A.; Lukyanov, S. A.; Zagaynova, E. V. *Journal of Biophotonics* **2012**.
- (26) Liu, X.; Liu, X.; Zhou, Y.; Zou, D.; Shi, R.; Li, Z.; Zheng, D. *Analytical Biochemistry* **2010**, *405*, 272.
- (27) Waldemar Waldeck, G. M., Manfred Wiessler, Katalin Tóth, Klaus Braun *International Journal of Medical Sciences* **2011**, *8*, 97.
- (28) Serebrovskaya, E. O.; Gorodnicheva, T. V.; Ermakova, G. V.; Solovieva, E. A.; Sharonov, G. V.; Zagaynova, E. V.; Chudakov, D. M.; Lukyanov, S.; Zarsisky, A. G.; Lukyanov, K. A. *Biochemistry* **2011**, *435*, 65-71
- (29) Ai, H. W.; Shaner, N. C.; Cheng, Z. H.; Tsien, R. Y.; Campbell, R. E. *Biochemistry* **2007**, *46*, 5904.
- (30) Wang, L.; Xie, J.; Deniz, A. A.; Schultz, P. G. *The Journal of Organic Chemistry* **2002**, *68*, 174.
- (31) Chen, W.; Sun, Z.; Wang, X.; Jiang, T.; Huang, Z.; Fang, D.; Zhang, D. *Journal of the American Chemical Society* **2012**, *134*, 9589.
- (32) Wachter, R. M.; Elsliger, M. A.; Kallio, K.; Hanson, G. T.; Remington, S. J. *Structure with Folding & Design* **1998**, *6*, 1267.
- (33) Andresen, M.; Stiel, A. C.; Folling, J.; Wenzel, D.; Schonle, A.; Egner, A.; Eggeling, C.; Hell, S. W.; Jakobs, S. *Nature Biotechnology* **2008**, *26*, 1035.
- (34) Shu, X.; Leiderman, P.; Gepshtein, R.; Smith, N. R.; Kallio, K.; Huppert, D.; Remington, S. J. *Protein Science* **2007**, *16*, 2703.
- (35) Wall, M. A.; Socolich, M.; Ranganathan, R. *Nature Structural Biology* **2000**, *7*, 1133.
- (36) Shaner, N. C.; Campbell, R. E.; Steinbach, P. A.; Giepmans, B. N. G.; Palmer, A. E.; Tsien, R. Y. *Nature Biotechnology* **2004**, *22*, 1567.

- (37) Shu, X.; Shaner, N. C.; Yarbrough, C. A.; Tsien, R. Y.; Remington, S. J. *Biochemistry* **2006**, *45*, 9639.
- (38) Kneen, M.; Farinas, J.; Li, Y.; Verkman, A. S. *Biophysical Journal* **1998**, *74*, 1591.
- (39) Souslova, E. A.; Belousov, V. V.; Lock, J. G.; Stromblad, S.; Kasparov, S.; Bolshakov, A. P.; Pinelis, V. G.; Labas, Y. A.; Lukyanov, S.; Mayr, L. M.; Chudakov, D. M. *BMC Biotechnology* **2007**, *7*, 37.
- (40) Barondeau, D. P.; Kassmann, C. J.; Tainer, J. A.; Getzoff, E. D. *Journal of the American Chemical Society* **2002**, *124*, 3522.
- (41) Belousov, V. V.; Fradkov, A. F.; Lukyanov, K. A.; Staroverov, D. B.; Shakhbazov, K. S.; Terskikh, A. V.; Lukyanov, S. *Nature Methods* **2006**, *3*, 281.
- (42) McLean, M. A.; Rajfur, Z.; Chen, Z. Z.; Humphrey, D.; Yang, B.; Sligar, S. G.; Jacobson, K. *Analytical Chemistry* **2009**, *81*, 1755.
- (43) Chalfie, M.; Tu, Y.; Euskirchen, G.; Ward, W.; Prasher, D. *Science* **1994**, *263*, 802.
- (44) Abbe, E. *Archiv für Mikroskopische Anatomie* **1873**, *9*, 413.
- (45) Lippincott-Schwartz, J.; Patterson, G. H. *Trends in Cell Biology* **2009**, *19*, 555.
- (46) Dedecker, P.; Hotta, J.; Ando, R.; Miyawaki, A.; Engelborghs, Y.; Hofkens, J. *Biophysical Journal* **2006**, *91*, L45.
- (47) Habuchi, S.; Ando, R.; Dedecker, P.; Verheijen, W.; Mizuno, H.; Miyawaki, A.; Hofkens, J. *Proceedings of the National Academy of Sciences of the United States of America* **2005**, *102*, 9511.
- (48) Faro, A. R.; Carpentier, P.; Jonasson, G.; Pompidor, G.; Arcizett, D.; Demachy, I.; Bourgeois, D. *Journal of the American Chemical Society* **2011**, *133*, 16362.
- (49) Chudakov, D. M.; Verkhusha, V. V.; Staroverov, D. B.; Souslova, E. A.; Lukyanov, S.; Lukyanov, K. A. *Nature Biotechnology* **2004**, *22*, 1435.

- (50) Andresen, M.; Wahl, M. C.; Stiel, A. C.; Grater, F.; Schafer, L. V.; Trowitzsch, S.; Weber, G.; Eggeling, C.; Grubmuller, H.; Hell, S. W.; Jakobs, S. *Proceedings of the National Academy of Sciences of the United States of America* **2005**, *102*, 13070.
- (51) Andresen, M.; Stiel, A. C.; Trowitzsch, S.; Weber, G.; Eggeling, C.; Wahl, M. C.; Hell, S. W.; Jakobs, S. *Proceedings of the National Academy of Sciences of the United States of America* **2007**, *104*, 13005.
- (52) Lukyanov, K. A.; Chudakov, D. M.; Lukyanov, S.; Verkhusha, V. V. *Nature Reviews Molecular Cell Biology* **2005**, *6*, 885.
- (53) Betzig, E.; Patterson, G. H.; Sougrat, R.; Lindwasser, O. W.; Olenych, S.; Bonifacino, J. S.; Davidson, M. W.; Lippincott-Schwartz, J.; Hess, H. F. *Science* **2006**, *313*, 1642.
- (54) Hess, S. T.; Girirajan, T. P. K.; Mason, M. D. *Biophysical Journal* **2006**, *91*, 4258.
- (55) Lecoq, J.; Schnitzer, M. J. *Nature Biotechnology* **2011**, *29*, 715.
- (56) Campbell, R. E.; Tour, O.; Palmer, A. E.; Steinbach, P. A.; Baird, G. S.; Zacharias, D. A.; Tsien, R. Y. *Proceedings of the National Academy of Sciences of the United States of America* **2002**, *99*, 7877.
- (57) Fradkov, A. F.; Chen, Y.; Ding, L.; Barsova, E. V.; Matz, M. V.; Lukyanov, S. A. *FEBS Letters* **2000**, *479*, 127.
- (58) Yarbrough, D.; Wachter, R. M.; Kallio, K.; Matz, M. V.; Remington, S. J. *Proceedings of the National Academy of Sciences of the United States of America* **2001**, *98*, 462.
- (59) Larkin, M. A.; Blackshields, G.; Brown, N. P.; Chenna, R.; McGettigan, P. A.; McWilliam, H.; Valentin, F.; Wallace, I. M.; Wilm, A.; Lopez, R.; Thompson, J. D.; Gibson, T. J.; Higgins, D. G. *Bioinformatics* **2007**, *23*, 2947.
- (60) Calin, M. A.; Gruia, M. I.; Herascu, N.; Coman, T. *Photomedicine and Laser Surgery* **2005**, *23*, 405.
- (61) Griffin, B. A.; Adams, S. R.; Tsien, R. Y. *Science* **1998**, *281*, 269.

- (62) Adams, S. R.; Campbell, R. E.; Gross, L. A.; Martin, B. R.; Walkup, G. K.; Yao, Y.; Llopis, J.; Tsien, R. Y. *Journal of the American Chemical Society* **2002**, *124*, 6063.
- (63) Thannickal, V. J.; Fanburg, B. L. *American Journal of Physiology - Lung Cellular and Molecular Physiology* **2000**, *279*, L1005.
- (64) Pletnev, S.; Gurskaya, N. G.; Pletneva, N. V.; Lukyanov, K. A.; Chudakov, D. M.; Martynov, V. I.; Popov, V. O.; Kovalchuk, M. V.; Wlodawer, A.; Dauter, Z.; Pletnev, V. *Journal of Biological Chemistry* **2009**, *284*, 32028.
- (65) Carpentier, P.; Violot, S.; Blanchoin, L.; Bourgeois, D. *FEBS Letters* **2009**, *583*, 2839.
- (66) Adam, V.; Carpentier, P.; Violot, S.; Lelimosin, M.; Darnault, C.; Nienhaus, G. U.; Bourgeois, D. *Journal of the American Chemical Society* **2009**, *131*, 18063.
- (67) Roy, A.; Carpentier, P.; Bourgeois, D.; Field, M. *Photochemical & Photobiological Sciences* **2010**, *9*, 1342.
- (68) Boyle, R. W.; Dolphin, D. *Photochemistry and Photobiology* **1996**, *64*, 469.
- (69) Serebrovskaya, E. O.; Edelweiss, E. F.; Stremovskiy, O. A.; Lukyanov, K. A.; Chudakov, D. M.; Deyev, S. M. *Proceedings of the National Academy of Sciences* **2009**, *106*, 9221.
- (70) Egorov, S. Y.; Kamalov, V. F.; Koroteev, N. I.; Krasnovsky, A. A.; Toleutaev, B. N.; Zinukov, S. V. *Chemical Physics Letters* **1989**, *163*, 421.
- (71) Costa, G. L.; Weiner, M. P. *Cold Spring Harbor Protocols* **2006**, *2006*, 4, S131-S136.
- (72) Belevich, I.; Gorbikova, E.; Belevich, N. P.; Rauhamäki, V.; Wikström, M.; Verkhovsky, M. I. *Proceedings of the National Academy of Sciences* **2010**, *107*, 18469.
- (73) Borisov, V. B.; Belevich, I.; Bloch, D. A.; Mogi, T.; Verkhovsky, M. I. *Biochemistry* **2008**, *47*, 7907.

- (74) Belevich, I.; Bloch, D. A.; Belevich, N.; Wikström, M.; Verkhovsky, M. I. *Proceedings of the National Academy of Sciences* **2007**, *104*, 2685.
- (75) Bloch, D. A.; Jasaitis, A.; Verkhovsky, M. I. *Biophysical Journal* **2009**, *96*, 4733.
- (76) Rakowski, A. *Zeitschrift Fur Physikalische Chemie--Stochiometrie Und Verwandtschaftslehre* **1906**, *57*, 321.
- (77) Bell, R. P. *Journal of Molecular Structure* **1976**, *33*, 173.
- (78) Wilkinson, W.; Helman W. P.; Ross, A. B. *Journal of Physical and Chemical Reference Data* **1995**, *24*, 663.
- (79) Jiménez-Banzo, A.; Ragas, X.; Abbruzzetti, S.; Viappiani, C.; Campanini, B.; Flors, C.; Nonell, S. *Photochemical & Photobiological Sciences* **2010**, *9*(10), 1336-41.
- (80) Miller, H. J.; Cold Spring Harbor Laboratory: Cold Spring Harbor, New York, **1972**, p 352.
- (81) Setsukinai, K.; Urano, Y.; Kakinuma, K.; Majima, H. J.; Nagano, T. *Journal of Biological Chemistry* **2003**, *278*, 3170.
- (82) Rinalducci, S.; Pedersen, J. Z.; Zolla, L. *Biochimica Et Biophysica Acta-Bioenergetics* **2008**, *1777*, 417.
- (83) Sajiki, J.; Masumizu, T. *Chemosphere* **2004**, *57*, 241.
- (84) de Menezes, S. L.; Augusto, O. *Journal of Biological Chemistry* **2001**, *276*, 39879.
- (85) Mottley, C.; Connor, H. D.; Mason, R. P. *Biochemical and Biophysical Research Communications* **1986**, *141*, 622.
- (86) Dikalov, S.; Jiang, J.; Mason, R. P. *Free Radical Research* **2005**, *39*, 825.
- (87) McCord, J. M.; Fridovic, I. *Journal of Biological Chemistry* **1969**, *244*, 6049.

- (88) Benov, L. *Protoplasma* **2001**, 217, 33.
- (89) Manda, G.; Nechifor, M. T.; Neagu, T.-M. *Current Chemical Biology* **2009**, 3, 22.
- (90) Koubek, E.; Haggett, M. L.; Battaglia, C. J.; Ibne-Rasa, K. M.; Pyun, H. Y.; Edwards, J. O. *Journal of the American Chemical Society* **1963**, 85, 2263.
- (91) Stadtman, E. R.; Berlett, B. S. *Chemical Research in Toxicology* **1997**, 10, 485.
- (92) Vengris, M.; van Stokkum, I. H. M.; He, X.; Bell, A. F.; Tonge, P. J.; van Grondelle, R.; Larsen, D. S. *Journal of Physical Chemistry A* **2004**, 108, 4587.
- (93) Solntsev, K. M.; Poizat, O.; Dong, J.; Rehault, J.; Lou, Y. B.; Burda, C.; Tolbert, L. M. *Journal of Physical Chemistry B* **2008**, 112, 2700.
- (94) Forbes, M. W.; Jockusch, R. A. *Journal of the American Chemical Society* **2009**, 131, 17038.
- (95) Bogdanov, A. M.; Mishin, A. S.; Yampolsky, I. V.; Belousov, V. V.; Chudakov, D. M.; Subach, F. V.; Verkhusha, V. V.; Lukyanov, S.; Lukyanov, K. A. *Nature Chemical Biology* **2009**, 5, 459.
- (96) Sniegowski, J. A.; Lappe, J. W.; Patel, H. N.; Huffman, H. A.; Wachter, R. M. *Journal of Biological Chemistry* **2005**, 280, 26248.
- (97) Blazek, E. R.; Peak, M. J. *International Journal of Radiation Biology* **1988**, 53, 237.
- (98) Chatteraj, M.; King, B. A.; Bublitz, G. U.; Boxer, S. G. *Proceedings of the National Academy of Sciences of the United States of America* **1996**, 93, 8362.
- (99) Agmon, N. *Biophysical Journal* **2005**, 88, 2452.
- (100) Bravaya, K. B.; Subach, O. M.; Korovina, N.; Verkhusha, V. V.; Krylov, A. I. *Journal of the American Chemical Society* **2012**, 134, 2807.

- (101) Quercioli, V.; Bosisio, C.; Daglio, S. C.; Rocca, F.; D'Alfonso, L.; Collini, M.; Baldini, G.; Chirico, G.; Bettati, S.; Raboni, S.; Campanini, B. *Journal of Physical Chemistry B* **2010**, *114*, 4664.
- (102) Bosisio, C.; Quercioli, V.; Collini, M.; D'Alfonso, L.; Baldini, G.; Bettati, S.; Campanini, B.; Raboni, S.; Chirico, G. *Journal of Physical Chemistry B* **2008**, *112*, 8806.
- (103) Schwille, P.; Kummer, S.; Heikal, A. A.; Moerner, W. E.; Webb, W. W. *Proceedings of the National Academy of Sciences of the United States of America* **2000**, *97*, 151.
- (104) Haupts, U.; Maiti, S.; Schwille, P.; Webb, W. W. *Proceedings of the National Academy of Sciences of the United States of America* **1998**, *95*, 13573.
- (105) Widengren, J.; Mets, Ü.; Rigler, R. *Chemical Physics* **1999**, *250*, 171.
- (106) Bizzarri, R.; Nifosi, R.; Abbruzzetti, S.; Rocchia, W.; Guidi, S.; Arosio, D.; Garau, G.; Campanini, B.; Grandi, E.; Ricci, F.; Viappiani, C.; Beltram, F. *Biochemistry* **2007**, *46*, 5494.
- (107) Abbruzzetti, S.; Grandi, E.; Viappiani, C.; Bologna, S.; Campanini, B.; Raboni, S.; Bettati, S.; Mozzarelli, A. *Journal of the American Chemical Society* **2005**, *127*, 626.
- (108) Jung, G.; Wiehler, J.; Zumbusch, A. *Biophysical Journal* **2005**, *88*, 1932.
- (109) Rusanov, A. L.; Mironov, V. A.; Goryashenko, A. S.; Grigorenko, B. L.; Nemukhin, A. V.; Savitsky, A. P. *Journal of Physical Chemistry B* **2011**, *115*, 9195.
- (110) Gepshtein, R.; Huppert, D.; Agmon, N. *Journal of Physical Chemistry B* **2006**, *110*, 4434.
- (111) Weber, W.; Helms, V.; McCammon, J. A.; Langhoff, P. W. *Proceedings of the National Academy of Sciences of the United States of America* **1999**, *96*, 6177.
- (112) Baldridge, A.; Solntsev, K. M.; Song, C.; Tanioka, T.; Kowalik, J.; Hardcastle, K.; Tolbert, L. M. *Chemical Communications* **2010**, *46*, 5686.

- (113) Baranov, M. S.; Lukyanov, K. A.; Borissova, A. O.; Shamir, J.; Kosenkov, D.; Slipchenko, L. V.; Tolbert, L. M.; Yampolsky, I. V.; Solntsev, K. M. *Journal of the American Chemical Society* **2012**, *134*, 6025-6032.
- (114) Wu, L.; Burgess, K. *Journal of the American Chemical Society* **2008**, *130*, 4089.
- (115) Megley, C. M.; Dickson, L. A.; Maddalo, S. L.; Chandler, G. J.; Zimmer, M. *The Journal of Physical Chemistry B* **2008**, *113*, 302.
- (116) Polyakov, I. V.; Grigorenko, B. L.; Epifanovsky, E. M.; Krylov, A. I.; Nemukhin, A. V. *Journal of Chemical Theory and Computation* **2010**, *6*, 2377.
- (117) Martin, M. E.; Negri, F.; Olivucci, M. *Journal of the American Chemical Society* **2004**, *126*, 5452.
- (118) Dickson, R. M.; Cubitt, A. B.; Tsien, R. Y.; Moerner, W. E. *Nature* **1997**, 388, 355.
- (119) Jou, F.-Y.; Freeman, G. R. *The Journal of Physical Chemistry* **1979**, *83*, 2383.
- (120) Carroll, E. C.; Song, S.-H.; Kumauchi, M.; van Stokkum, I. H. M.; Jailaubekov, A.; Hoff, W. D.; Larsen, D. S. *The Journal of Physical Chemistry Letters* **2010**, *1*, 2793.
- (121) Larsen, D. S.; van Stokkum, I. H. M.; Vengris, M.; van der Horst, M. A.; de Weerd, F. L.; Hellingwerf, K. J.; van Grondelle, R. *Biophysical Journal* **2004**, *87*, 1858.
- (122) Wishart, J. F.; Neta, P. *The Journal of Physical Chemistry B* **2003**, *107*, 7261.
- (123) Draper, W. M.; Crosby, D. G. *Journal of Agricultural and Food Chemistry* **1983**, *31*, 734.
- (124) Milosavljevic, B. H.; Micic, O. I. *The Journal of Physical Chemistry* **1978**, *82*, 1359.
- (125) Cormack, B. P.; Valdivia, R. H.; Falkow, S. *Gene* **1996**, *173*, 33.

- (126) Daglio, S. C.; Banterle, N.; D'Alfonso, L.; Collini, M.; Chirico, G. *Journal of Physical Chemistry B* **2011**, *115*, 10311.
- (127) Mallik, R.; Udgaonkar, J. B.; Krishnamoorthy, G. *Proceedings of the Indian Academy of Sciences-Chemical Sciences* **2003**, *115*, 307.
- (128) Saxena, A. M.; Udgaonkar, J. B.; Krishnamoorthy, G. *Protein Science* **2005**, *14*, 1787.
- (129) McAnaney, T. B.; Zeng, W.; Doe, C. F. E.; Bhanji, N.; Wakelin, S.; Pearson, D. S.; Abbyad, P.; Shi, X. H.; Boxer, S. G.; Bagshaw, C. R. *Biochemistry* **2005**, *44*, 5510.
- (130) Huang, B.; Bates, M.; Zhuang, X. W. In *Annual Review of Biochemistry* **2009**, *78*, 993.
- (131) Stiel, A. C.; Trowitzsch, S.; Weber, G.; Andresen, M.; Eggeling, C.; Hell, S. W.; Jakobs, S.; Wahl, M. C. *Biochemical Journal* **2007**, *402*, 35.
- (132) Henderson, J. N.; Ai, H.-w.; Campbell, R. E.; Remington, S. J. *Proceedings of the National Academy of Sciences of the United States of America* **2007**, *104*, 6672.
- (133) Richards, C. I.; Hsiang, J. C.; Senapati, D.; Patel, S.; Yu, J. H.; Vosch, T.; Dickson, R. M. *Journal of the American Chemical Society* **2009**, *131*, 4619.
- (134) Richards, C. I.; Hsiang, J. C.; Dickson, R. M. *Journal of Physical Chemistry B* **2010**, *114*, 660.
- (135) Vosch, T.; Antoku, Y.; Hsiang, J.-C.; Richards, C. I.; Gonzalez, J. I.; Dickson, R. M. *Proceedings of the National Academy of Sciences* **2007**, *104*, 12616.
- (136) Battistutta, R.; Negro, A.; Zanotti, G. *Proteins-Structure Function and Genetics* **2000**, *41*, 429.
- (137) Scholz, O.; Thiel, A.; Hillen, W.; Niederweis, M. *European Journal of Biochemistry* **2000**, *267*, 1565.
- (138) Yang, F.; Moss, L. G.; Phillips, G. N. *Nature Biotechnology* **1996**, *14*, 1246.

(139) Seifert, M. H. J.; Georgescu, J.; Ksiazek, D.; Smialowski, P.; Rehm, T.; Steipe, B.; Holak, T. A. *Biochemistry* **2003**, *42*, 2500.